1-12-2017 12:00 AM

# Design of Radio-Frequency Arrays for Ultra-High Field MRI

Ian R O Connell, *The University of Western Ontario*

Supervisor: Professor Ravi Menon, Ph.D., *The University of Western Ontario*

A thesis submitted in partial fulfillment of the requirements for the Doctor of Philosophy degree in Medical Biophysics

# Abstract

Magnetic Resonance Imaging (MRI) is an indispensable, non-invasive diagnostic tool for the assessment of disease and function. As an investigational device, MRI has found routine use in both basic science research and medicine for both human and non-human subjects.

Due to the potential increase in spatial resolution, signal-to-noise ratio (SNR), and the ability to exploit novel tissue contrasts, the main magnetic field strength of human MRI scanners has steadily increased since inception. Beginning in the early 1980's, 0.15 T human MRI scanners have steadily risen in main magnetic field strength with ultra-high field (UHF) 8 T MRI systems deemed to be insignificant risk by the FDA (as of 2016). However, at UHF the interaction of electromagnetic fields with nuclei in human tissue assume 'wave-like' behaviour due to an increase in the precessional frequency of nuclei at UHF. At these frequencies, the electromagnetic interactions transition from purely near-field interactions to a mixture of near- and far-field mechanisms. Due to this, the transmission field at UHF can produce areas of localized power deposition – leading to tissue heating – as well as transmission-field weighting in the reconstructed images. Correcting for these difficulties is typically achieved via multi-channel radio-frequency (RF) arrays. This technology allows multiple transmitting elements to synthesize a more uniform field that can selectively minimize areas of local power deposition and remove transmission field weighting from the final reconstructed image. This thesis provides several advancements in the design and construction of these arrays.

First, in Chapter 2 a general framework for modeling the electromagnetic interactions occurring inside an RF array is adopted from multiply-coupled waveguide filters and applied to a subset of decoupling problems encountered when constructing RF arrays. It is demonstrated that using classic filter synthesis, RF arrays of arbitrary size and geometry can be decoupled via coupling matrix synthesis.

Secondly, in Chapters 3 and 4 this framework is extended for designing distributed filters for simple decoupling of RF arrays and removing the iterative tuning portion of utilizing decoupling circuits when constructing RF arrays.

Lastly, in Chapter 5 the coupling matrix synthesis framework is applied to the construction of a conformal transmit/receive RF array that is shape-optimized to minimize power deposition in the human head during any routine MRI examination.

Among the numerous advancements presented throughout Chapters 2 – 5, several fundamental conclusions can be drawn. As seen in Chapter 2, it is possible to derive a physical model that generalizes the equivalent circuit interactions between MRI RF array elements. The application of this physical model allows for the construction of decoupling circuits for an arbitrary number and arrangement RF array elements. This is the first demonstration of a general circuit formulism for eliminating mutual coupling in arbitrary RF arrangements. Following from this new approach to RF array design, distributed element filters were synthesized for the first time to decouple RF array elements, as outlined in Chapters 3 and 4. The application of distributed element filters demonstrated a single-layer printed circuit board method for eliminating interactions between array elements without using external decoupling circuits with tunable components, or element overlap – when applicable for loop-based elements. The level of isolation achieved between array elements was comparably better than conventional methods and provided a more flexible means by which RF arrays could be constructed. Extending the general circuit formulism even further, this thesis demonstrated the first effective application of a dipole array decoupling method. Due to the restrictions removed via the general decoupling methodology, dipole array elements were actively shape-optimized via an evolutionary computer algorithm and implemented with a decoupling circuit calculated by the general decoupling formulism. It was demonstrated in Chapter 5 that the process of shape optimizing dipole conductor paths is a powerful method for passive SAR reduction. This was achieved, for the first time, via the intelligent manipulation of non-uniformly meandered dipole conductor paths that resulted in electric field nulling across the sample. The general decoupling method, distributed filters and shape-optimized dipole arrays presented in this thesis form a complementary series of novel engineering tools for the design and construction of UHF MRI RF arrays.

## Keywords

Magnetic resonance imaging (MRI), radio-frequency coils, radio-frequency arrays, biomedical engineering, MRI physics, MRI engineering

# Co-Authorship Statement

This thesis consists of four papers describing original research works, as chapters 2, 3, 4, and 5 that are all co-authored. Contributions are described below.

Chapter 2: "General Coupling Matrix Synthesis for Decoupling MRI RF Arrays" has two contributing authors: IRO Connell and RS Menon. IC and RM devised the concept and experiments for validation. IC programmed the decoupling software in Matlab, performed FDTD electromagnetic simulations, constructed the RF coils, acquired and analyzed the data. IC and RM wrote the manuscript.

Chapter 3: " MRI RF Array Decoupling Method with Magnetic Wall Distributed Filters " has four contributing authors: IRO Connell, MA Abou-Khousa, KM Gilbert, and RS Menon. MA and RM devised the concept for the magnetic wall. MA constructed the first prototype of the magnetic wall. IC and RM elaborated upon the original concept and constructed an improved design as well as experiments for validation. IC developed the theory of operation and associated physical derivations, performed FDTD electromagnetic simulations, constructed the proof-of-principle coil, acquired and analyzed the data. KG provided assistance in collecting and analyzing the data. IC and RM wrote the manuscript.

Chapter 4: " Design and Decoupling of a Parallel Transit Head Coil at 7T with Magnetic Wall Distributed Filters" has four contributing authors: IRO Connell, MA Abou-Khousa, KM Gilbert, and RS Menon. MA and RM devised the concept for the magnetic wall. MA constructed the first prototype of the magnetic wall. IC and RM elaborated upon the original concept and constructed an improved design as well as experiments for validation. IC performed FDTD electromagnetic simulations, constructed the transmit RF coil, acquired and analyzed the data. KG provided assistance in constructing the transmit RF coil and constructed the receive coil. KG and IC performed MRI experiments. IC and RM wrote the manuscript.

Chapter 5: " Conformal Electric Dipole Array " has two contributing authors: IRO Connell, and RS Menon. IC and RM devised the concept for the design. IC wrote the software to implement the design algorithm, performed FDTD electromagnetic simulations, constructed the RF coil, acquired and analyzed the data. IC and RM wrote the manuscript.

# Acknowledgments

I have been fortunate to complete my Ph.D. at the Robarts Research Institute under the supervision of Prof. Ravi Menon. I am grateful for his mentorship and his support during my graduate studies. Whether providing criticism or praise, Ravi treats his students as equals and provides the inspiration to further their abilities as scientists. To this end, it is his enduring scientific curiosity and openness to new ideas that has provided me the opportunity to learn very much.

Dr. Kyle Gilbert, although not listed as a co-supervisor, has played an equally important role in my graduate studies. He has been a thoroughly patient teacher during my time in the RF laboratory, and many of my experiments as well as RF coil techniques and practices have been inherited from him. To this, I owe many thanks.

Members of Prof. Menon's research staff: Igor Solovey and Dr. Martyn Klassen have both been supportive in my research efforts. More specifically, discussion regarding the software development for Chapter 2 and Chapter 4, was particularly insightful and important in implementing my ideas.

This work is dedicated to my parents: Barbara and Graeme for their love and unending support of all aspects of my life; my sister: Hilary; my uncles: Rob and Marco; my grandmother: Muriel; and my grandfather: Len, a man of everlasting passions, whose life has inspired me to stay the course throughout a long and often difficult academic career.

# List of Abbreviations

| | |
|---|---|
| $k_B$ | Boltzmann's Constant |
| $\gamma$ | Gyromagnetic ratio |
| $\hbar$ | Reduced Planck's constant |
| AFI | Actual flip-angle imaging |
| $B_o$ | Main (static) magnetic field strength |
| $B_1^+$ | Transmit radio-frequency magnetic field strength |
| $B_1^-$ | Receive radio-frequency magnetic field strength |
| CMS | Coupling matrix synthesis |
| EM | Electromagnetic |
| FDTD | Finite-difference time domain |
| FOV | Field of view |
| pTx | Parallel transmit |
| pRx | Parallel receive |
| RF | Radio frequency |
| ROI | Region or interest |
| SAR | Specific absorption rate |
| SNR | Signal to noise ratio |
| $T_1$ | Longitudinal relaxation time |
| $T_2$ | Transverse relaxation time |

# Table of Contents

# List of Tables

# List of Figures

# List of Appendices

# Preface

Magnetic resonance imaging (MRI) is a versatile tool for equal use in diagnostic radiology as well as basic science research. The soft tissue contrast achieved with MRI, in conjunction with the ability to image without the use of ionizing radiation, presents MRI as an ideal choice for radiological imaging of human anatomy, as an observational device and as a pre-surgical planning tool. Due to the complex contrast mechanisms available to the user in an MRI experiment, it is possible to non-invasively probe many areas in the human body as well as utilize a variety of methods for constructing images of various human and non-human imaging subjects.

The methodology and design behind MRI scanners is a multifaceted topic. This thesis concentrates on a particular component of the MRI scanner – the radio-frequency (RF) coil. The area of particular focus of this thesis is on ultra-high field (UHF) MRI and the engineering of multi-channel RF coils typically employed at these field strengths.

This field of MRI is colloquially known as 'RF engineering' and blends several aspects of electrical and biomedical engineering into the composite electromagnetic environment of an MRI scanner. Due to this, the basic physics required for understanding the operation of RF coils does not rely on an in-depth discussion of MRI physics. Rather, concepts related to microwave engineering and electromagnetics provide many of the physical basis upon which experts construct RF coils. Therefore, for the sake of readability the introduction does not provide an in-depth overview of MRI physics and the current state-of-the art MRI applications. For a more extensive overview of basic MRI principals and applications, the author found the following textbooks very insightful during the writing of this thesis:

1. "Magnetic Resonance Imaging: Physical Principles and Sequence Design", 1999. E. Mark Haacke, Robert W. Brown, Michael R. Thompson and Ramesh Venkatesan.
2. "Principles of Magnetic Resonance Imaging", 1999. Zhi-Pei Liang, Paul C. Lauterbur.
3. "RF Coils for MRI", 2012. J. Thomas Vaughan, John R. Griffiths.

This page is intentionally left blank.

# Chapter 1

## Objectives

Magnetic resonance imaging (MRI) is performed via a complex system of electromagnets and radio-frequency antennae. The magnetic fields produced by the system of electromagnets and antennae allow the system to non-invasively probe the structure and dynamics of human, biological systems. This thesis presents advancements on the design of novel antennae that produce radio-frequency magnetic fields which interact with nuclei located within the human body. It is demonstrated that for a subset of the design challenges associated with constructing these antennae, increases in antennae performance directly result in increased patient safety during any given MRI examination and improvements in image quality. The following chapter will introduce many of the topics required for understanding the role of radio-frequency magnetic fields in MRI and the methods by which state-of-the-art antennae are designed.

## MRI Background

MRI is a non-invasive diagnostic tool routinely employed for the assessment of human anatomy and function. Additionally, it is an indispensible tool for basic science and medical research.

MRI utilizes the phenomenon of nuclear magnetic resonance (NMR), in concert with specialized imaging hardware, to reconstruct images associated with nuclei possessing a non-zero spin angular momentum. Non-zero spin angular momentum is a quantum mechanical property obtained by nuclei that have an odd number of protons and/or an odd number of neutrons. This property is responsible for producing a quantized magnetic moment that will respond to externally applied magnetic fields and results in energy level splitting between different spin states. In a clinical setting, the typical nuclear spin of interest is hydrogen, $^{1}$H, a spin-$1/2$ particle. In large part, this is due to two factors: (1) the relatively high abundance of hydrogen in biological tissue, and (2) the high value of the magnetic moment. Therefore, nuclear spins – or magnetic moments – for the purpose of this thesis will refer to hydrogen protons with a $\pm 1/2$ spin.

In the absence of an external magnetic field, nuclear spins will possess random orientations with respect to one-another. In this state, the net magnetization (summation of all magnetization vectors located in a volume) will be zero. However, in the presence of an externally applied magnetic field, individual magnetic moments will have a tendency to align with or against the external field. This results in a small net magnetization vector that aligns along the direction of the applied field. Therefore, to generate a detectable signal from a collection of nuclear spins in a volume, MRI relies upon the fact that large quantities of magnetic moments are utilized during an acquisition. Fortunately, there is a large abundance of hydrogen in human tissue, and this gives rise to an externally detectable signal. In combination with other physical interactions between applied magnetic fields and nuclei, the abundance of hydrogen nuclei in the human body allows MRI to reconstruct images demonstrating exquisite soft tissue contrast.

To perform MRI, three externally applied magnetic fields are utilized to manipulate the magnetic moments and reconstruct an image: (1) the static main field, referred to as '$B_o$', that produces the aligned net magnetization, (2) the gradient fields that are responsible for spatial encoding of the image, and (3) the radio-frequency (RF), or $B_1$ fields, that are responsible for signal excitation and reception.

By definition, the static $B_o$ field is uniform along the z-axis of the MRI scanner. In this orientation, the proton nuclear magnetic moments exhibit discretized energy values for the two spin states. These states are commonly referred to as spin-up and down, or as parallel and anti-parallel. Each of these spin states have characteristic potential energies. Mathematically, these energies are proportional to their gyromagnetic ratios, the reduced Planck's constant and the external magnetic flux density:

$$E = \pm\frac{1}{2}\gamma\hbar\boldsymbol{B_o} \tag{1.1}$$

where the $\pm\frac{1}{2}$ term refers to the spin state of the magnetic moment. During this discretization of spin states, there is a tendency for the higher energy state spins to drive towards a lower energy state. However, this degeneracy in spin states is offset by the

intrinsic thermal energy in the system. This surplus in spin population in the ground state is described with the Boltzmann distribution:

$$\Delta N = e^{\frac{-\Delta E}{k_B T}} \tag{1.2}$$

where $k_B$ is the Boltzmann constant, $T$ is the temperature of the system, and $\Delta E = \hbar\omega_o$ is the energy difference between spin states Due to the population excess described from (1.2), when summed over the population of spins in a sample, the vector-wise addition of magnetic moments leads to the net magnetization of the sample. In thermal equilibrium, the net magnetization $\boldsymbol{M}_o$, that is the source of the MRI signal, can be defined as:

$$\boldsymbol{M}_o = \frac{\rho\gamma^2\hbar^2\boldsymbol{B}_o}{4kT} \tag{1.3}$$

where $\rho$ is the proton density, $\gamma$ is the gyromagnetic ratio (42.57 MHz/T for Hydrogen), $\hbar$ is the reduced Planck's constant, $\boldsymbol{B}_o$ is the external magnetic flux density, $k$ is Boltzmann's constant, and $T$ is the temperature.

The classical physics model used to describe the MRI experiment relies on manipulating the net magnetization $\boldsymbol{M}_o$ vector and describes the dynamics of spin systems at a level required for performing the experiments. This is done even though it is understood that the physics of nuclear magnetic resonance (NMR) is fundamentally a quantum mechanical phenomenon.

In the classical vector model, at equilibrium when located inside the MRI scanner, $\boldsymbol{M}_o$ is aligned parallel to the $\boldsymbol{B_o}$-field located along the z-axis. This direction defines the longitudinal axis and is normal to the transverse (x-y) plane. As will be elaborated upon in section 1.1, it is possible to excite $\boldsymbol{M}_o$ out of alignment with the z-axis and $\boldsymbol{M}_o$ will precess $\boldsymbol{B_o}$ at the Larmour frequency:

$$\omega_o = \gamma\boldsymbol{B_o} \tag{1.4}$$

At the main field strength of 7 Tesla, this equates to 300 MHz for hydrogen nuclei. Once, 'tipped' off-axis, the transverse component of the $\boldsymbol{M_o}$ (projection of $\boldsymbol{M_o}$ on the x-y plane) generates detectable signal.

In the classical NMR framework, excitation is the process by which spins, collected into vector $\boldsymbol{M_o}$ from equation (1.3), are tipped off-axis through the application of radio-frequency (RF) energy. Excitation is required to acquire signal for imaging.

Spin excitation is attained by application of a time-varying RF magnetic field, $B_1^+$, at the Larmor frequency as defined in equation (1.4). The time-varying RF field is achieved through the application of a short, amplitude and/or phase modulated waveform and is typically referred to as an 'RF pulse'. After the application of an RF pulse, $\boldsymbol{M_o}$ experiences a rotation, with a component present in the transverse plane. The angle at which $\boldsymbol{M_o}$ is rotated away from the z-axis is defined as the 'flip angle' or 'nutation angle'. In terms of the RF pulse shape and duration, the flip angle is defined as:

$$\theta = \gamma \int_0^\tau B_1(t)dt \tag{1.5}$$

where $\gamma$ is the gyromagnetic ratio and $B_1(t)$ is the RF pulse as a function of time. From equation (1.5) it is apparent that either increasing the pulse amplitude or duration will result in a larger tip angle and that an RF pulse can be generated with a time-varying envelope. The application of an RF pulse can occur anywhere in the x-y plane. The phase of the RF pulse will determine about which axis $\boldsymbol{M_o}$ is rotated towards the transverse plane. For example, following a 90-degree flip angle about the x-axis, $\boldsymbol{M_o}$ is completely rotated away from the z-axis and lies in the transverse plane, aligned along the y-axis. Once the excitation is complete, $\boldsymbol{M_o}$ precesses freely about the z-axis with the principal component of $\boldsymbol{M_o}$ rotating in the transverse plane. Once the $\boldsymbol{M_o}$ component is freely precessing, two forms of macroscopic relaxation occur post excitation: (1) spin-lattice relaxation and (2) spin-spin relaxation. Spin-lattice relaxation characterizes the spin systems drive back to thermal equilibrium and can be quantitatively measured in terms of signal evolution over time. This process causes a regrowth of the $\boldsymbol{M_o}$ vector along the z-axis and is defined by the time constant $\boldsymbol{T_1}$. Spin-spin lattice relaxation describes the local interaction between an

ensemble of spins that produce the vector sum $\boldsymbol{M_o}$. Once precessing post-excitation, individual spins will experience micro- or nano-scale magnetic field inhomogeneities and the phase difference between individual spins with respect to one another will accumulate. This phase difference causes signal loss over time as incoherence between individual spins rotating in the transverse plane results in vector subtraction. Time constant $\boldsymbol{T_2}$ quantifies spin-spin relaxation.

Including relaxation, the mechanics of excitation and relaxation are described in terms of the Bloch equations, which can be written in matrix form:

$$\frac{d}{dt}\begin{bmatrix} M_x' \\ M_y' \\ M_z' \end{bmatrix} = \begin{bmatrix} -\frac{1}{T_2} & \gamma B_o - \omega & 0 \\ -\gamma B_o + \omega & -\frac{1}{T_2} & \gamma B_1 \\ 0 & -\gamma B_1 & -\frac{1}{T_1} \end{bmatrix}\begin{bmatrix} M_x' \\ M_y' \\ M_z' \end{bmatrix} + \begin{bmatrix} 0 \\ 0 \\ \frac{M_o}{T_1} \end{bmatrix} \tag{1.6}$$

The MRI component responsible for exciting $\boldsymbol{M_o}$ and rotating the bulk magnetization away from the z-axis is the RF transmit coil. Similarly, when $\boldsymbol{M_o}$, or a measureable component thereof, is rotating in the transverse plane, the magnetization is detectable via magnetic induction in an RF receive coil. In more sophisticated systems, separate RF coils are utilized for reception and transmission, however it is possible to perform both functions with the identical probe in a so-called transceiver mode.

RF coils are typically resonant structures that are tuned to be sensitive to the magnetic field fluctuations generated by spins at the Larmor frequency via magnetic induction. The magnetic fields generated by RF coils are vector valued in space, with their transverse components responsible for excitation ($B_1^+$) and reception ($B_1^-$) during an MRI experiment. Typically, the transmit and receive fields are expressed in terms of their circularly polarized basis set:

$$B_1^+ = \frac{1}{2}\left(B_x + iB_y\right) \tag{1.7a}$$

$$B_1^- = \frac{1}{2}\left(B_x - iB_y\right) \tag{1.7b}$$

where co-rotating components expressed in (1.7a) are responsible for excitation, and counter-rotating components expressed in (1.7b) are responsible for reception, respectively.

The term $B_1^-$ from equation (1.7b) defines the magnitude of the magnetic field that causes an induction current to circulate in the RF receive coil. The resulting induced current in the RF coil defines the signal magnitude and phase. However, the same induction mechanisms that cause precession of the magnetic moments in the sample to produce a current in the RF coil, apply to random sources of electronic noise. These noise sources are due to random ionic movements occurring inside the sample (unrelated to precession of magnetic moments) and internal noise in the electrical devices used to construct the coil. It is the ratio between the measured signal and the noise that provides a measure of image quality. This quantity is known as the signal-to-noise ratio (SNR).

## Ultra-High Field & SAR

Ultra-high field (UHF) is defined as performing MRI at main magnetic field strengths ≥ 7 Tesla (T). In many MRI acquisitions, the sensitivity is strongly related to the magnetic field strength ($\boldsymbol{B_o}$). This can be illustrated from equation (1.3) where the net magnetization aligned along the z-axis, $\boldsymbol{M}_o$, is directly proportional to the applied static field, $\boldsymbol{B}_o$. Thus, there exists a drive to image at ever increasing $\boldsymbol{B_o}$ due to the potential for higher spatial resolution, an increase in the signal available for imaging, and the ability to exploit novel tissue contrasts [1]. However, it is clear from equation (1.4), the Larmor frequency that excites spin populations increases linearly with field strength. Due to this, when increasing field strength, the RF transmit coils produce electromagnetic radiation of increasingly shorter wavelengths. Additionally, the wavelength of an electromagnetic

wave is inversely proportional to the square root of the relative permittivity of the medium in which it travels:

$$\lambda_{material} \sim \frac{\lambda_{free-space}}{\sqrt{\varepsilon_r}} \tag{1.8}$$

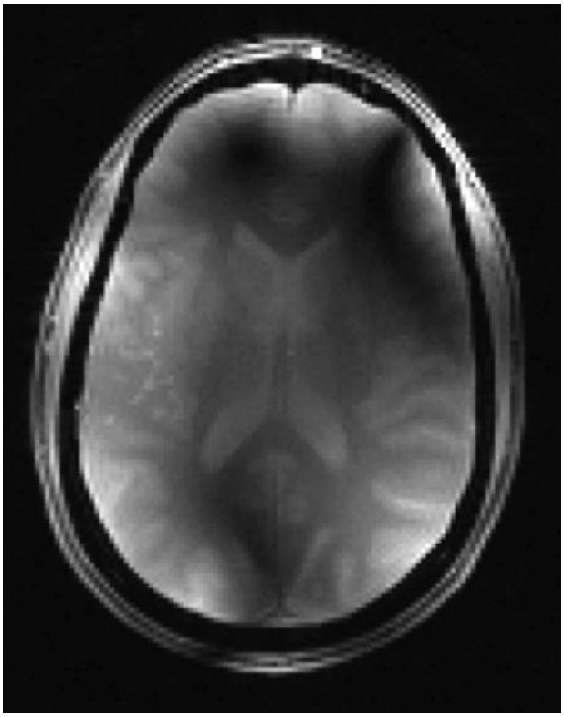

**Figure 1: 'Wave-like' interactions during excitation, resulting in tissue-independent weighting in the reconstructed image.**

Once at 7 T for head imaging, the wavelength of the excitation field is now on the order of the dimensions of the human anatomy that is being imaged: ~12 cm at 7 T in human tissue. This is a large problem for performing MRI at UHF on human subjects. Non-uniformities in the excitation field can lead to tissue-independent contrast weighting in the reconstructed images, which is below the level required for radiological confidence. This occurs due to a variation in flip angles occurring across the imaging volume as defined as a variation in $B_1$ term from equation (1.5). Typically, the behaviour of the RF transmit field at UHF is termed 'wave-like' due to the visual wavelength interactions that occur inside the imaging volume as demonstrated in Fig. 1. The reason for these 'wave-like' interactions is due to the resonant effect of standing waves in the tissue. With standing waves present,

both constructive and destructive interference exists across the field-of-view (FOV) as a function of distance away from the transmitting element. Thus areas of hyper- and hypo-intensity in Fig. 1 demonstrate areas where either constructive or deconstructive interference patterns exist.

This concept of ‘wave-like’ interactions occurs due to classic electromagnetism. Typically, when producing an excitation for MRI $\leq 3$ T in the human head, the RF excitation field resides in the ‘near-field’ regime. RF fields are classified to be in the ‘near-field regime’ when the wavelength of the electromagnetic wave is long relative to the imaging volume. Therefore, fully self-propagating waves are not yet the dominant field sources. Instead, the magnetic and vector potentials for currents produced on the structure of the RF transmit coil generate the electric and magnetic fields. The potentials are the sole mechanism for producing fields-at-a-distance and are linearly proportional to the excited currents. In this regime, several magnetostatic assumptions can be made which further simplify the design and visualization of homogeneous RF fields required for excitation. However, when approaching 7 T in the human head (or the torso at 3 T), the excitation transitions away from purely near-field interactions to a combination of near- and far-field interactions.

At 7 T, displacement currents are being produced inside the sample. However, a fully developed travelling wave solution is not supported. Therefore, the excitation of human tissue in this regime is known as lying within the ‘transition zone’ or ‘Fresnel zone’. When observing electromagnetism in the transition zone, both wave-behaviour and near-field interactions account for portions of the observed electromagnetic interactions. However, if either model is solely applied across the entire region-of-interest, both will fail to fully encapsulate the dynamics of the entire system. Therefore, with the occurrence of both physical models during excitation at 7 T, the magnetic field component of the RF

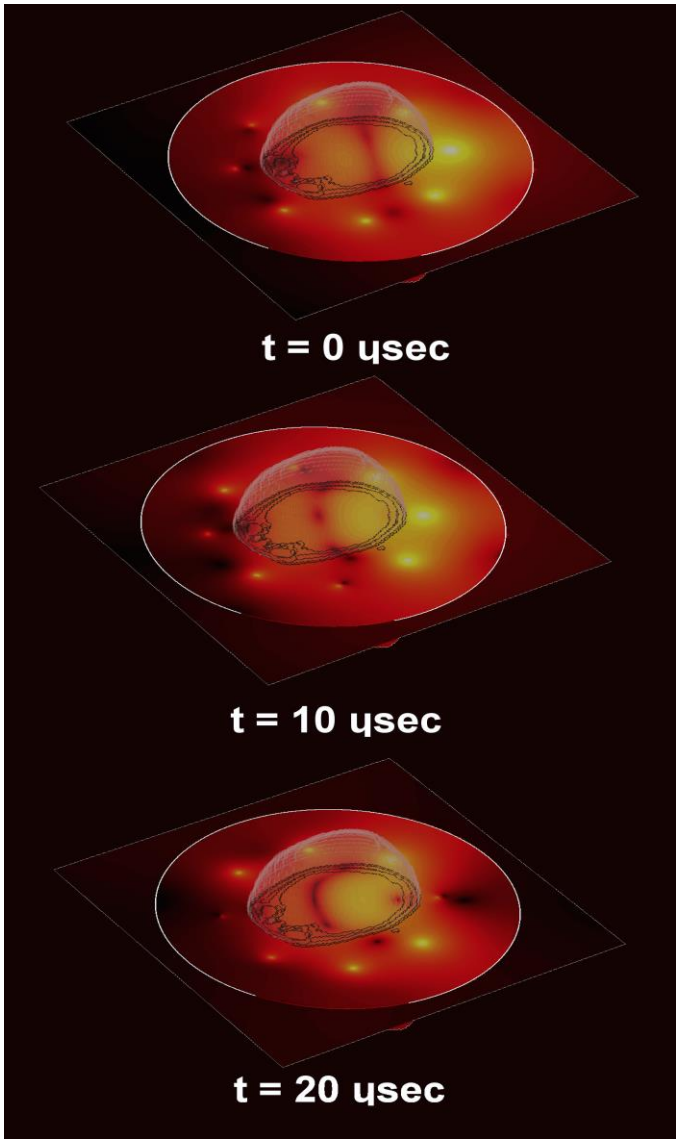


**Figure 2: Time-lapse of RF excitation field ($B_1^+$). Wave propagation is visible towards the anterior of the head, with near-field interactions present at the posterior.**

transmit field can vary in intensity across the imaging FOV. This gives rise to 'wave-like' interactions that can be observed in MRI exams at UHF, if left unmitigated. This electromagnetic behaviour is demonstrated in Fig. 2 where an RF excitation source is placed at the posterior of a numerical human head phantom. Following the time-lapse simulation at 297.2 MHz, the wave behaviour is clear – developing near the isocentre of the brain, and forming a wavefront that travels towards the anterior of the head. However,

near-fields are present at the posterior of the head, adjacent to the source of excitation, before equation (1.8) begins to dominate the fields.

In addition to the magnetic field distribution occurring at the 'transition zone', the electric field can be similarly non-uniform. The electric field contributes to the total power deposition occurring inside human tissue and poses the most significant patient risk during any routine MRI examination. Coupling the intrinsic resistance present in human tissue with the electric potential generated inside human tissue due to the presence of an electric field, Joule heating results. For MRI, Joule heating is assessed in terms of power deposition due to the transmission field. To assess patient risk due to radio-frequency fields, the power deposition is averaged across a defined tissue mass. This quantity is known as specific absorption rate (SAR):

$$SAR = \frac{1}{V}\int_{sample} \frac{\sigma(\boldsymbol{r})|\boldsymbol{E}(\boldsymbol{r})|^2}{\rho(\boldsymbol{r})}\, d\boldsymbol{r} \tag{1.9}$$

where V is the volume of the sample, $\sigma$ is the conductivity of the sample volume, $\rho$ is the density of the sample volume, $\boldsymbol{E}$ is the electric field at some position in space $\boldsymbol{r}$.

Although tissue heating is of prime concern, typically SAR, which is an abstract measure of temperature rise in tissue, is used to evaluate the safety of any given RF coil or MRI sequence. This is due to the fact that in vivo temperature mapping is difficult to accurately determine and is variable across subjects due to anatomy and metabolic function. Therefore, the metric of SAR is adopted to provide conservative estimates of potential tissue heating due to power deposition.

Equation (1.9) is evaluated against FDA guidelines to ensure patient safety. These guidelines typically refer to a set of four hard limits on the maximum allowed energy deposition in the human head. The limits are divided into global SAR (SAR averaged over the entire head) and the local SAR (SAR averaged over any closed 10-g volume of tissue). The four are evaluated for both 10-second average and 6-minute average. Table I: IEC/FDA SAR Guidelines for MRI provides a summary of the SAR limits as defined for diagnostic MRI.

Areas of increased electrical activity due to ‘transition zone’ interactions are called local SAR ‘hot-spots’ and occur due to a concentration of electric field at any given point in the sample. These local SAR ‘hot-spots’ pose the most significant patient safety risk for UHF MRI due to the constructive and destructive interference patterns of the transmission field. Due to this, new types of RF coils that exploit the dynamics of the ‘transition zone’ of electromagnetic fields are required for performing homogeneous excitation, with minimal SAR burden, in UHF MRI.

**Table I: IEC/FDA SAR Guidelines for MRI**

| | |
|---|---|
| Local SAR | 30 W/kg per 10-s over 10-g volume |
| Local SAR | 10 W/kg per 6-min over 10-g volume |
| Global SAR | 9.6 W/kg per 10-s over whole head |
| Global SAR | 3.2 W/kg per 6-min over whole head |

# Multi-Channel Radio-Frequency Arrays

## Theory and Construction

The MRI scanner is composed of many subsystems, each responsible for different aspects of imaging. The radio frequency (RF) coil sub-system includes a device located around the object to be imaged (in the case of neuro-imaging, the patient’s head and neck). The RF coil is responsible for both transmitting a magnetic field into the patient that excites the tissue, as well as receiving a signal post-excitation. This received signal is then used to reconstruct an image, or is analyzed based on tissue-specific parameters (e.g. $T_1$ or $T_2$ tissue relaxation times). The most sophisticated versions of these RF coils include a separate RF coil to transmit into the patient, and a second RF coil, located extremely close to the patient, to receive the signal. A sample schematic for a transmit array is provided in Fig. 3a, with a sample schematic for a receive array provided in Fig. 3b.

During reception, a greater sensitivity to the sample contributes to higher SNR in the reconstructed image. Therefore, receive arrays utilize the high local sensitivity individual array elements exhibit and extend this sensitivity across the array’s entire field-of-view. Similarly, transmit arrays utilize the multiple sensitivity profiles to synthesize a tailored excitation.

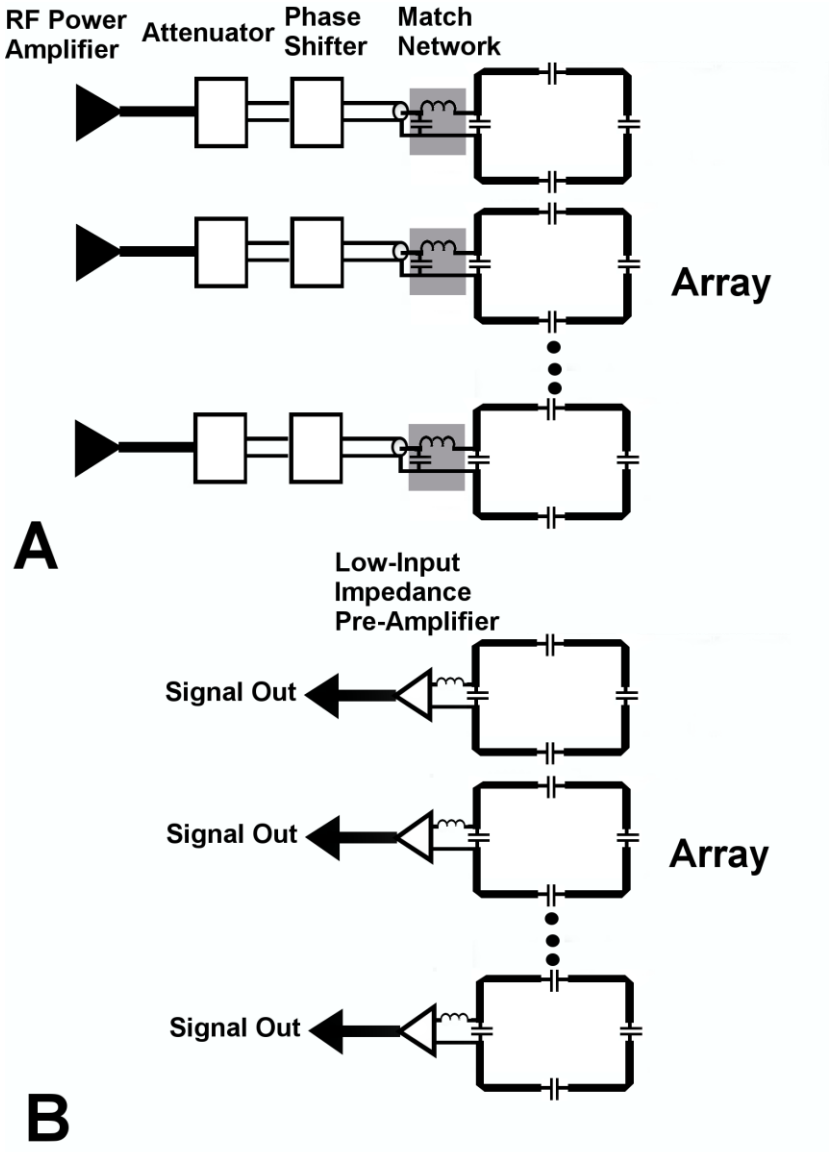


**Figure 3: General schematics of multiple resonating elements attached to the RF chain for (a) transmit arrays and (b) receive arrays.**

A tailored excitation is a method for combating UHF excitation inhomogeneity, and to-date many RF transmit arrays have been constructed with multiple resonating elements. The sample schematic for an RF transmit array is presented in Fig. 3a which shares many similarities with its receive counterpart in Fig. 3b. The main concept behind constructing RF transmit arrays is that multiple elements, each with individual waveforms (phase, amplitude, and/or time envelope), can be independently controlled to produce

desired transmit fields on a per channel basis. Then, software algorithms can compute solutions that drive the individual channels such that their combined fields achieve a more uniformly excited target, reduced SAR, or a weighted combination of both simultaneous objectives. A demonstration of this is provided in Fig. 4.

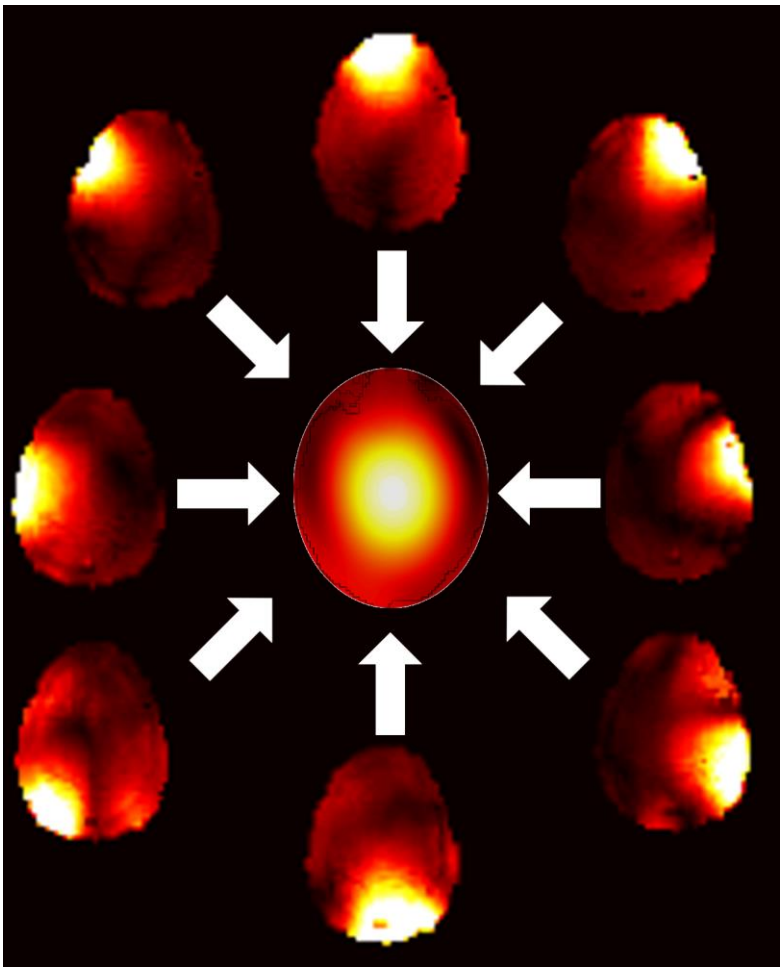

**Figure 4: Combination of individual transmission profiles from a transmit RF coil.**

## Array-Element Design

Among several factors, the electromagnetic field produced in the imaging volume is directly related to the size and geometry of the individual elements that compose the full RF array. Due to this, many types of elements have been explored for the purpose of more efficiently exciting or receiving signal from the transverse magnetization. Furthermore, when placed into an array, different element types may encounter dissimilar interactions

with either the sample or adjacent elements. Therefore, the selection of the basic element that composes a full array is typically evaluated with several criteria: (1) $B_1^+/B_1^-$ efficiency, (2) electric field generation per unit $B_1^+$ (SAR), (3) ease of construction and (4) ability to limit mutual interactions between elements in the array.

The most common form of array element is a resonant loop. The loop-based element is a tuned structure that acts as a magnetic dipole – generating a very strong magnetic near-field, with minimal electrical fields. Therefore, it is a suitable element for MRI at most field strengths. However, at UHF it has been demonstrated that the ideal current patterns responsible for exciting and producing signal from the transverse magnetization transition away from an entirely reactive-near field RF excitation and reception [2]. Visualization of these ideal current patterns has provoked work into combining dissimilar RF elements and/or constructing arrays that utilize elements that are not solely the classic tuned loop. The most common UHF-specific element is the electric dipole that produces a linear current pattern in the closely spaced conducting sample.

As visible in Fig. 3, a typical building block for an RF array – transmit or receive – includes a resonant structure (in the case of Fig. 3, a loop with lumped capacitors) as well as an RF chain matched at each individual element input. The individual elements, transmit or receive, can be modeled as a series RLC circuit – see Fig. 5. The first resonant frequency can be calculated from:

$$\omega_o = \frac{1}{\sqrt{LC}} \tag{1.10}$$

where 'L' is the total inductance of the element, 'C' is the capacitance and '$\omega_o$' is the resonant frequency of the circuit. The efficiency of individual array elements are typically evaluated based upon an equivalent circuit model of an RLC circuit, whereby the ability for an array element to store energy is defined in terms of 'Q-factor':

$$Q = \frac{\omega_o L}{R} \tag{1.11}$$

where 'R' is the parasitic resistance. Therefore, it is clear that with the resonant frequency fixed at the Larmor frequency, either the inductance needs to be increased or resistance

minimized. Typically, the inductance is held constant due to the fact that the major source of inductance in an array element is the loop inductance formed from the conductive trace or wire that defines the element. For non-loop based elements, inductance is a combination of self-inductance of the conductor and additional turns or folder-over in the element's structure. The length and dimensions of the elements are dictated by the geometry of the RF coil construction. Hence, minimizing series resistance in an array element one tactic for producing highly efficient MRI probes.

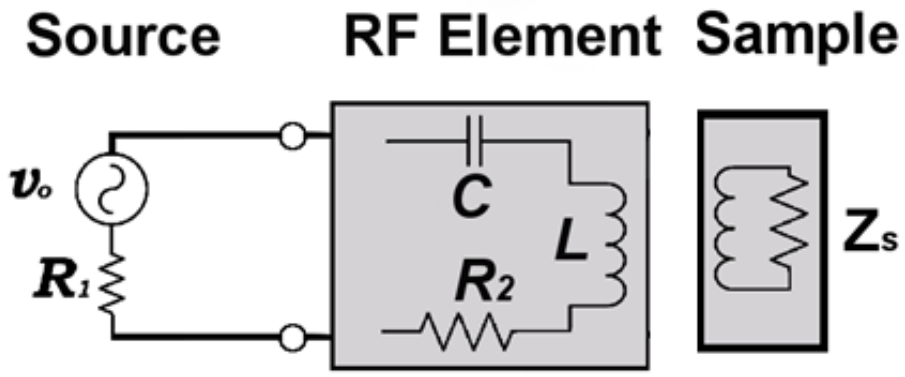


**Figure 5: Equivalent circuit of an RF element driven with a voltage source. Sample interactions with the element are typically modelled with an increase in resistance and inductive coupling.**

The SNR loss of an MRI probe can be evaluated in terms of the 'loaded' to 'unloaded' Q-ratio. Whereby, the terms 'loaded' and 'unloaded' refer to the probe in the presence of a lossy, conducting body and in isolation, respectively [3]:

$$Q_{ratio} = \frac{Q_u}{Q_l} \tag{1.12}$$

During transmission, the efficiency of RF coils is typically evaluated based upon the excitation produced in the sample, for a given root-mean-square (RMS) 10-g SAR value – $\frac{B_1^+{}_{VOI}}{\sqrt{SAR_{10g}}}$ or in units of $\frac{\mu T}{\sqrt{W/kg}}$ [4]. This efficiency defines the RF coil's ability to produce a transverse magnetic field in the patient, for a given 10-g SAR level – which is commonly the limiting factor during transmission at UHF.

Also present in Fig. 5, is the sample impedance '$Z_s$' that is typically modeled as an equivalent resistance due to sample losses that dampen the resonance calculated in equation (1.11). Additionally, inductive coupling to the sample modifies the total equivalent inductance measured at the input of the RF element. This modifies the reactive portion of the impedance of the RLC circuit. Due to this, the equivalent circuit representation in Fig. 5 can be expanded into a network representation seen in Fig. 6a. Here, along the RF chain matching networks as well as balanced-to-unbalanced transformers (baluns) are included. Baluns connect the RF element and the rest of the RF chain via coaxial cable - reducing current along the coaxial cable shielding. This minimizes cable radiation and parasitic coupling to other electrically active elements in the RF array and electronics. Two forms of baluns are employed in this thesis: (a) shielded LC trap baluns – see Fig. 6b – and (b) lattice LC baluns – see Fig. 6c.

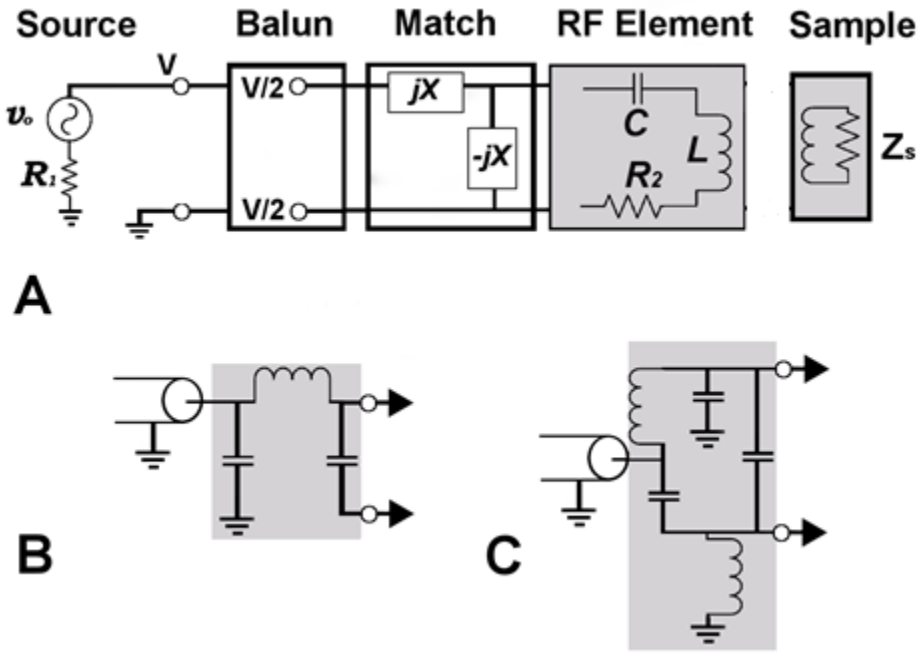


**Figure 6: (a) Network circuit of RF element connected to matching network and balun. (b) 'LC' choke balun used in concert with shunt capacitor for matching and (c) lattice balun and shunt capacitor for matching.**

As seen in Fig. 5, the sample equivalent impedance modifies two portions of the RF element RLC equivalent circuit: (a) the input impedance, and (b) the resonant frequency of the element.

(a) For the transmit array presented in Fig. 3a, a matching network is required to provide a conjugate power match to connect the loaded RLC circuit to a 50 Ω driving impedance output from the RF power amplifier. Similarly, a matching network for the receive array, presented in Fig. 3b, is required to maximize signal directed back towards the MRI console.

(b) Both the transmit and receive arrays presented in Fig. 3, include capacitors on the RF elements. Tuning is achieved by calculating the required capacitance in concert with pre-existing element inductance to resonate an element in the presence of a load. Additional fine-tuning of the resonant frequency, in presence of a sample, is provided via replacing discrete lumped capacitances with tuner capacitors at the drive port and opposite thereof. For loop-based RF elements, this has the additional benefit of reducing radiation emanating from the element and maintains an intense near-field distribution. For non-loop based elements, resonance is achieved by designing self-resonant structures via combining self-inductance with self-capacitance – terms typically defined by the geometry of the forming conductors and electrical parameters.

The network representation in Fig. 6a demonstrates the matching networking as a function of RF element equivalent circuit parameters as well as relative loading to the sample. Therefore, if either loading or circuit self-impedance changes, the matching network most-often need be adjusted. However, for MRI typically narrowband ‘L’ networks are used to sufficient accuracy required for matching elements. An ‘L’ network is presented in Fig. 7.

'L' matching networks combine two reactive elements. Throughout this thesis, the series inductor and shunt capacitor is employed for matching. This is possible, as the

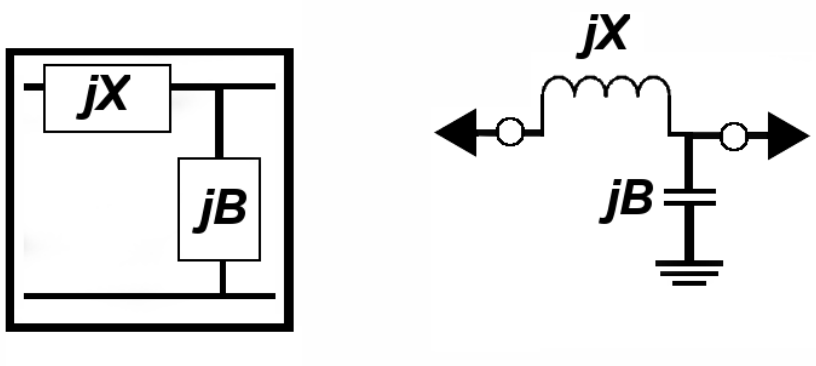


**Figure 7: 'L' matching network for RF arrays constructed in this thesis.**

amplifier intrinsic impedance '$R_o$' is greater in magnitude than the load impedance, which for MRI RF elements is the impedance of the damped resonant circuit – damping determined by the resistive loss and inductive coupling to the sample in Fig. 5.

The equations that define the matching under these conditions can be written as:

$$B = \frac{X_L \pm \sqrt{\frac{R_L}{Z_o}}\sqrt{R_L^2 + X_L^2 - Z_o R_L}}{R_L^2 + X_L^2} \tag{1.13a}$$

$$X = \frac{1}{B} + \frac{X_L Z_o}{R_L} - \frac{Z_o}{B R_L} \tag{1.13b}$$

where 'X' an 'B' calculate the circuit values from Fig. 7. '$R_L$' and '$X_L$' are the load resistance and reactance, respectively. '$Z_o$' is the source impedance.

## Electromagnetic Coupling

Electromagnetic coupling ('coupling') is the transfer of energy between components in an electrical system. Coupling arises from electrically- or magnetically-induced interactions that can cause undesired effects on the operation of RF arrays. The design of RF arrays, both receive and transmit, require individual resonating coils in the array to be

located in close proximity to one-another. The required close spacing between coils results in coupling.

Electrically induced sources of coupling in an RF array include both free-space and sample-mediated interactions. Free-space electrical coupling occurs due to overlap in the near-field distributions of closely spaced resonating elements. In this physical manifestation, the overlap in electric field between array elements can be modeled as a capacitor electrically connecting nearby elements [5]. Due to the presence of this electrical pathway, high-frequency current can be distributed between adjacent elements. In the second physical manifestation, the closely-spaced conducting sample provides a lossy pathway for parasitic currents to be transmitted and received between nearby RF array elements [5]. The magnitude of this coupling is a function of the sample material properties, and separation between elements. Finally, magnetic-coupling arises due to Faraday's law. The time-varying magnetic field produced by an RF array element will produce an electromotive force (EMF) at the terminals of a neighbouring coil, resulting in an induced electric current [6].

In the most extreme case, contributions to the input impedance of an array element in the presence of coupling can cause detuning and mismatching of array elements. During transmission, detuning and mismatching results in power reflection at the input of the RF array element, decreasing overall array excitation efficiency. Similarly, power transfer between elements due to coupling does not contribute to producing an excitation inside the sample and provide an additional means for efficiency loss. This is due to the fact that coupled power is directed backwards, away from the RF coil, and dissipated across dummy 50-Ohm terminations located near- or inside-the power amplifiers. During reception, detuning and mismatching reduces the magnitude of signal that is transferred from the RF array element to the console, reducing the overall signal-to-noise ratio (SNR) in the reconstructed image. This concept is illustrated in Fig. 8 where in the equivalent circuit; coupling contributes to the reactance of the input impedance of each RF element. The magnitude of coupling, defined by their lumped element equivalents, will determine the relative contributions to the input impedance in accordance with their physical layout. A derivation is provided in equations (1.16-17) for two of the three elements in Fig. 8.

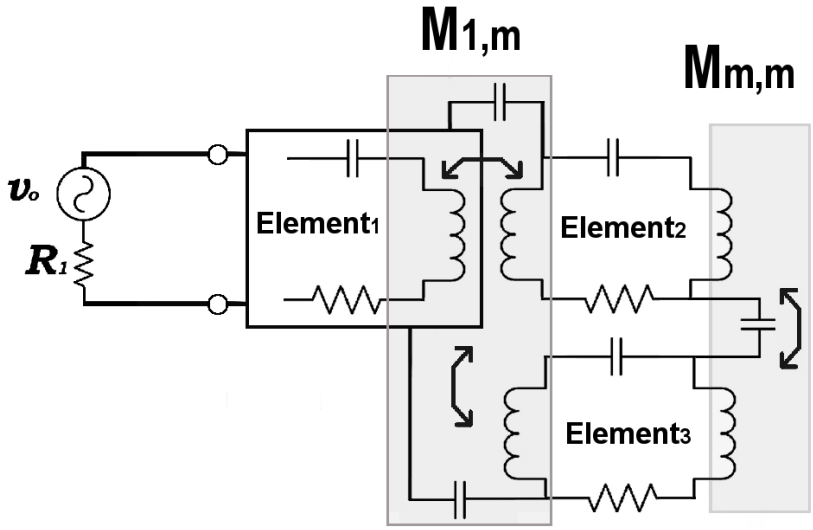


**Figure 8: Mutual coupling between RF elements modelled via magnetic (mutual inductance) and electric (shared capacitor) interaction.**

For both transmit, receive and transceiver RF arrays, coupled RF array elements demonstrate a spatially dependent relationship between one-another in the sample. This occurs as the primary field produced by a single array element will excite currents in adjacent coupled elements, via one/or more of the mechanisms described above, that in turn produce secondary fields in space. The vector sum of these secondary fields with the primary field is not directly related to the original source of excitation. For transmit arrays, this increases the complexity for synthesizing flat excitation patterns, requiring an iterative solution, and make SAR reduction less predictable from any set of channel driving parameters. In terms of receive array performance; the coupling manifests itself as an increase in the noise correlation between elements. If non-linear, correlated noise has the potential to degrade the accelerated SNR of the system during under-sampled acquisition.

In this thesis, 'mutual impedance' is commonly used to quantify the effect of coupling in an RF array. Like self-impedance, mutual impedance has a real (resistive) component as well as an imaginary (reactive) component:

$$Z_{self} = R_{self} + iX_{self} \tag{1.14a}$$

$$Z_{mutual} = R_{mutual} + iX_{mutual} \tag{1.14b}$$

In a system of multiple interacting circuits, or in the case of an RF array multiple interacting RF elements, the impedance of the entire system can be represented algebraically as:

$$[\mathbf{V}] = [\mathbf{I}][\mathbf{Z}] \tag{1.15}$$

where

$$[\mathbf{V}] = \begin{bmatrix} \boldsymbol{V_i} \\ \vdots \\ \boldsymbol{V_n} \end{bmatrix} \qquad [\mathbf{I}] = \begin{bmatrix} \boldsymbol{I_1} \\ \vdots \\ \boldsymbol{I_n} \end{bmatrix} \qquad [\mathbf{Z}] = \begin{bmatrix} \boldsymbol{Z_{1,1}} & \cdots & \boldsymbol{Z_{1,n}} \\ \vdots & \ddots & \vdots \\ \boldsymbol{Z_{n,1}} & \cdots & \boldsymbol{Z_{n,n}} \end{bmatrix} \tag{1.16}$$

Following from Fig. 8, the off-diagonal terms in the impedance matrix from (1.15) are the mutual impedance terms from (1.13b) that itemize the coupling between elements. The individual input impedances of each circuit element are located along the main diagonal of (1.15) and take the form of the self-impedances (1.13a). The reactive component of the mutual impedance includes contributions from both the capacitive (electrical) and inductive (magnetic) coupling mechanisms outlined above. Typically, both coupling mechanisms are present, however one will have a greater effect on the type of reactance that is measured. This is reflected in the sign of the imaginary component. A positive reactance denotes predominately inductive coupling and a negative reactance denotes a predominant capacitive coupling. The matrix equations in (1.15) can be extended to include both resonating, non-resonating as well as radiating array elements and non-radiating circuits in the array in one compact formulism.

Solving (1.15) for the case of two mutual coupled RLC circuits takes the form of:

$$\begin{bmatrix} R_1 + j\omega\left(L_1 + \dfrac{1}{C_1}\right) & j\omega M_{12} \\ j\omega M_{12} & R_2 + j\omega\left(L_2 + \dfrac{1}{C_2}\right) \end{bmatrix} \begin{bmatrix} i_1 \\ i_2 \end{bmatrix} = \begin{bmatrix} V \\ 0 \end{bmatrix} \tag{1.17}$$

where the self-impedance is located along the diagonal, with mutual coupling terms located along the off-diagonal. Under these conditions, two resonant frequencies are defined:

$$\omega_1^2 = \frac{1}{L_1 C_1}\left(1 + \frac{M}{L_1}\right)^{-1} \qquad \omega_2^2 = \frac{1}{L_2 C_2}\left(1 + \frac{M}{L_2}\right)^{-1} \tag{1.18}$$

From equation (1.18) it is clear that the magnitude of coupling term 'M' – which can be extended to include both electric and magnetic interactions (see Chapter 3) – defines the relative effect coupling will have on the tuning and matching of an RF array.

It is clear from equation (1.17) that electromagnetic coupling in RF arrays increases in complexity when considering an array that mixes dissimilar element patterns (loops and dipoles, by example). This is due to the fact that the matrices involved in solving the system of equations increases in size and the terms that form the coupling matrix 'M' can vary non-uniformly, depending on the geometry and loading of the constructed array. Similarly, unusual element patterns, that may have benefits in terms of efficiency or SAR management, etc., will all couple via one of the previously mentioned mechanisms, however with different magnitudes and predictability depending on the geometry of the array and the element. Therefore, coupling mitigation requires some knowledge of the electromagnetic fields involved with the problem, as well as a general understanding of circuits that can be reliably constructed for arrays with many elements.

## Coupling Mitigation

Due to the geometric constraints of designing RF arrays and the possibility of ever-increasing channel counts, strategies for adequately decoupling RF array coils has been the source of many studies [5-11]. Practically speaking, the minimum level of isolation achieved in these arrays (and subsequently, the minimum level of isolation typically required for operating RF coil arrays) is on the order of -12 dB for transmission and -18 dB for reception.

The most common form of element decoupling was presented by Roemer et. al. [12]. Roemer and colleagues demonstrated that it was possible to completely eliminate magnetic

coupling between adjacent resonant loops by overlapping the adjacent loops. When the overlap in loops approaches roughly ~ 15% of their total area, the EMF induced in either loop is cancelled by the voltage present in the overlapped portion of loops. However, it was noted that inductive coupling between non-adjacent elements was not exactly cancelled by this approach. Therefore, their next development was the application of low-input impedance preamplifiers at the input of the receiving loops. When placed in series with a tuner capacitor, the inductance in the loop along with the capacitor formed a parallel resonant circuit across the virtual short present across the terminals of the pre-amplifier (due to the very low input resistance). This parallel resonant circuit presents high impedance on the loop on-resonance. Therefore, the total current flowing on the resonant loop due to magnetic induced interactions with the sample is suppressed. This reduced the residual coupling, not accommodated for with loop overlap, to acceptable levels for signal acquisition. The use of loop-overlap in conjunction with low-input impedance preamplifiers does not completely eliminate electrically induced sources of coupling. This is due to the fact that both loop overlap and reducing the magnitude of current flowing on the individual elements are strategies aimed at reducing inductive coupling. Although loop overlap was demonstrated by Roemer to reduce a portion of the capacitive coupling, a measurable coupling coefficient was still measured when inductive coupling was effectively eliminated between two elements.

A similar procedure can be performed for transmit arrays that relies on loop overlapping as well. Due to the fact that low-input impedance amplifiers are not readily available at the power levels required for MRI excitation, loop overlap can be offset with a myriad of additional techniques including: (1) the insertion of decoupling capacitors between neighbouring elements, (2) insertion of decoupling inductors between neighboring elements, and/or (3) insertion of resonant circuits between neighbouring elements. The general concept behind these additional circuits is to compensate for the induced currents in the elements that either directly cancels the mutual impedance with a new electrical pathway and/or modifying the input impedance of the elements such that it is possible to selectively match current modes in the array that exhibit minimal coupling. More sophisticated driving systems have also been developed to reduce element coupling, with the most prominent method being the Cartesian Feedback approach [13]. These techniques

rely on either modifying the driving conditions of the array such that decoupled modes are power matched, or a feedback loop is included which injects current into the elements that directly oppose the coupling. These aforementioned techniques can be classified as strategies to implement a high-output-impedance power amplifier.

## Parallel Transmission Strategies

Parallel transmission utilizes the distinct sensitivity profiles generated by multi-channel RF arrays (see section 1.3), to tailored RF excitation throughout the imaging volume. By employing additional degrees of freedom in terms of excitation profiles, studies have been performed to increase volume selectivity during imaging [14], increase homogeneity of the transmission field [15], and/or reduce the SAR [16, 17].

The form of parallel transmission that is employed in the studies outlined in this thesis is 'RF shimming' [18]. RF shimming combines the spatial profiles of transmit array elements with a set of magnitude weightings and phase offsets. The subsequent operation is a vector sum, resulting in an excitation that is a linear combination of fields produced by individual coils:

$$B_1^+(\boldsymbol{r}, w) = \sum_{i=1}^{\#\ elements} w_i B_{1,i}^+(\boldsymbol{r}) \tag{1.19a}$$

$$w_i = A_i e^{i\emptyset_i} \tag{1.19b}$$

where $A_i$ is the per-channel magnitude scaling and $\emptyset_i$ is the per-channel phase offset.

Through individual control of each coil element via equation (1.18b), the RF excitation field is shaped for a summed excitation at some point **r** in space. In terms of the magnitude coefficient '$A_i$' in (1.18b), separate power amplifiers per channel scale the contributions from each element. The phase offset term '$\emptyset_i$' is modified via phase shifters located along the RF chain between the transmit array and the power amplifiers. The spatial phase offset, and separate per-channel waveform generators enable modulation of the RF pulse shapes on a per-transmitter basis. The MRI platform used in this work has eight separate RF chains, enabling all of these capabilities for fine control of the transmitter

channels.

The equations (1.18a) and (1.18b) can be used to solve a simple minimization problem given some desired target region in the sample and $B_1^+$ distribution. Solving the minimization problem involves selecting a weights vector from (1.18b) to optimize a metric over a targeted region of interest (ROI) for imaging, typically a voxel, slice, or volume in the sample. In terms of $B_1^+$ homogeneity, in this thesis the minimization problem was solved in the least-squares sense:

$$\min_{w} \|wB_1^+(\boldsymbol{r}, w) - B_1^+(\boldsymbol{r})\|^2 \tag{1.20}$$

where $B_1^+(\boldsymbol{r})$ is a desired distribution across the ROI and the weighting vector 'w' is the optimization variable. Similar minimizations were formulated in this thesis that minimize the SAR distribution or electric field distribution in the sample:

$$\min_{w} \|wB_1^+(\boldsymbol{r}, w) - B_1^+(\boldsymbol{r})\|^2 + \lambda \|f(SAR(\boldsymbol{r}))\|^2 \tag{1.21}$$

where $f(SAR(\boldsymbol{r}))$ is some function defining the total SAR in the ROI, or is a weighted combination of the electric field distribution computed with the 'w' weights. The Lagrangian multiplier '$\lambda$' represents a scaling factor to weight the amount of regularization of the final solution with respect to the penalization of SAR.

The equations (1.19) and (1.20) represent the common minimization problem that software algorithms attempt to solve for a given RF transmit array. Typically, the residual computed from either (1.19) or (1.20) is a combination of the algorithm design, the ROI and the array construction. The type of element, number of array elements and its geometry have a direct impact on the ability to obtain a suitable solution to (1.19) and (1.20). Therefore, the careful selection of array elements and the elimination of electromagnetic coupling between them present an important challenge addressed by this thesis and the following chapters.

Additional means for increasing the homogeneity and/or simultaneously decreasing SAR burden for a given pulse sequence includes the use of fully parallel transmission strategies such as transmit SENSE [19]. Transmit SENSE utilizes both RF waveform

manipulation in conjunction with the three orthogonal gradient coils to manipulate the excitation across time. The governing equation for transmit SENSE excitation is a linear combination of individual pulse profiles ($P_r$) weighted by corresponding sensitivity profiles ($S_r$) [19]:

$$P_{des}(\boldsymbol{x}) = \sum_{r=1}^{R} S_r(\boldsymbol{x}) P_r(\boldsymbol{x}) \tag{1.22}$$

whereby the desired excitation profile is defined across 'R' voxels for any given point 'x' in the VOI. Pulse profiles $P_r$ are generated as a combination of gradient waveforms and the pulse envelop of the transmit excitation.

## Thesis Objectives

To-date, the largest implementation barriers for clinical translation of UHF MRI include an increase in SAR and reduce homogeneity of the RF transmission field. The adoption of multi-channel RF arrays have proven to be an effective method for addressing these concerns. However, the presence of mutual coupling along with geometry-specific solutions for realizing RF arrays have limited their ability to reduce SAR while increasing homogeneity of the RF transmission field. Therefore, this thesis presents several key advancements in the theory and understanding of mutual coupling in RF arrays. Furthermore, it presents several flexible solutions for eliminating mutual coupling and applies them to several RF arrays constructed for UHF MRI.

With the construction of several well-decoupled RF arrays, several hypotheses are addressed by this work:

(1) Does an increase in element-to-element isolation translate to increased imaging performance?
(2) Does a more flexible solution for isolating elements in an RF array remove implementation barriers for more sophisticated RF array designs that have potential benefits for UHF MRI?
(3) Is it possible to shape-optimize conducting structures to passively shape

the electromagnetic fields responsible for SAR and nuclear excitation?

To test the above research questions, several studies were performed. These studies included:

(1) The design and construction of several well-isolated loop-based RF arrays utilizing various decoupling strategies synthesized from new methods laid out in Chapter 2.
(2) The construction of a novel dipole-based RF array that is shape-optimized to selectively reduces 10g-SAR while maintaining excitation uniformity.
(3) The decoupling of a novel dipole-based RF array where previous decoupling methods were not applicable.

# Chapter 2

# Coupling Matrix Synthesis for Decoupling MRI RF Arrays

In this chapter, a general framework is developed for understanding coupling and decoupling in complex, arbitrary RF array constructions. This chapter is derived from the manuscript, "General Coupling Matrix Synthesis for Decoupling MRI RF Arrays" published in IEEE Transactions on Medical Imaging on April 2016.

## Introduction

Generally speaking, previous derivations aimed at minimizing coupling in RF arrays have relied upon analytic expressions that are solved for zero mutual impedance between array coils as presented in equation (1.17). Analytically, this derivation takes the form of a closed-form matrix diagonalization whereby the off-diagonal impedance terms are 'zeroed'. This procedure attempts to find an orthogonal basis set of eigenmodes that when applied to the input of each array element produces zero mutual coupling and the characteristic behaviour of coupled elements. This strategy implies that the impedance matrix is well conditioned and there exists a sufficient number of linearly independent entries that allow the decomposition procedure to continue. However, the impedance matrix in (1.15) physically represents a system of coupled-equations. Therefore, the matrix is rank deficient, and additional degrees-of-freedom need to be inserted into the impedance matrix in order to perform a meaningful reduction. These additional degrees-of-freedom take on the form of secondary, non-radiating electrical circuits. With the insertion of these circuits, a set of current modes can either be driven or power-matched such that the magnitude of the off-diagonal coupling terms is reduced to a suitable level. This strategy dramatically increases in complexity as the number of coils is increased. At present, with receive-only RF array coils utilizing as many as 96 receivers [20], and transmit arrays utilizing up to 16 transmitters [21] or more, this strategy of computing circuit element values based on analytic derivations is no longer trivial and the algebraic approach is more tractable.

Similarly, it is not rigorously defined if decoupling two adjacent elements can be extended to larger array counts with more complex electromagnetic environments and/or a

combination of resonant nodes and asymmetric cross coupling throughout the array. Hence, the solution presented by Roemer [12] for receive arrays utilizing geometric overlap in concert with low-input impedance pre-amplifiers has been widely considered one of the most important methods of array construction to-date for two reasons: (a) the efficacy of the method, and (b) the relatively direct implementation. Therefore, when investigating array element patterns that are no longer well-suited for existing decoupling methods, such as dipole elements where element overlap is not possible or transmit arrays with 50 Ohm driving impedance, a general set of simple circuit constructions that will suitably eliminate all forms of main-line and cross-coupling in the array would serve useful for realizing novel array designs, akin to overlapping loop elements.

Given the resulting system of coupled equations for these large array channel counts, a method for generally decoupling resonant circuits in an arbitrary design can take on the form of an inverse filter design problem, whereby specific array features, such as frequency response, can be prescribed and the required circuit values solved for. In terms of RF arrays for MRI, this has not been previously investigated, and has great potential for implementing a series of well-known classes of ladder filter designs not previously defined for large-coil count RF arrays.

In this paper, a general approach for synthesizing complex decoupling networks for RF arrays is formulated in terms of a prototype filter design problem using coupled resonator circuits [22]. The frequency response of the coupled resonator circuits is found from exciting individual ports of the coupled circuit based upon the RF array design. This frequency response is fitted to predetermined reflection polynomials [23] with the objective of simultaneously minimizing all possible transmission between all coils in the array. The solution to this problem is presented in the form of a bounded, nonlinear optimization that directly calculates a coupling matrix [**M**], without perturbing the original RF array element coupling. The synthesized [**M**] compensates for both main-line and cross-coupling in the array to produce a fully decoupled RF array. Furthermore, we demonstrate that a sparsity-enforced ($L_1$-norm regularized) coupling matrix [**M**] is achieved via a 2-stage decoupling ladder network or $10^{th}$-order distributed filter, that are appropriate for most conceivable MRI RF array designs. Monte-Carlo simulations are utilized to validate

the efficacy of this approach. Computed results can be realized in terms of lumped element ladder networks, distributed element networks, used to define placement of coils in an RF array, or a combination of all three, given that the coefficients from [**M**] are reproduced in the final RF array construction.

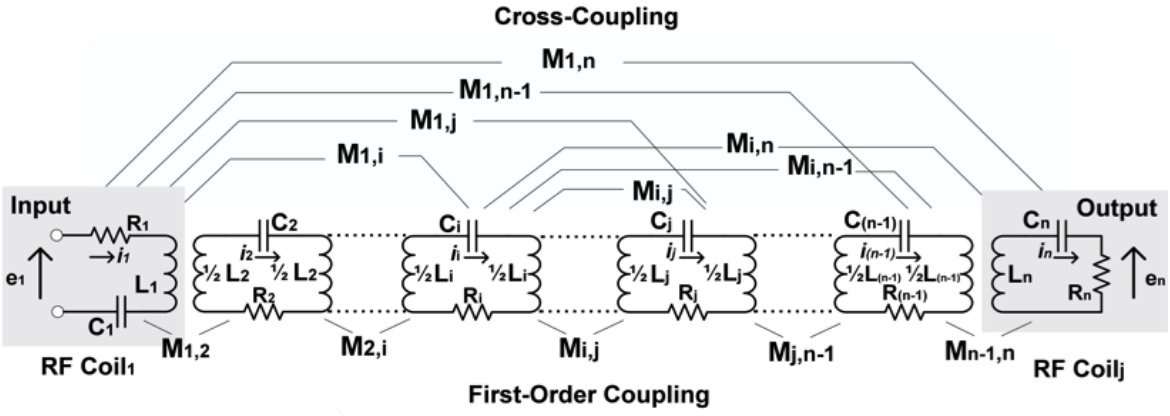


**Figure 9: Equivalent circuit of RF array with multiple couplings.**

The application of prototype filter design via modulating the coupling matrix is well known. However, the application of it for MRI RF arrays requires several specific new requirements not typically addressed with the conventional theory. For decoupling RF arrays, the array coils themselves must retain high Q, and be matched to the same source impedance outside the network. However, the additional decoupling networks inserted into the equivalent circuit do not necessarily require uniform Q, nor are they terminated outside the network. Therefore, although the circuit elements and the transfer functions derived between array coils are linear functions, the simultaneous matching of specific array coils terminated outside the array, while maintaining uniform Q between array elements only, presents a nonlinear objective function. Hence, formulating the problem of decoupling an RF array in terms of nonlinear programming provides a unique opportunity to solve for possible decoupling strategies in this non-smooth domain. Similarly, evaluation of regularized solutions demonstrates the first MRI RF array decoupling solution that can eliminate all first- and higher-order coupling in complex arrays by simply placing coupling matrix optimized circuits between nearest-neighbours. Additionally, the method extends

the decoupling capability of these circuits beyond symmetric arrays or pre-defined array geometries.

## General Theory

The equivalent circuit of a RF array can be described with multiple couplings between *n*-resonant circuits with the following indices:

| | |
|---|---|
| *n* | Total number of coupled resonant circuits |
| *i,j* | Arbitrary pair of coupled resonant circuit (index 1 → *n*) |
| *m,k* | Arbitrary terminating resistances for any *i,j* circuit |
| | (index 1→ *n*) |

Therefore, the equivalent circuit is reduced to Fig. 9 and it can be seen that the hypothetical array is similar to a cascaded filter design problem, with each circuit representative of a ladder stage. As such, the coupling arrangement for this equivalent circuit is defined with

$$[\boldsymbol{M}] = \begin{bmatrix} M_{1,1} & \dots & M_{1,n} \\ \vdots & \ddots & \vdots \\ M_{n,1} & \cdots & M_{n,n} \end{bmatrix} \tag{2.1}$$

The diagonal terms in [**M**] are the respective 'self-coupling' values. For the prototype filter response, a value of '0' for the 'self-coupling' term in [**M**] is equivalent to zero frequency shift away from $\omega_o$ at that specific resonant circuit (either RF array element, or decoupling element). For coupling values in [**M**] not equal to '0', the frequency shift ($\omega_{shift}$) from $\omega_o$ can be calculated with repsect to the prototype lowpass corner frequency ($\omega_c = 1$) as,

$$\omega_{shift} = \omega_o \pm \frac{M_{i,j}}{2} \tag{2.2}$$

where the normalized coupling values $M_{i,j}$ in the synthesized coupling matrix [**M**] are related to the physical coupling coefficients '$k_{i,j}$' via,

$$k_{i,j} = M_{i,j} \cdot \frac{\Delta f}{f_o} \tag{2.3}$$

The term '$f_o$' denotes the centre frequency to which the final design is scaled (ie. 297.2 MHz for 7 T MRI) and '$\Delta f$' is the prototype bandwidth scaled to the frequency range of the centre frequency '$f_o$'.

Defining the excitation vector

$$\begin{aligned} [\boldsymbol{e}] &= [e_1\ e_2 \dots e_n] \\ e_1 &= [1\ 0\ 0 \dots 0]^{\boldsymbol{T}} \\ e_2 &= [0\ 1\ 0 \dots 0]^{\boldsymbol{T}} \\ &\vdots \\ e_n &= [0\ 0\ 0 \dots 1]^{T} \end{aligned} \tag{2.4}$$

and the resistance matrix

$$[\boldsymbol{R}] = \begin{bmatrix} R_{1,1} & \cdots & 0 \\ \vdots & \ddots & \vdots \\ 0 & \cdots & R_{n,n} \end{bmatrix} \tag{2.5}$$

then applying $[\boldsymbol{e}]$ at the input of terminated ports in Fig. 9, yields the network in Fig. 10. Making the narrowband approximation $j\omega M_{i,j} \approx i\omega_o M_{i,j}$, the loop current, $I_j$ in circuit $j$ from Fig. 10 is

$$\begin{gathered} \left[R_1\delta_{1,j} + R_n\delta_{n,j} + j\left(\omega - \frac{\omega_o^2}{\omega}\right)\right] I_i + j\sum_{\substack{k=1 \\ k\neq i}}^{n} M_{i,j}I_j = e_1\delta_{1,j} \\ \delta_{i,j} = \begin{cases} 0 & if\ \ i \neq j \\ 1 & if\ \ i = j \end{cases} \\ i = 1,2,3, \dots, n \end{gathered} \tag{2.6}$$

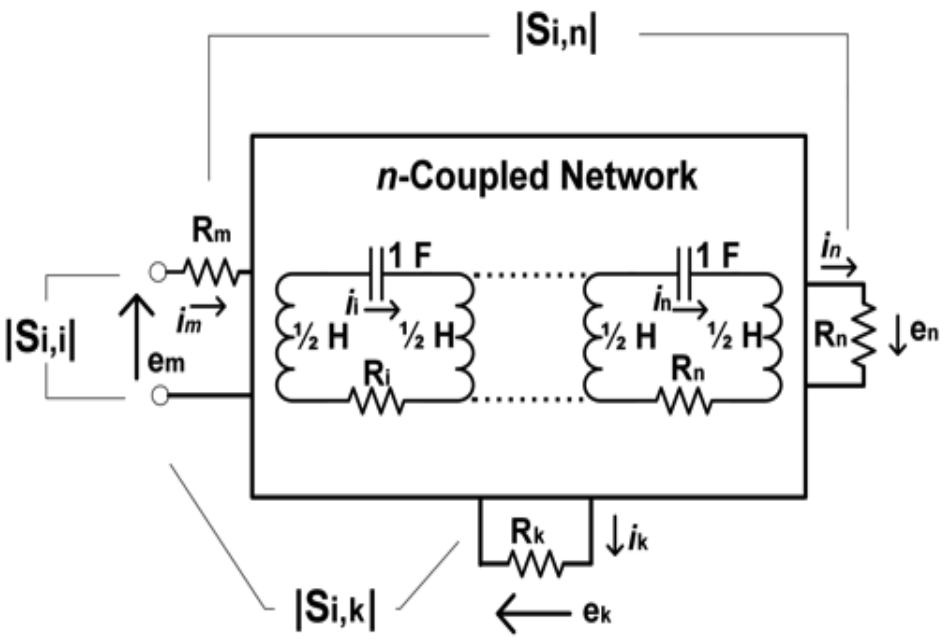


**Figure 10: Network representation of n-coupled RF array**

where $R_1$ and $R_n$ are the resistances of the source (excited RF coil) and the load (terminated RF coil), respectively; $M_{i,j}$ denote the symmetric coupling terms; and $e_1$ is the unit voltage excitation. Rewriting (2.6) into matrix form yields

$$[\sigma\mathbf{I} - j\mathbf{R} + \mathbf{M}]\varphi = -j[\boldsymbol{e}] \qquad (2.7).$$

From (2.7), **I** is the identity matrix and **M** is the symmetric coupling matrix. Input resistances of the RF coils and decoupling circuits are included in the $n \times n$ diagonal matrix **R**. In order to impedance match the RF array to the external excitation, $R_n = R_j$, at the terminated ports, with the other resistance terms set to a near-zero ($Q_{coil} < Q_{decoupling}$) fraction of the terminated resistance. This ensures that the RF coils dominate the efficiency of the array, not losses incurred in the decoupling network.

Frequency and current vector terms are defined as

$$\sigma = \omega - \frac{\omega_o^2}{\omega}$$
$$\varphi = \left[I_1, I_2, \ldots, I_j\right]^T \qquad (2.8)\ .$$

Solving the system of equations in (2.7) by exciting each RF coil in turn with every entry in the excitation vector $[\mathbf{e}]$ and solving for the currents, $\varphi$, present in each terminated RF coil results in reflection ($\Gamma$) and transmission parameters (T) of the form

$$\Gamma_{i,i} = 1 + 2jR_m[\boldsymbol{A}]^{-1}_{i,i} \qquad \mathrm{T}_{i,j} = -2j\sqrt{R_m R_k}[\boldsymbol{A}]^{-1}_{i,j} \tag{2.9}$$

where $[\mathbf{A}]$ is defined as the loop matrix impedances from Fig. 9,

$$[\mathbf{A}] = [\sigma\mathbf{I} - \mathrm{j}\mathbf{R} + \mathbf{M}] \tag{2.10}$$

and from Fig. 10, $R_m$ and $R_k$ are the unit terminated resistances at the output of each port.

Several important physical details of this circuit representation in Fig. 9 and the expression (10) include:

(1) Each resonant circuit is in series RLC form. It is not possible to represent both series and parallel RLC resonators and anti-resonators in the same coupled arrangement without applying any circuit transformations, therefore the problem is left in terms of coupled series circuits.

(2) When placed into ladder form, the decoupling circuit resonators are physically represented as coupled, shunt series resonators. When the shunt resonators are cascaded together with appropriate coupling terms, they can be used in concert with the pre-existing coil-to-coil coupling to convert the mutual impedance between RF coils from a shared inductor/capacitor link to that of a multi-pole bandstop filter – the number of poles which are dictated by the number of cascaded decoupling network sections.

(3) Although the impedances between RF coil ports can be transformed by several cascaded sections of reactive components, matching networks applied outside the network in Fig. 10 can be used to transform the input impedance to match a source impedance other than $R_s = 1$. This is achieved regardless of the internal circuit inter-connections. The accrual of any additional reactance present at the input impedance of the network is therefore tightly controlled by a synthesis procedure that penalizes both increased transmission between coils or impedance mismatch at the external ports.

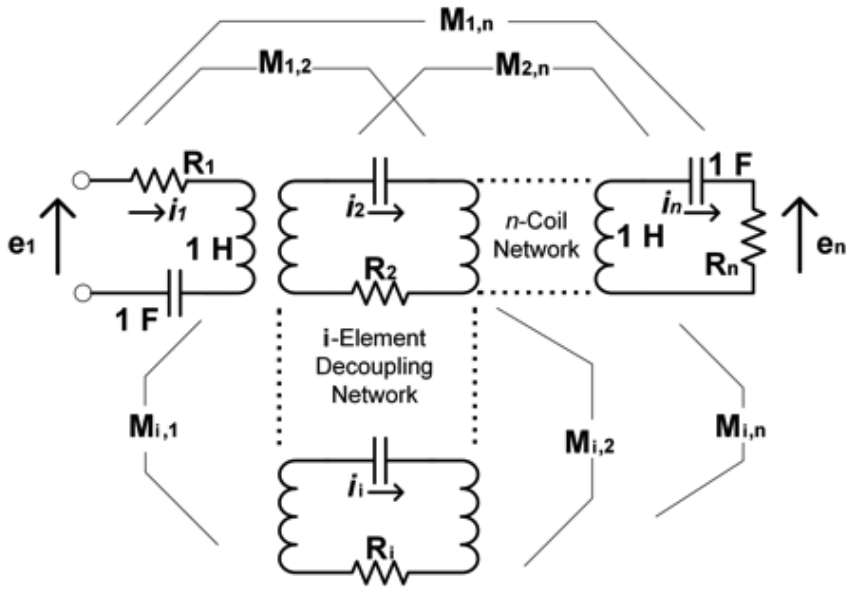


**Figure 11: Equivalent circuit of a n-coupled RF array with decoupling circuits of arbitrary dimension placed between adjacent elements**

The problem of designing a decoupled RF array becomes one of finding the optimal number of cascaded decoupling sections to compensate for pre-determined coupling values located in matrix **M** (geometry and proximity of RF coils to each other) while synthesizing the appropriate impedances for each ladder stage. Inter-stage impedance matching can be accomplished by synthesizing mutual coupling terms between decoupling elements that contribute to the overall input impedance of each cascade.

## Coupling Matrix Topology

Coupling matrix topology is a mathematical representation, (2.1), of the mutually coupled elements in an electrical system. Therefore, different RF array constructions can take on different canonical forms. A prototypical topology is presented in Fig. 11 that can be adapted for a lumped element ladder network, distributed filter or any other decoupling interface placed along the RF feed chain.

The canonical form of a coupling matrix is a function of the RF coils and decoupling element connections between the arrays. An example for one of these canonical forms is

given: a three-coil array decoupled with a 1st-order ladder network/distributed filter connected in series between adjacent coils,

$$M_{i,j} = \begin{bmatrix} M_{1,1}^{C_1} & M_{1,2} & M_{1,3} & 0 & M_{1,5} \\ & M_{2,2}^{D_1} & M_{2,3} & 0 & 0 \\ & & M_{3,3}^{C_2} & M_{3,4} & M_{3,5} \\ & & & M_{4,4}^{D_2} & M_{4,5} \\ & & & & M_{5,5}^{C_3} \end{bmatrix} \quad (2.11)\,.$$

The superscript ‘C’ denotes the RF coil number in the array, and the superscript ‘D’ denotes the decoupling circuits, connected in parallel with the RF elements through terms [1,2], [2,3], [3,4], and [4,5] used for decoupling the array. Note that only the upper triangle of the coupling matrix is shown, as the coupling matrix is symmetric about the principle diagonal.

# Coupling Matrix Synthesis

## Topology Generation

Synthesizing a particular decoupling solution begins with defining the coupling topology in a binary template of the same size. This matrix is a stencil where coupling terms that can be modified retain a ‘1’, and 0’s where the couplings are pre-determined (coil-to-coil coupling), non-physical or too difficult to realize. An example of this procedure is given for the topology in equation (2.11),

$$M_{i,j}^{tem} = \begin{bmatrix} 1 & 1 & 0 & 0 & 0 \\ & 1 & 1 & 0 & 0 \\ & & 1 & 1 & 0 \\ & & & 1 & 1 \\ & & & & 1 \end{bmatrix} \quad (2.12).$$

As demonstrated in equation (2.12), for a 1st-order decoupling network, no coupling is permitted between the decoupling circuit between coils 1 and 2 (matrix term [2,2]) and the decoupling circuit between coils 2 and 3 (matrix term [4,4]). In order to realize the coupling term [1,4] in (2.12), either a capacitive path or magnetic path would have to be introduced between the two lumped elements which would cross the field-of-view of potentially all three coils. This carries a high probability of parasitic interaction between the other elements and coils of the array.

Additionally, coupling between coils 1, 2, and 3 – matrix terms [1,1], [3,3], and [5,5] - are not modifiable as they are pre-determined by the array design and hence cannot be modified (MRI bore dimensions, the object to be imaged, desired image quality, etc.). Physically, this is done to ensure the synthesized network does not rely on coupling terms between the decoupling circuits and coils that are not simply replicated. These coefficients can be determined through various well-known methods [12, 24], estimated from the design parameters, or directly measured [25].

Due to the fact that the number of decoupling circuits required to achieve an adequately decoupled array state is not readily known, this template can be iteratively regenerated for an arbitrary number of decoupling terms, provided the same stencil requirements for synthesizing a physically realizable network.

## Polynomial Generation

In order to synthesize **M** in (2.10) a set of reflection coefficient objectives for the coils in the array are generated from a Chebyshev Type I polynomial [26],

$$\Gamma_i'(\omega) = \frac{1}{\sqrt{1+\varepsilon^2 C_n^2(\omega)}} \tag{2.13}$$

where $C_n^2(\omega)$ is the $n$ degree filtering function for the characteristic Chebyshev filter [23] and $\varepsilon$ is related to the prescribed ripple, 'R' (in dB), set equal to 0.05 dB.

$$C_n^2(\omega) = \cosh\left(\sum_{i=1}^{n} \cosh^{-1}(x_i)\right) \tag{2.14}$$

$$\varepsilon = \left.\frac{1}{\sqrt{10^{R/10}-1}}\right|_{R=0.05} \tag{2.15}$$

and $x_i$ is related to the position of the $i^{\text{th}}$ reflection zero (coil resonant frequency),

$$x_i = \frac{\omega - 1/\omega_i}{1-\omega/\omega_i} \tag{2.16}$$ .

In order to transform the transfer function between coils in the RF array from the low-pass prototype to the bandstop prototype, the following transform is applied to (2.16),

$$\frac{\omega_2 - \omega_1}{\omega_o}\left(\frac{\omega_o}{\omega} - \frac{\omega}{\omega_o}\right) \rightarrow \omega' \qquad (2.17)\,.$$

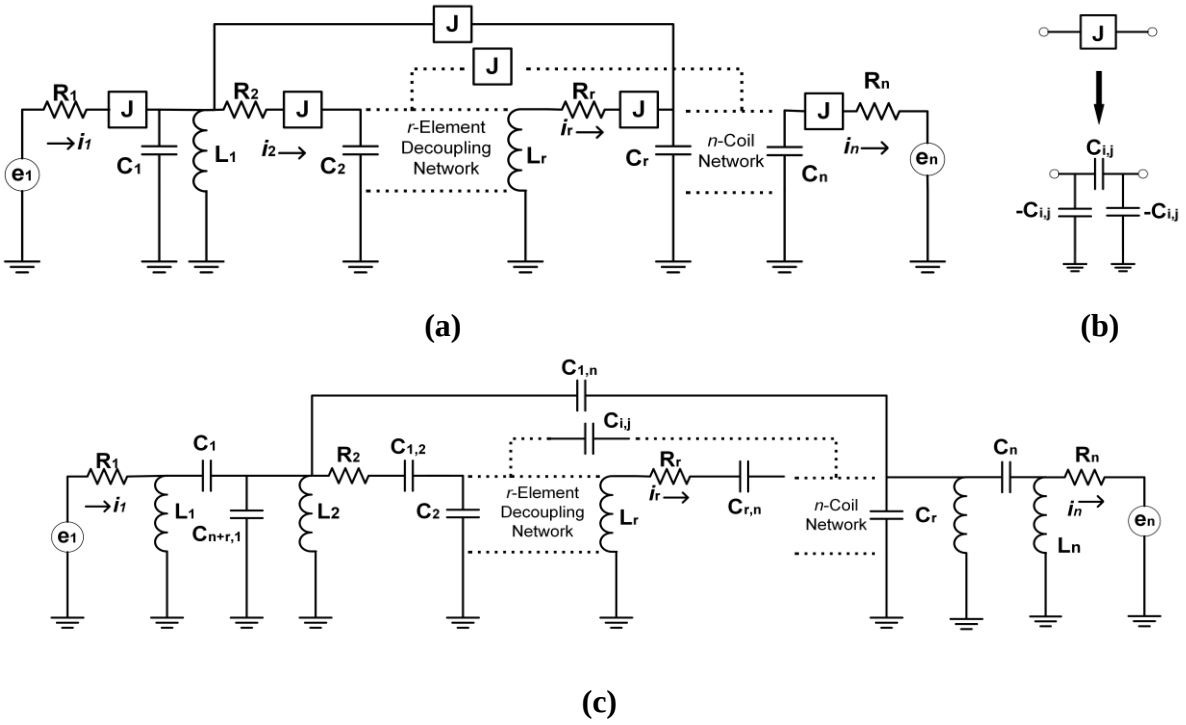


**Figure 12: (a) Multiple couplings replaced with 'J'-inverters, (b) replacement of 'J'-inverters with their capacitive PI representation and (c) final circuit realization with capacitors realizing the multiple couplings**

From (2.13), and definitions in (2.14-2.17), the reflection coefficient objectives are generated by evaluating the first-degree filtering function (*n = 1*).

The transmission coefficient goal is defined as a single point located at coil resonance ($\omega_o$). The value of $|T'_{i,j}|$ (in dB) at this point is defined as the maximum permissible amount of transmission between any coils in the RF array. This value $\boldsymbol{v}_{i,j}$ can be set to be equivalent for all transmission coefficients between array elements, or specified in vector format for individual coil pairs,

$$\mathbf{T}'_{\boldsymbol{i,j}}(\boldsymbol{\omega_o}) = [\boldsymbol{v}_{\boldsymbol{i,j}}] \qquad (\mathbf{2.18}).$$

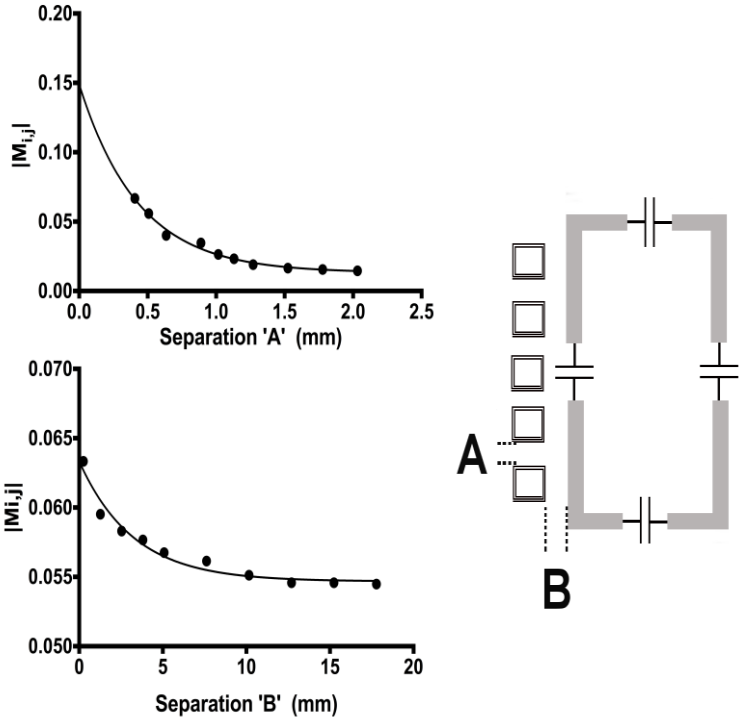


**(a)** **(b)**

**Figure 13: (a) Measured coupling coefficients as a function of distance, (b) identification of measured distances.**

## Nonlinear Least-Squares Optimization

Differences between the frequency response of the array computed in (2.9) and the set of ideal frequency responses for tuned-and-match decoupled RF coils defined in (2.13) and (2.18) can be recursively minimized, as a function of the coupling matrix **M**, in the form of a nonlinear least-squares optimization,

$$\min_{\mathbf{M}} \left\| f_i(\mathbf{M}) + f_{i,j}(\mathbf{M}) \right\|^2 \tag{2.19}$$

where the residuals of the reflection and transmission coefficients are defined for *n* coils,

$$f_i(\mathbf{M}) = \Gamma_i(\omega, \mathbf{M}) - \Gamma_i'(\omega) \qquad i = 1,2, \dots, n \tag{2.20}$$

$$f_{i,j}(\mathbf{M}) = \mathrm{T}_{i,j}(\omega, \mathbf{M}) - \mathrm{T}'_{i,j}(\omega) \quad \begin{cases} i = 1,2,\dots,n \\ j = 1,2,\dots,n \\ i \neq j \end{cases} \tag{2.21}$$

## Regularization and Optimal Network Design

Given the formulation in (2.20) and (2.21), solving for an optimum number of decoupling elements can be included via a combination of the topology stencil and an $L_1$-norm regularization that enforces sparsity in the final synthesized coupling matrix **M,**

$$\min_{\mathbf{M}} \left\| f_i(\mathbf{M}) + f_{i,j}(\mathbf{M}) \right\|^2 + \lambda \|\mathbf{M}\|_1 \tag{2.22}$$

# Physical Realization

Based upon the type of decoupling network, the physical realization of the array can be related to both geometry and positioning (distributed filer, tertiary scatterers, etc.) or lumped elements (ladder networks). Furthermore, the decoupling method could be applied along the RF chain of the array, as long as the coupling coefficient requirements are satisfied, positioning can vary.

## Ladder Networks

The coupling matrix of the ladder network can be converted to its bandstop lumped element form by coupling the resonators through *J*-inverters, see Fig. 12a. Converting *J*-admittance inverters to their capacitor network (using Fig. 12b) equivalent results in the final lumped element topology presented in Fig. 12c, with lumped element values for the decoupling network synthesized from optimizing (2.10). The resultant network is composed of shunt series resonators coupled through ∏-networks. Combining the ∏-networks results in a capacitvely-coupled bandstop filter. Matching between ladder stages is achieved via the coupling capacitors.

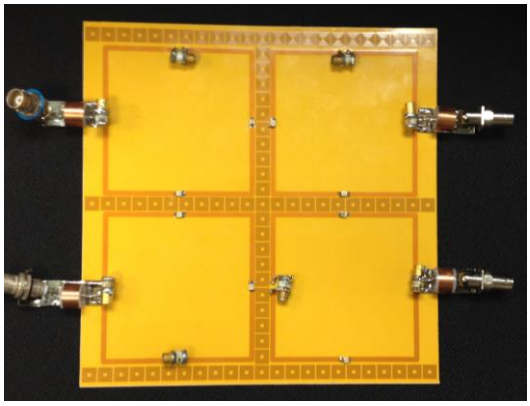

**(a)**

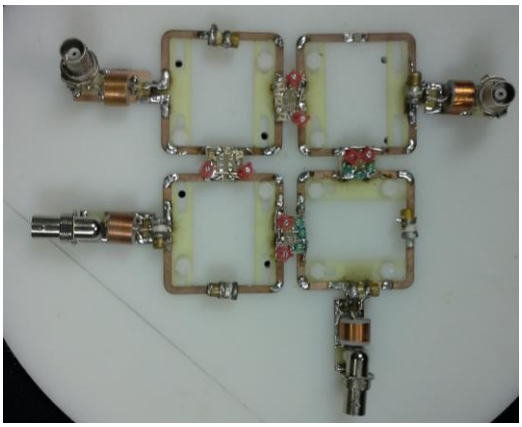

**(b)**

**Figure 14: (a) Distributed filter implemented on single-layer PCB, (b) second-order decoupling ladder filter**

## Distributed Networks

The coupling matrices for geometric overlap or the insertion of a scatterer/distributed filter result in coupling matrix values that can be directly related to the relative position of elements with respect to each other. The relative positioning of the elements will affect the magnitude of coupling and therefore can be characterized to replicate the synthesized coupling matrix from (10). An example of this is provided Fig. 13, where the coupling between a distributed filter, presented in [9], is measured as a function of distance between the filter and an adjacent RF coil, suitable for imaging at 7 T. From Fig. 13, the empirical

relationship between separation distances ‘A’ and ‘B’ and the measured coupling coefficients are,

$$k_{i,j} = 0.027A^{-1.005}$$
$$k_{i,j} = 0.0602B^{-0.036} \quad (2.22).$$

# Methods

Three theoretical array constructions were optimized with the coupling matrix algorithm. These included 4-, 8- and 32-coil arrays, respectively. These designs were chosen to replicate 8-coil transmit technology and 32-coil receive technology with the 4-coil array constructed for experimental verification. All arrays were optimized with 2$^{nd}$-order lumped element-decoupling networks as well as with 10$^{th}$-order distributed filters (order determined by the available coupling coefficients presented in the empirical relationships in (2.21)).

## Optimization Computation

The coupling matrix optimization was implemented in Matlab R2015 (Mathworks, Natick, USA) with GPU-accelerated computation performed across one Tesla K20 unit (Nvidia, Santa Clara, USA).

To replicate a typical array construction, the coil-to-coil coupling coefficients for the 4-coil arrays that were both optimized then constructed were computed from,

$$\mathrm{k_{i,j}} = \frac{f_2^2 - f_1^2}{f_2^2 + f_1^2} \quad (2.24)$$

where $f_2^2$ and $f_1^2$ correspond to the upper and lower resonant peaks resultant from coupling.

Similarly, the coupling coefficients for the 8- and 32-coil arrays were estimated from literature using well-known methods [12, 24] where the coefficients for the theoretical arrays were calculated utilizing (2.24). Coefficients across several equidistantly spaced separation distances between coils were measured, and an interpolated polynomial was constructed. This polynomial, as a function of separation distance between coils, was then used as the function to populate the entire RF array coupling matrices.

Coupling coefficients can also be readily calculated from full-wave simulation via,

$$k_{e_{i,j}} = \frac{\int_V \mathbf{E_i} \cdot \mathbf{E_j}\, dv}{\sqrt{\int_V |\mathbf{E_i}|^2 dv \times \int_V \left|\mathbf{E_j}\right|^2 dv}} \tag{2.25a}$$

$$k_{m_{i,j}} = \frac{\int_V \mu_r \mu_o\, \mathbf{H_i} \cdot \mathbf{H_j}\, dv}{\sqrt{\int_V \mu_r \mu_o |\mathbf{H_i}|^2\, dv \times \int_V \mu_r \mu_o \left|\mathbf{H_j}\right|^2 dv}} \tag{2.25b}$$

where $k_{e_{i,j}}$ and $k_{m_{i,j}}$ represent the electric and magnetic coupling coefficients between the $i^{th}$ and $j^{th}$ coils in the array each producing electric and magnetic vector fields $\mathbf{E_i}$ , $\mathbf{E_j}$ and $\mathbf{H_i}$ , $\mathbf{H_j}$ **,** respectively; terms $\mu_r$ and $\mu_o$ denoting the relative and free-space permeability; and the volume integration term $dv$ spanning the coil-sensitive region for the $i^{th}$ and $j^{th}$ coils.

To ensure results from the regularized solutions provided by solving (2.22) were stable and optimum, Monte Carlo simulations were run on the 32-coil array solution. Individual coupling coefficients between coils were distributed between 50-150% of their original value across 500 samples. A 10% bandwidth (with respect to the full frequency span) centered about $\omega_o$ was used to extract the mean value of the transmission and reflection coefficients for each run. The Monte Carlo results were then compared against the original solution's reflection and transmission coefficients, respectively.

## Experimental Verification

A physical realization of the 4-coil arrays was performed to verify the algorithms computational results. Two 4-coil arrays were designed and sized appropriately such that they were a possible subset of a full multi-channel receive head coil. Both the distributed filter and lumped element implementations of the synthesized coupling matrix were constructed and are visible in Fig. 14. To demonstrate the utility of the technique, the two coil arrays were constructed with different coil dimensions and dielectric materials. The coupling coefficients with respect to the two constructions are available in Tables I-II for

the lumped-element decoupling network array and Tables III-IV for the distributed filter array, respectively.

Differences between the computed values returned by the optimization (presented in Appendix A: Tables I-IV) and those physically realized with the constructed 4-coil arrays were calculated for: (i) shunt decoupling resonator self-resonances, (ii) coil self-resonances, and (iii) coupling capacitor values. Measured values were obtained by replacing trimmer capacitors with their discrete element value.

The 4-coil array decoupled with a distributed filter was implemented in the form of a single-layer PCB. All copper routing for both RF coils and distributed filter nodes was complete atop a single sheet of Rogers 3003 dielectric with single-layer 0.5-oz rolled copper foil. Dimensions of the four coils were 3.1 x 3.1 cm with 0.31-cm wide struts. These dimensions and positions relative to each other (see Fig. 5a) resulted in a coupling coefficient of 0.0397 for adjacent coils and 0.0243 for the coils located along the opposite diagonals. Individual nodes of the filter were self-resonant at $\omega_o = 297.2$ MHz (corresponding to a '0' in the coupling matrix presented in Table III), with coupling between node-to-node and node-to-coil given by (21). The nodes were composed of 14-windings of 3-mil wide copper traces. Copper traces were spaced 3-mil apart from winding-to-winding. Spacing between individual nodes is given in Table IV.

The four-coil array decoupled with lumped elements was implemented with four discrete coils (dimensions: 2x2 cm with 0.31-cm wide struts) with 1 oz. copper traces routed atop 0.79-mm-thick garolite. The coil dimensions and positioning (see Fig. 14b) resulted in coupling coefficients of 0.0670 for adjacent coils. Coils facing each other across the diagonal had a coupling coefficient of 0.0410.

Both lumped- and distributed-array constructions were composed of four coils and utilized surface-mount capacitors (100 series: American Technical Ceramics, NY) with values ranging from 4.2– 5.5 pF. For both arrays, variable capacitors (1 – 30 pF, Johanson Manufacturing, NJ) were placed at the drive point and opposite thereof to allow for tuning and matching. The lumped element array included three additional variable capacitors (1 – 30 pF, Sprague-Goodman, NY) and two variable inductors (25 – 34 nH, Coilcraft, IL)

were located on decoupling circuits placed between the coils. This corresponds to the topology and design values given in Tables I-II.

Both arrays were loaded with cylindrical gel phantoms (14.6 cm in diameter and 8.6 cm in height), located approximately 7.5 cm perpendicularly away from the transmit elements. The gel phantoms were composed of gadolinium chloride, agarose, and sodium chloride, in concentrations intended to mimic the human head.

*S*-parameter measurements were performed on the arrays while located inside a 40-cm cylindrical RF shield then correlated to those computed by the coupling matrix algorithm. The effect of sample loading on the physically constructed arrays was studied through a series of s-parameter measurements taken at coil-to-sample separation distances of 0-cm, 2.5-cm, and 5-cm, as well as unloaded. Separation distances were defined along the shared perpendicular axis of the RF array and cylindrical phantom.

### Full-Wave Electromagnetic Simulation

Time domain full-wave electromagnetic simulation was performed using commercially available software CST Microwave Studio Suite (Darmstadt, Germany). Simulation environment was constructed with open boundary conditions computed to -40 dB reflected power accuracy. Adaptive meshing was applied to the simulation objects with a linear *s*-parameter tolerance of 0.01. Adaptive meshing terminated once change in *s*-parameters across the frequency of interest (297.2 MHz) was less than the assigned tolerance for successive simulation passes. SAR was computed following the IEEE C95.3, regulations for 1g SAR averaging.

## Results

### $L_1$-Regularization

As demonstrated in Fig. 12 and Fig. 13, the lumped element representation of a decoupling network contains fewer limitations to the achievable coupling coefficients in a physical design. The coupling capacitor values can be altered with relative ease, whereas a distributed design relies on several physical factors that may not be simply replicated in the physical design. To this end, when solving the optimization problem for the lumped

element representation, the regularization procedure was able to achieve a decoupling solution of transmission ≤ - 20 dB between all coils with a 2nd-order network. However, due to the fact that available coupling coefficients were much more restricted in the distributed design case, many more decoupling elements were required. Therefore, in the distributed case a 10th order distributed filter was required to decouple the arrays.

Rank regularization of the decoupling network is presented in Fig. 15 for a lumped-element decoupling solution of the 32-channel array. The L-curve is normalized to the residual norm of the optimization routine for a 20-stage decoupling network. As demonstrated in Fig. 15, for a decoupling network of rank two (2nd-order lumped element network), the optimization returns a solution while increasing the magnitude of the residual norm by 17 % in comparison to the relatively unbounded 20-stage decoupling network. With respect to the feasibility of constructing a 2nd-order network, as well as the dramatic decrease in degrees of freedom for decoupling the array when moving from 20- to 2-network sections, this 17 % increase is considered a modest compromise, and can encompass many of the simultaneous decoupling objectives for the RF arrays tested in this study.

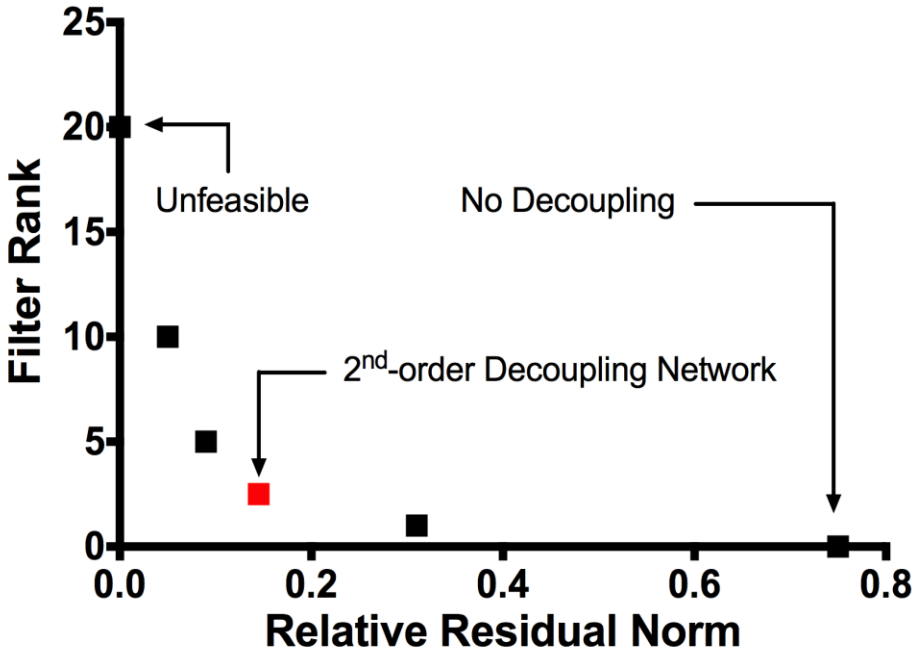


**Figure 15: Relative residual norm of the cost function as a function of filter order.**

Computation time monotonically increases as a function of array/decoupling network complexity. Total computation time for the 4-, 8- and 32-coil arrays were 2:46 min, 9:48 min and 1:32:38 min for the lumped-element designs, respectively. The distributed-element computation times for the 4-, 8-, and 32-coil arrays were 8:46 min, 1:12:06 min, and 6:38:01 min, respectively. Maximum computation times for the 32-channel array were achieved on relatively modest server platform (Tesla K20 GPU and dual Intel Xenon E5-2697V2 CPU) with total memory requirements below 1 GB. However, the main computational overhead of the algorithm includes sparse matrices, with the entirety of calculations performed in parallelizable-fashion. Due to this, additional acceleration and speed-up could be achieved via utilizing an entirely GPU-accelerated nonlinear solver, which is not currently supported in Matlab, but freely available in Python via several publically licensed toolboxes.

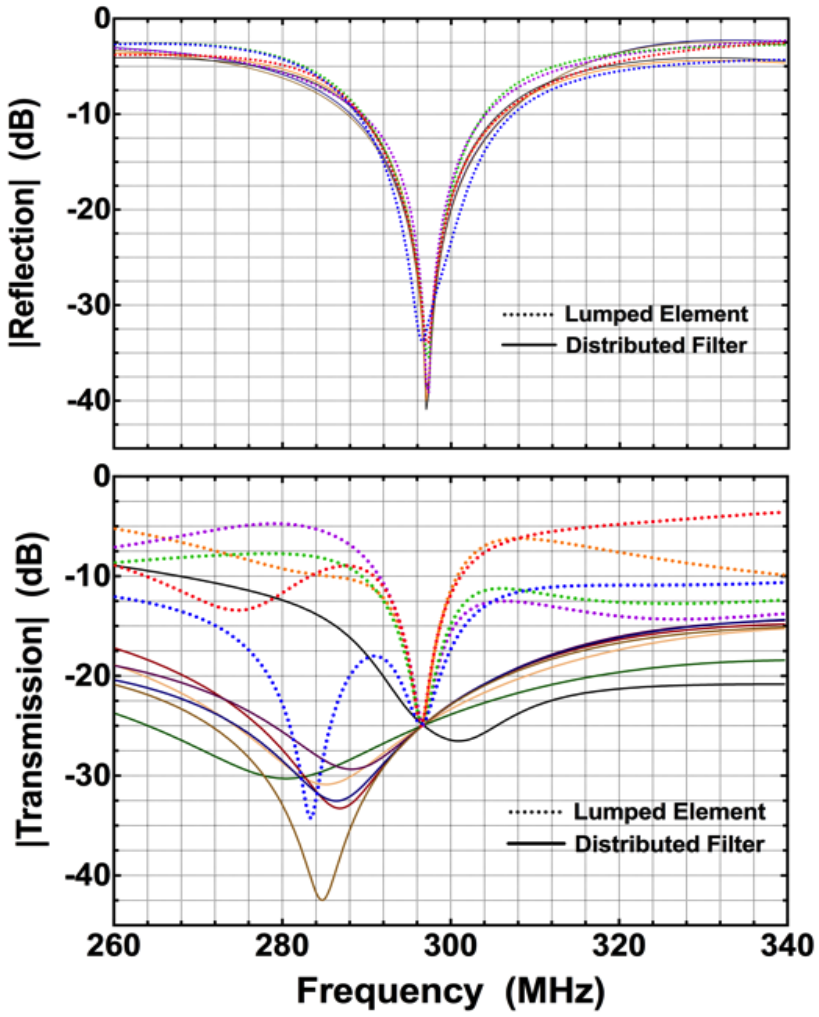


**Figure 16: S-parameters of optimized four-coil array scaled to 297.2 MHz. The lumped element implementation is visible with the dotted line and the solid lines represent the distributed filter frequency response. Individual line-colours denote the S-parameters for individual coils (reflection) and between coils (transmission).**

# Four-Coil Array

## Coupling Matrix Optimization

The four-coil array was optimized for both a 2$^{nd}$-order lumped element decoupling network, realized with capacitors, as well as a distributed filter, similar to the concept illustrated in Fig. 13b. The corresponding *s*-parameters for the lumped element and distributed design are presented in Fig. 16, respectively. The optimized *s*-parameters are

given for $\omega_o = 297.2$ MHz which allows for a direct comparison to the full-wave and experimental results. The synthesized coupling matrix for the lumped element implementation is presented in Appendix A. Appendix A presents the relevant design parameters obtained from frequency scaling the coupling coefficients using (3), calculating the coupling bandwidth from (2) and using an equivalent inductance of 702 nH for the

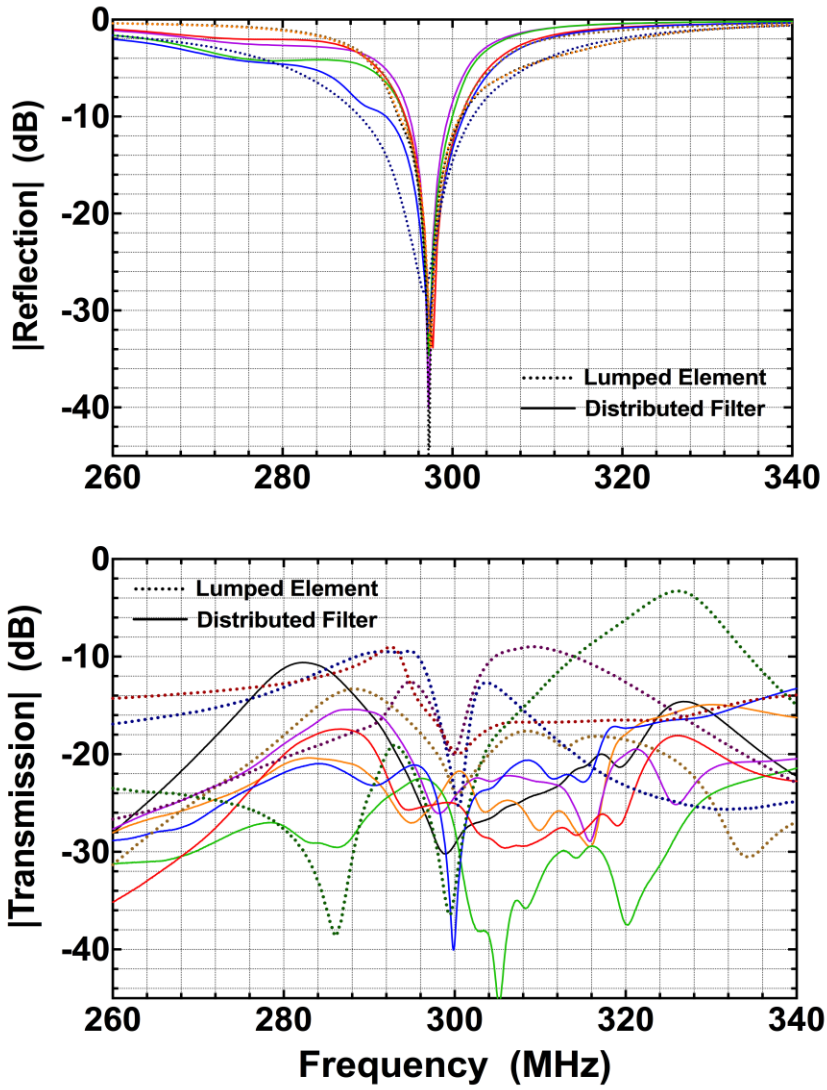


**Figure 17: S-parameters of the physical four-coil array constructed according to Fig. 6. The lumped element implementation is visible with dotted lines and solid lines represent the distributed filter frequency response. Individual line-colours denote the S-parameters for individual coils (reflection) and between coils (transmission).**

individual RF coils calculated from [27] for a flat wire track. The decoupling network capacitor values are given in pF, with RF coil tuning provided in MHz and the coupling coefficients between RF coils left for completeness.

Due to size requirements, a subset of the synthesized coupling matrix for the distributed implementation is presented in Appendix A for coils 1 to 2. The design parameters ‘A’ and ‘B’ are presented in Appendix A and evaluated using (2.21) based on the coupling values presented in Appendix A.

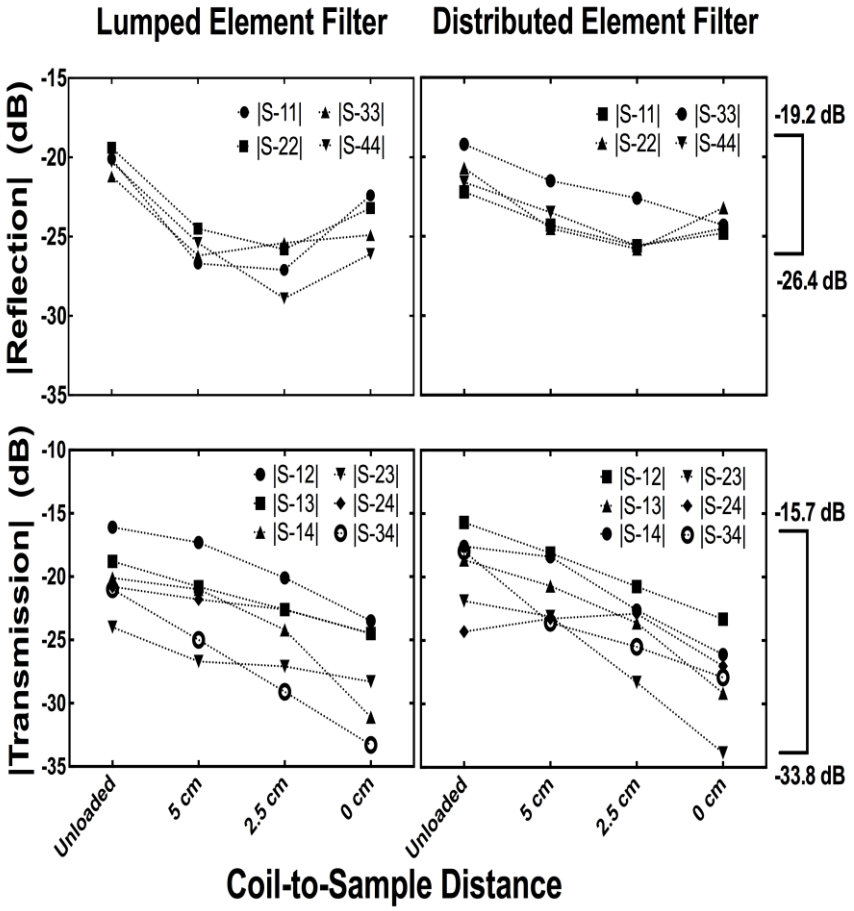


**Figure 18: S-parameter measurements for different coil-to-sample distances. Coils were re-matched for the different distances.**

## Experimental Verification

Measured *s*-parameters for the four-coil arrays are presented in Fig. 17. The design parameters corresponding to the lumped element construction are presented in Appendix A, with the design parameters for the distributed filter implementation presented in Appendix A, respectively. Measured variations in s-parameters as a function of coil-to-sample distance are presented in Fig. 18.

Mean differences between the calculated and physically constructed shunt resonators self-resonances were 1.5 ± 0.5 MHz. The mean difference in coil self-resonances was 2.1 ± 1 MHz. Coupling capacitor values demonstrated a mean difference of 1.2 ± 0.4 pF between calculated and physically constructed designs.

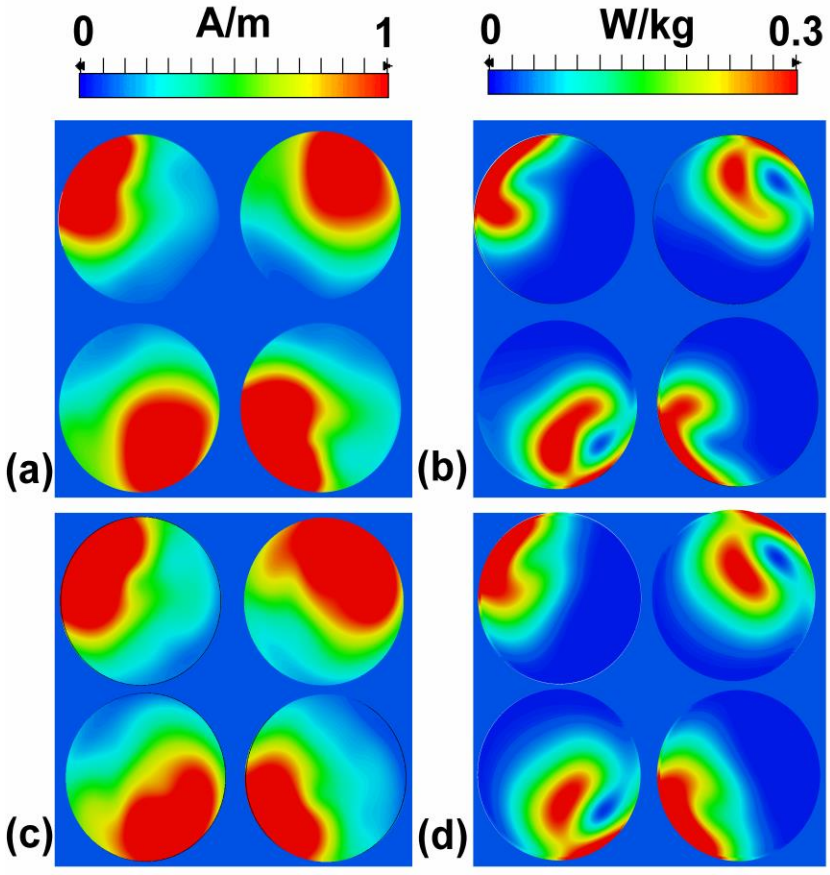


**Figure 19: Full-wave simulation results demonstrating (a), (c) magnetic field distributions, and (b), (d) 1g SAR.**

## Full-Wave Electromagnetic Simulation

Magnetic fields computed across a slice located at isocentre of the tissue-mimicking phantom are presented in Fig. 19a,c for the distributed- and lumped-element arrays, respectively. The 1g SAR field contours are similarly presented in Fig. 19b,d. Quantitative results pertaining to the 1g SAR fields across the entire phantom, as well as current probe measurements of the worst-case induced currents in the RF array coils due to mutual interactions are presented in Table II.

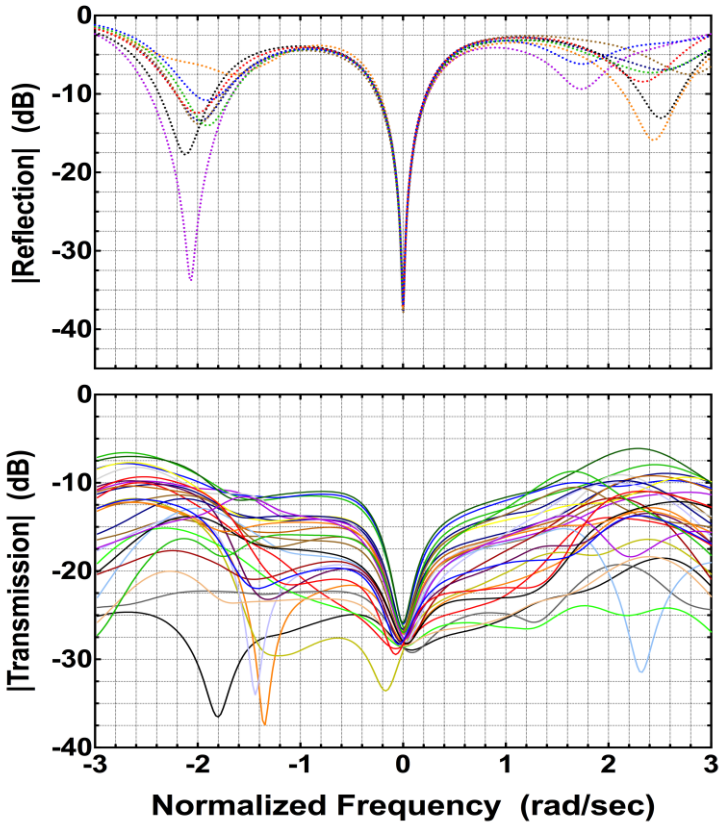


**Figure 20: Computed s-parameters for the 8-coil array decoupled with tenth-order distributed filter. Individual line-colours denote the S-parameters for individual coils (reflection) and between coils (transmission).**

**Eight-Coil Array Table II: Simulated field values for the four-coil arrays.**

| | | Decoupling Method | |
|---|---|---|---|
| | Coil | Distributed | Lumped |
| Average 1g SAR (W/kg) | 1 | 8.23e-2 | 0.101 |
| | 2 | 8.97e-2 | 0.102 |
| | 3 | 8.89e-2 | 0.101 |
| | 4 | 8.47e-2 | 0.101 |
| Peak 1g SAR (W/kg) | 1 | 0.577 | 0.582 |
| | 2 | 0.565 | 0.573 |
| | 3 | 0.540 | 0.573 |
| | 4 | 0.578 | 0.581 |
| Max Induced Current (A)* | 1 | 6.00e-3 | 4.22e-3 |
| | 2 | 2.88e-3 | 4.23e-3 |
| | 3 | 1.12e-3 | 3.96e-3 |
| | 4 | 1.95e-3 | 4.30e-3 |

*Magnitude of largest induced current due to coupling between elements corresponding to a **1 A reference.**

## Coupling Matrix Optimization

The eight-coil array was optimized for both a 2nd-order lumped element decoupling network, realized with capacitors, as well as a distributed filter, similar to the concept illustrated in Fig. 13b. The corresponding *s*-parameters, for the lumped element and

distributed designs are presented in Fig. 20 and Fig. 21, respectively. The *s*-parameters are presented for the prototype frequency span and can be scaled to the required resonant frequency for comparison, utilizing (3) for the coupling matrix entries.

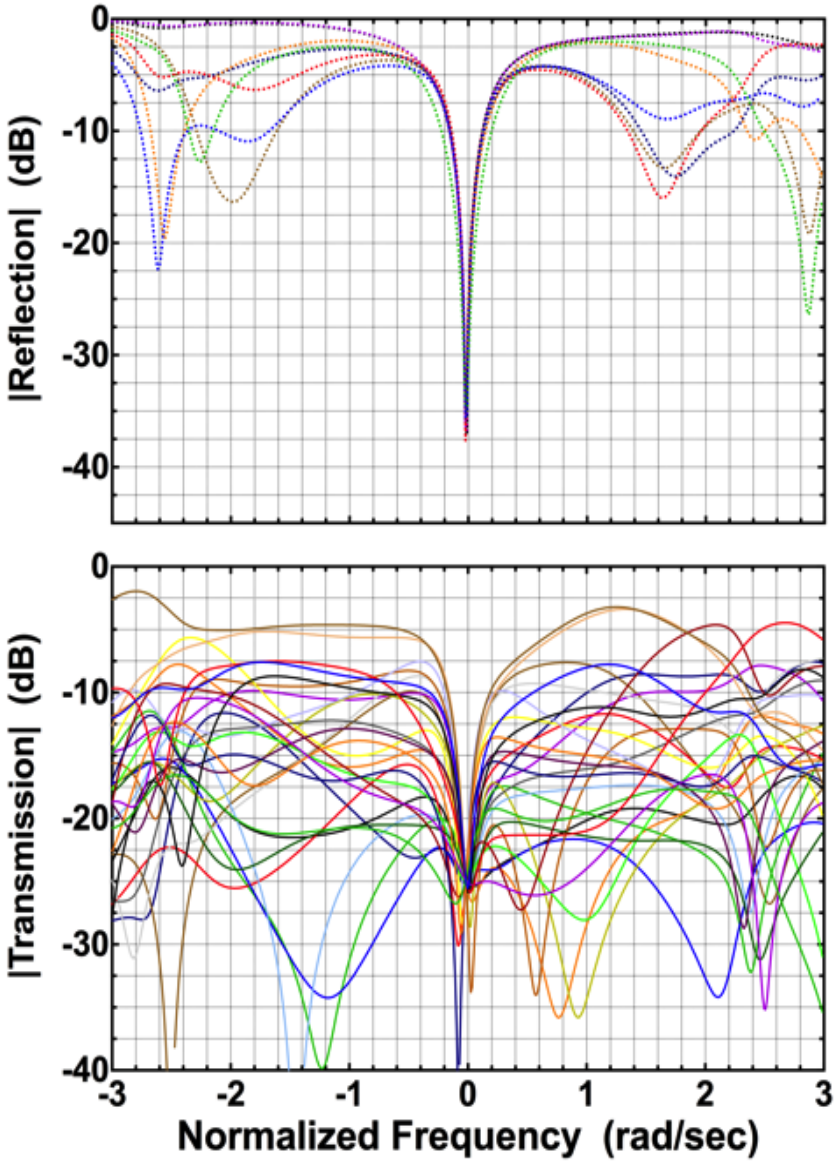


**Figure 21: Computed s-parameters for the 8-coil array decoupled with lumped elements. Individual line-colours denote the S-parameters for individual coils (reflection) and between coils (transmission).**

# Thirty-Two Coil Array

## Coupling Matrix Optimization

Similar to the four- and eight-coil array procedures, the 32-coil array was optimized for both a 2nd-order lumped-element decoupling network, realized with lumped elements, as well as a distributed filter (see Fig. 13b). The corresponding *s*-parameters for the lumped element and distributed design are presented in Fig. 22 and Fig. 23, respectively.

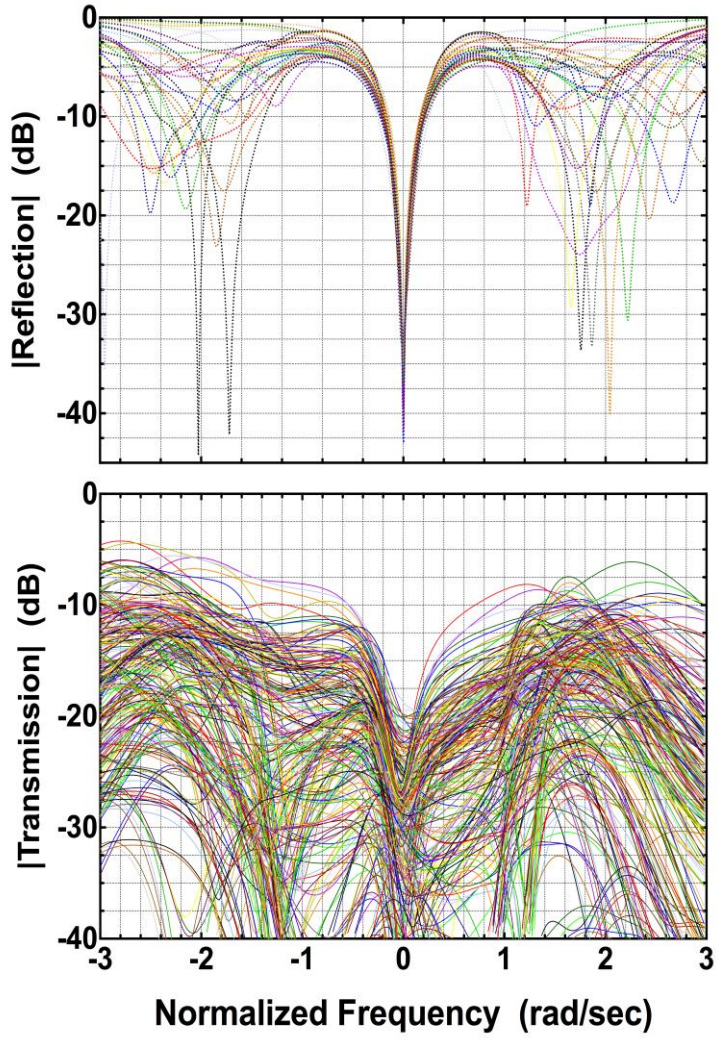


**Figure 22: Computed s-parameters for the 32-channel array decoupled with a distributed filter. Individual line-colours denote the S-parameters for individual coils (reflection) and between coils (transmission).**

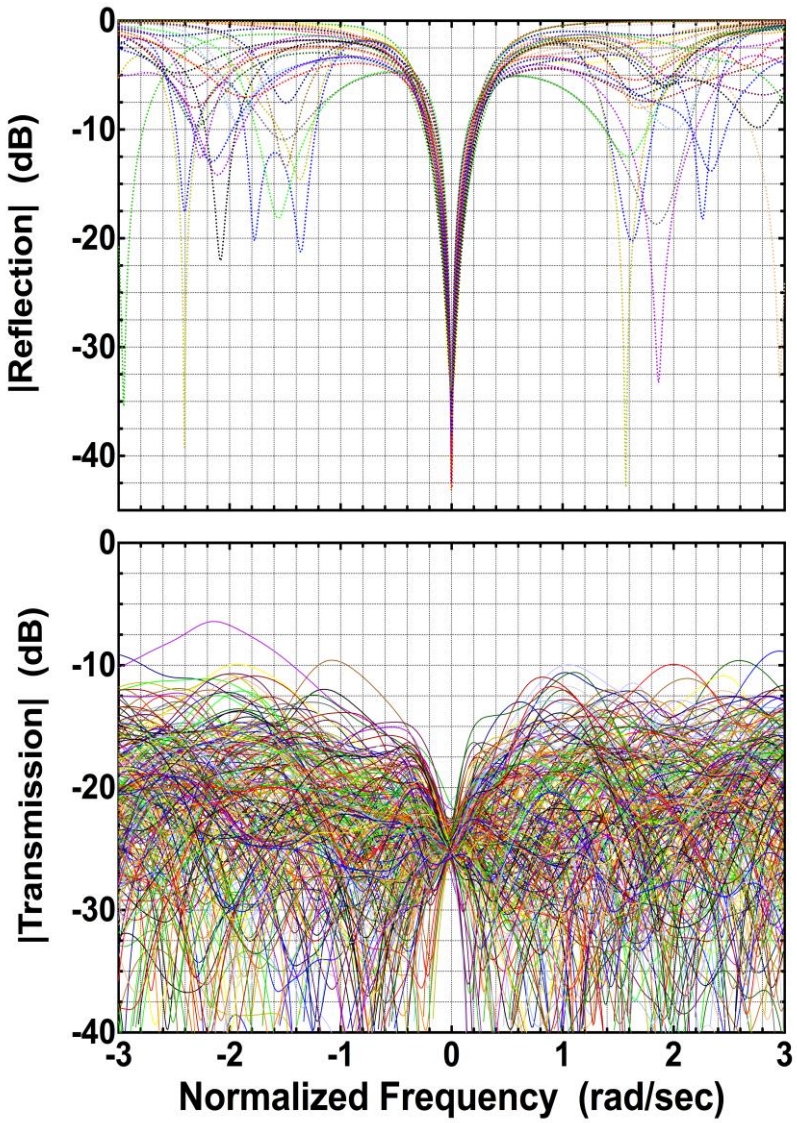


**Figure 23: Computed s-parameters for the 32-channel array decoupled with lumped elements. Individual line-colours denote the S-parameters for individual coils (reflection) and between coils (transmission).**

## Monte Carlo Simulation

Monte Carlo simulation was performed on the 32-coil array decoupled with a $2^{nd}$-order network. As shown in Fig. 24, the decoupling method, and by proxy the $L_1$-regularization procedure, used to find the optimal number of ladder stages is very stable. Both reflection and transmission coefficients remain steady throughout all trial runs. The mean and

standard deviation of the reflection and transmission coefficients from the random sampling distribution are -20.4 ± -1 dB and -20.5 ± -2 dB, respectively. In comparison, the optimal solution obtained by the nonlinear least squares algorithm had a mean reflection of -20.7 dB and transmission of -20.6 dB across the same frequency span. Therefore, the decoupling methodology can accommodate for a variety of possible changes in the array leading to a variation in coupling coefficients (load, physical deformation, etc.).

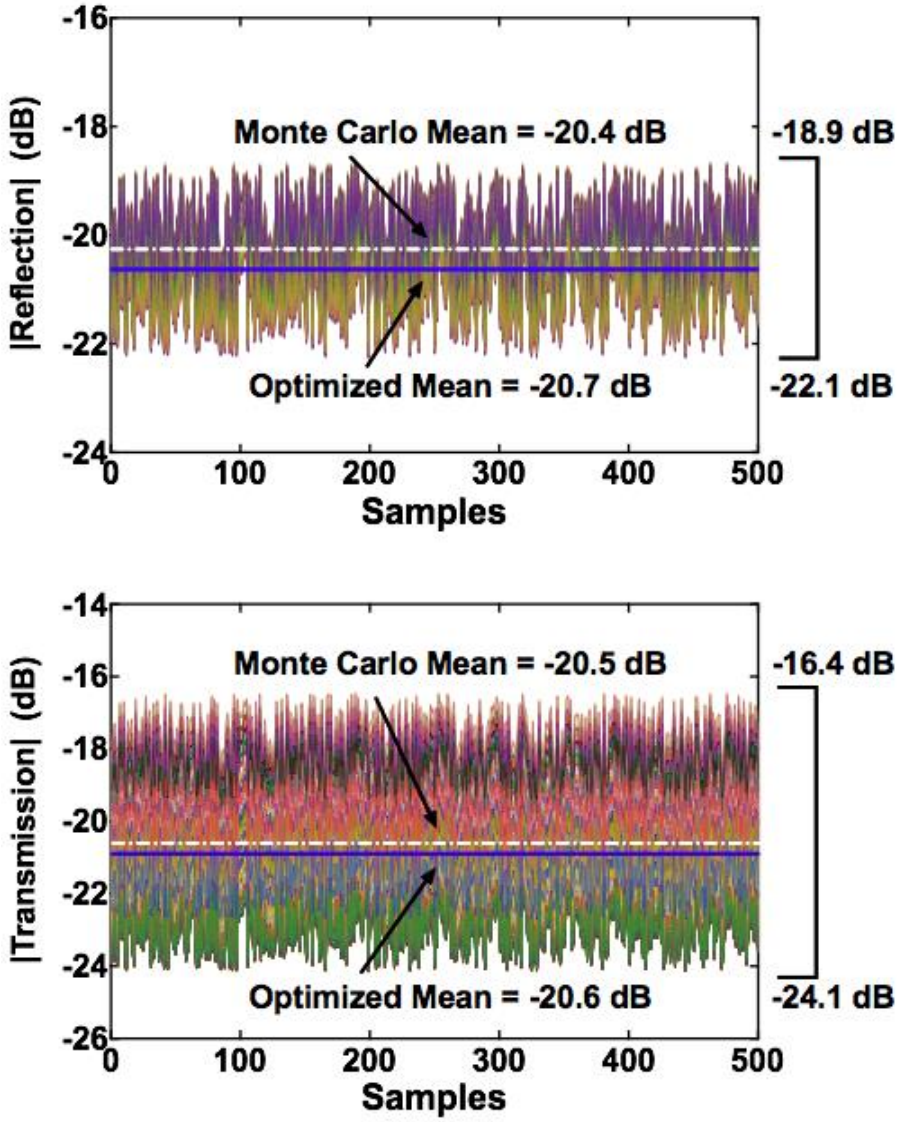


**Figure 24: Monte Carlo simulation performed by varying the coil-to-coil coupling coefficients of the 32-coil RF array with a second-order decoupling network. Coupling coefficients were distributed between 50-150% of their original value for 500 random trials.**

# Discussion

## Coupling Matrix Synthesis

The reduction of designing an RF array into a coupling matrix optimization has many potential benefits for future constructions. Most importantly, this method can compute either lumped element or geometric values that are commonly used for decoupling MRI RF arrays. Additionally, solving for the coupling coefficients in the prototype filter framework allows for arbitrary geometries and channel counts to be explored, as it does not rely on a closed-form solution to be reached. This also allows the design to be both frequency and impedance scaled for a variety of main magnetic field strengths as well as hardware interfaces. Furthermore, through converting the coupling matrix to its lumped element form or distributed filter form, it is possible to explore the sensitivity of any one form of decoupling under a variation of conditions that would affect coil-to-coil coupling. This was achieved with the Monte Carlo simulation of coil-to-coil coupling values located in a synthesized **M**.

Other than performing parametric sweeps in full-wave simulation, this solution provides a tractable way to synthesis a complex decoupling structure such as a distributed filter for a multi-port network. From optimization, a few variables can be selected in terms of filter placement in the array and can be realized from the method.

Similar studies, as seen in references [3, 9], achieve similar *s*-parameters (Fig. 16, 17, 19, 20, 22, and 23) computed here by the general coupling procedure. These frequency responses are typical of a tuned reduction in the mutual impedance between coils. However, the circuit representation presented by this study provides a very tractable framework to design decoupling networks for very dense arrays.

The relationships derived in [27] were presented but not thoroughly solved in the general case for arbitrary array constructions. Simply put, our method extends the same solution to the loop-voltage system of equations beyond the case of two coils. Similarly, the nonlinear programming approach via coupling matrix synthesis allows any decoupling interface to be included in the original system matrix, and not appended as an additional N+2 decoupling interface. This is beneficial due to the fact that located within this N+2 interface

are additional reactive terms occupying each matrix position presenting mutual impedance. In comparison to the 2-stage network placed only between adjacent coils, as is presented in this study, the N+2 interface requires potentially complex circuit realizations for array constructions with a high degree of asymmetric or several cross-coupling terms. Similarly, compensating for asymmetric coupling and arbitrary array geometry was not directly addressed by the work presented in [22], where a set of loop-voltage equations were analtyically solved for a two-coil system. As we have demonstrated in this study, the solution space for large array counts is non-smooth and potentially discontinuous which makes extending a close-form solution for two coils to a general framework non-trivial. Furthermore, the closed-form solution requires predetermining circuit realizations prior to solving the system of equations, whereas in coupling matrix synthesis, the filter design is flexible and can be physically realized with a class of well-known ladder equivalent circuits. Although the $\Pi$-network utilizing capacitor phase shifting was demonstrated in this study, equally applicable are the other coupling circuits presented and can be combined with other filter synthesis methods. This study has demonstrated the applicability of a coupling matrix procedure for a variety of complex RF array designs and concluded that the MRI electromagnetic environment does not preclude the use of advanced filter synthesis concepts [28-30] for designing RF array circuitry.

This concept of being able to decouple a wide-variety of resonating elements in an array is the strongest application of this work (see Fig. 22 and Fig. 23 for the 32-coil array). As demonstrated in [2] when performing MR at UHF ( $\geq$ 7 T), the electromagnetic fields during both transmit and receive become a mixture of both magnetic- and electric-dipole interactions. This is unlike lower field strengths, where typically magnetic-dipole interactions dominate. In an effort to achieve optimum SNR and transmit efficiency, more elaborate transmit/receive coils, that include mixtures of different resonating elements and antennae [31], have been demonstrated to better exploit these current distributions. Therefore, the coupling synthesis method is well suited for addressing the construction of these challenging arrays that will require some level of decoupling between elements not typically achieved with conventional methods.

Similar comparisons between this discussion point and other previously reported decoupling methods can also be made - the insertion of a tertiary decoupling loop [32, 33] or purely capacitive networks [4, 34, 35].

## Experimental Verification

The *s*-parameters presented in Fig. 17 demonstrate many similar characteristics to those obtained from the optimization routine (Fig. 16). Predictably, the additional resistance incurred in the physical design, as well as minor additional sources of coupling between elements results in perturbations in the measured response. However, the decoupling achieved about $\omega_o$ was beyond the -20 dB level for all transmission coefficients, with all reflection coefficients characterizing a tune-and-match for all elements at $\omega_o$. From both optimization and measurements, the distributed filter demonstrated a wider decoupling bandwidth in comparison to the lumped element implementation. This is due to the greater number of distributed filter resonators in comparison to a 2$^{nd}$-order decoupling network. For the distributed filter, the additional coupling terms between resonators and resonator-to-coil have the effect of broadening the decoupling bandwidth.

As demonstrated in Fig. 18, when decreasing the sample-to-coil distance, coupling monotonically decreased due to additional dissipative loss incurred in the more tightly place conductive load. Due to the increased loading, impedance match was similarly affected. However, once re-matching of the array elements were completed, the decoupling was minimally perturbed and demonstrated a steadily improving response regardless of the introduction of additional coupling pathways via conductive interactions through the phantom. For the most typical RF array constructions, separation distances of 2.5-cm and 5-cm demonstrate strong decoupling.

## Full-Wave Electromagnetic Simulation

As demonstrated in Fig. 19, the arrays constructed with the coupling synthesis method display distinct electromagnetic field profiles attributed to a low level of mutual interaction. Provided that the SAR field profiles provided in Fig. 19 are a function of the electric field at those points, the minimal interaction of coil elements has a similar effect on the electric field distribution as it does on the magnetic field distribution. This minimal

interaction is further demonstrated by the current probe measurements provided in Table II that illustrate very low induced current magnitudes. Qualitatively; the magnetic and SAR field profiles show agreement across decoupling implementations, with each coil in both array displaying unique sensitivity profiles – important for both parallel imaging performance, as well as parallel transmission.

## Conclusion

This study confirms the applicability of coupling matrix synthesis as a promising method for the design of multi-coil RF arrays used in MRI. This study presents a multi-port equivalent coupled circuit and performs analysis in the prototype-filter domain. By generating a series of Chebyshev Type I polynomials and frequency points to minimize transmission, this study demonstrates the ability of a nonlinear least squares algorithm that returns a coupling matrix that can be physically realized. Physical measurements confirm the results demonstrate high decoupling values between coils located in an array.

The coupling matrix synthesis approach provides exciting opportunities to design dense RF arrays, mixing multiple types of resonant elements and antennae, with highly decoupled coils and provide further insight into RF array interactions.

# Chapter 3

# MRI RF Array Decoupling Method with Magnetic Wall Distributed Filters

In this chapter, the general framework developed in Chapter 2 is extended to the construction of specific decoupling structures. Further electromagnetic insights are provided on the theory and operation of these classes of distributed filters. This chapter is derived from the manuscript, "MRI RF Array Decoupling Method with Magnetic Wall Distributed Filters" published in IEEE Transactions on Medical Imaging in April 2015.

## Introduction

This study presents the ability of a planar RF filter to decouple elements located inside a transmit array. The decoupling method was implemented in the form of a distributed filter, inspired by the periodic design of frequency selective surface (FSS) that utilize non-magnetic conductors. Typically, an FSS is designed as a cascaded array of 'unit cells' composed of self-resonant structures. The self-resonance of each unit cell is typically equivalent along the entire array. We refer to this design as a "magnetic-wall" (MW). The geometry and miniaturization possibilities of MWs make them attractive candidates for use in the space-limited environment of an MRI coil.

The principle of MW operation is illustrated with an equivalent circuit analysis that accounts for an arbitrary MW design and a chosen number of RF coils. Augmenting the theoretical discussion, full-wave electromagnetic simulations are performed in CST Microwave Studio (Darmstadt, Germany) to confirm results obtained from the equivalent network. Both results are experimentally verified with a physical MW filter design. The physical MW was implemented into a sample RF array to examine the decoupling of both first-order coupling and higher-order coupling arising from cross-coupling terms between three RF coils.

## General RF Coil Coupling

Various types of coil elements can be used to construct transmit arrays such as loops (square, circular, etc.), transmission lines, or dipoles. Without loss of generality, loop coils

similar to the one shown in Fig. 25 will be used to illustrate the decoupling concept. These coils are typically impedance matched (using $C_M$) to the rest of the RF transmit chain through a 50-Ω feeding line. A balanced-to-unbalanced transformer (balun) is usually used at the input of the loop. The loop can be matched and tuned using a variety of methods such as an L-network composed of series and shunt capacitors at the inputs. The series capacitor is commonly distributed around the loop as shown in Fig. 25 ($C_1$ and $C_2$). The loop can be tuned to the desired frequency by varying $C_T$. Fig. 25 shows a building block of an RF array showing two identical loop coils in the xz-plane (z being in the direction of the main magnetic field, $B_o$) without any decoupling method applied.

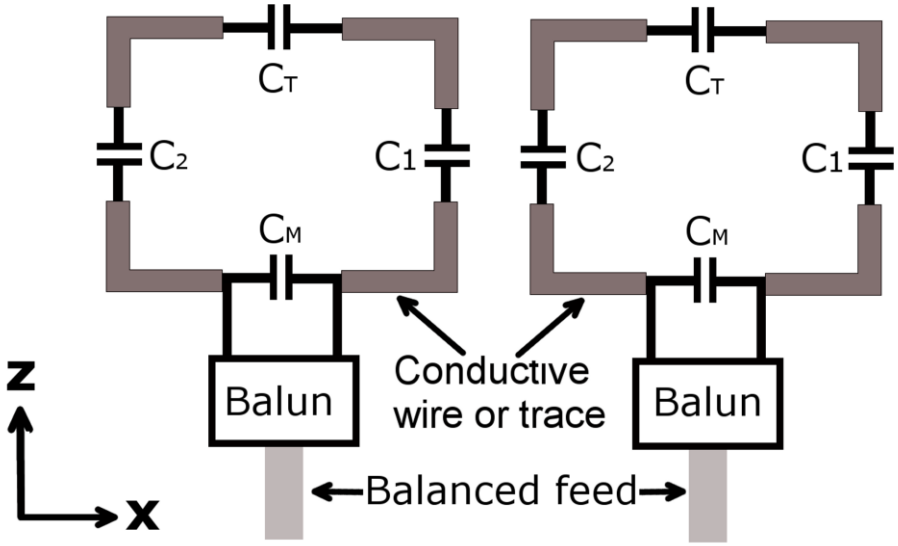


**Figure 25: Magnetic wall proof-of-principle setup.**

As elaborated upon in Section 1.3, due to the presence of magnetic flux linkage and stray capacitance emanating from RF coils in the array, interfering voltages develop across the terminals of all input ports in the array. This results in the production of tertiary magnetic fields from coils that may be otherwise un-driven. The corresponding reflection coefficients measured at the input of these coupled terminals show distinct 'mode splitting' since the coils (resonators) are tightly coupled (see Section 1.3 for derivation). For two RF coils, this splitting can be considered ‘first-order coupling’. The addition of more RF coils

to the two-coil setup would manifest itself as additional modes in the frequency spectrum of both the reflection and transmission coefficients. This cross coupling between coils that are not directly adjacent is considered ‘higher-order coupling’ (the order of which is determined by the number of coils in the full array). Under these coupled condition, each individual RF coil is detuned and mismatched at the Larmor frequency (298.2 MHz), rendering them inefficient for transmitting at this desired frequency.

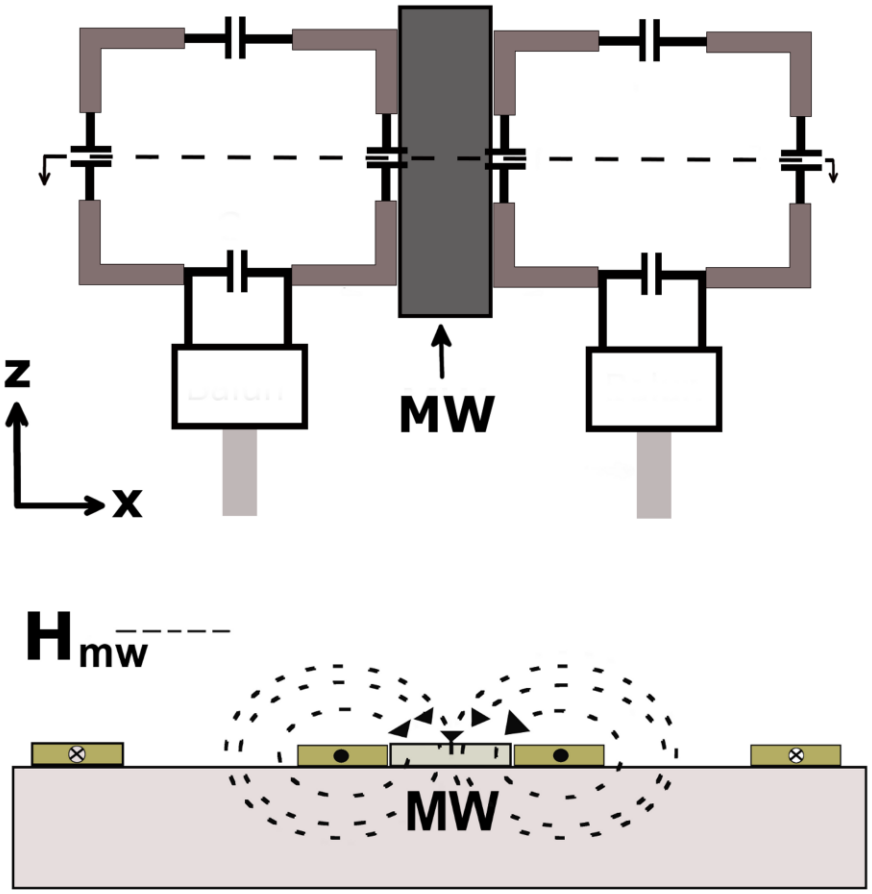


**Figure 26: Magnetic wall theory of operation.**

## Magnetic Wall Decoupling Concept

To reduce the mutual coupling between transmit array coils, a magnetic wall (MW) is inserted between the loops (see Fig 26). The magnetic wall is a miniaturized distributed

filter that is coupled to the array and designed to produce a stopband between the terminals of the RF coils. The stopband is centered about the Larmor frequency. By eliminating the transmission of energy between the terminals of individual coils, the tune and match of the array is restored to a singular resonance with high efficiency at the design frequency. Notably, the transmitter driving it, thus improving the fidelity of the transmitted waveforms, now solely determines the loop voltage.

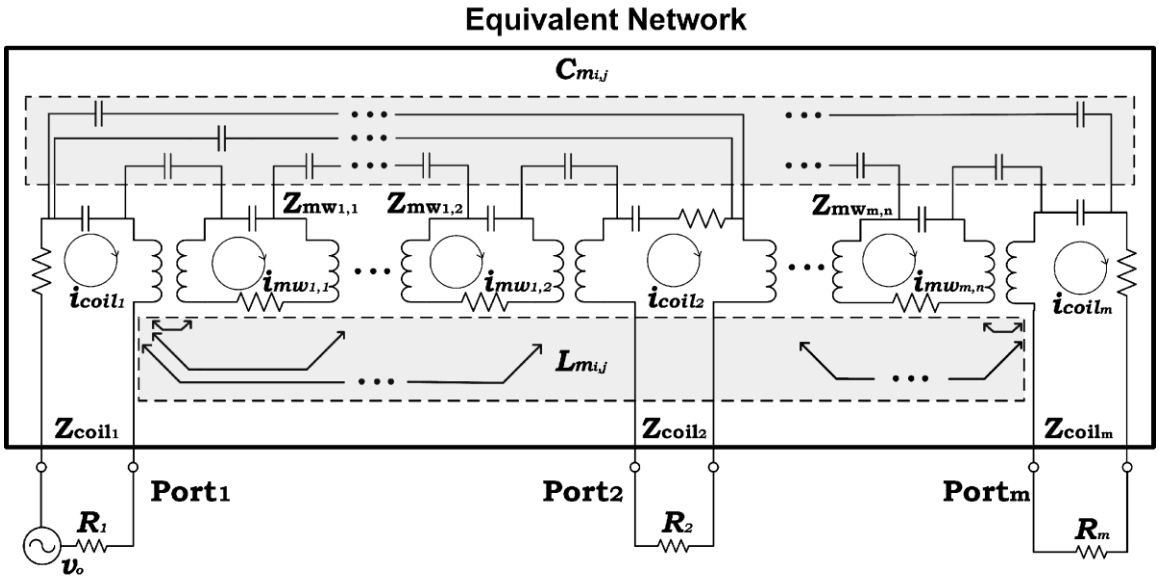


**Figure 27: Magnetic wall equivalent-circuit analysis.**

# THEORY

## A. Magnetic Wall Design

As seen in Fig. 26, the concept of the MW is to place a miniaturized filter between adjacent RF coils. The MW is edge-coupled to the adjacent RF coils via electric and magnetic coupling. The MW is comprised of a linear array of 'unit cells' that provide a decoupling response within a bandwidth that is determined by the number and geometry of the unit cells located inside a full MW. Each unit cell in the MW is comprised of a fundamental conductor geometry that is commonly referred to as either a 'spiral resonator (SR)' or a 'spiral inductor (SI)'. These tight windings have the ability for significant

miniaturization while resonating in the MHz regime required for MRI decoupling [36]. At higher GHz frequency of operation, split ring resonators (SRRs) and complementary split ring resonators (CSRRs) have been extensively studied in literature for their operation in high-frequency circuit design as effective noise suppressing elements [37]. They have also been used as filters for providing stopband and passband characteristics when the individual resonant conductors are tuned to the same resonant frequency [38]. This approach of tuning the individual resonant conductors ('unit cells') to the same resonant frequency is extended to the full RF array where the MW is comprised of an array of unit cells designed to resonate at the Larmor frequency of the RF coils.

## Equivalent Network Model

To analyze the MW operating inside an array of RF coils, the network model in Fig. 27 is employed. Here, the equivalent circuit presented in Chapter 2 is modified to consists of 'n' resonating unit cells located inside an individual MW and 'm' RF coils (Fig. 27 - $Z_{mw}$ and $Z_{coil}$, respectively). The total number of MWs is assigned to be equivalent to the number of 'm' coils. The mesh of the coupled network can be written as

$$\begin{bmatrix} V_1 \\ \vdots \\ V_{n+m} \end{bmatrix} = [\boldsymbol{Z}] \begin{bmatrix} i_1 \\ \vdots \\ i_{n+m} \end{bmatrix} \tag{3.1}.$$

For the general case of 'n' unit cells and 'm' RF coils the impedance matrix [**Z**] is

$$\begin{bmatrix} Z_{coil_1} & Z_{coil_1,mw_{1,1}} & \cdots & Z_{coil_1,mw_{m,n}} & Z_{coil_1,coil_m} \\ Z_{mw_{1,1},coil_1} & Z_{mw_{1,1}} & \cdots & Z_{mw_{1,1},mw_{m,n}} & Z_{mw_{1,1},coil_m} \\ \vdots & \vdots & \ddots & \vdots & \vdots \\ Z_{mw_{m,n},coil_1} & Z_{mw_{m,n},mw_{1,1}} & \cdots & Z_{mw_{m,n}} & Z_{mw_{m,n},coil_m} \\ Z_{coil_m,coil_1} & Z_{coil_m,mw_{1,1}} & \cdots & Z_{coil_m,mw_{m,n}} & Z_{coil_m} \end{bmatrix} \tag{3.2}.$$

The self-impedance terms are written as

$$Z_{coil_m} = R_{coil_m} + j\omega L_{coil_m} + \frac{1}{j\omega C_{coil_m}} \tag{3.3a}$$

$$Z_{mw_{m,n}} = R_{mw_{m,n}} + j\omega L_{mw_{m,n}} + \frac{1}{j\omega C_{mw_{m,n}}} \quad (3.3b).$$

Following from [39], the stopband for a coupled MW-like structure is centered about the resonant frequency of the individual unit cells that compose the full MW. Assuming individual MW unit cells are all tuned to the same self-resonant frequency that is equivalent to the resonant frequency of the RF coils in the array, (3.2) can be transformed to

$$[\boldsymbol{Z}] = \omega_o\left(L_c\overline{[\boldsymbol{Z_c}]} + L_{mw}\overline{[\boldsymbol{Z_{mw}}]}\right) - j\omega\overline{[\boldsymbol{Z_m}]} \quad (3.4)$$

where the normalized impedance terms are defined as

$$\overline{[\boldsymbol{Z_c}]}_{i,j} = \begin{cases} 0 & for\ i \neq j \\ q_{coil_m} + \delta & for\ i = j\ and\ i,j \neq n \end{cases} \quad (3.5a)$$

$$\overline{[\boldsymbol{Z_{mw}}]}_{i,j} = \begin{cases} 0 & for\ i \neq j \\ q_{mw_{m,n}} + \delta & for\ i = i\ and\ i,j \neq m \end{cases} \quad (3.5b)$$

$$\overline{[\boldsymbol{Z_m}]} = \begin{bmatrix} 0 & M_{1,2} & \dots & M_{i,j} \\ M_{2,1} & \ddots & & \vdots \\ \vdots & & \ddots & \vdots \\ M_{j,i} & \dots & \cdots & 0 \end{bmatrix} \quad (3.5c).$$

Terms in (3.5a) and (3.5b) are defined as

$$q_{coil_m} = \frac{R_{coil_m}}{\omega_o L_{coil_m}} \quad (3.6a)$$

$$q_{mw_{m,n}} = \frac{R_{mw_{m,n}}}{\omega_o L_{mw_{m,n}}} \quad (3.6b)$$

$$\delta = j\left(\frac{\omega}{\omega_o} - \frac{\omega_o}{\omega}\right) \quad (3.6c).$$

Term $\omega_o$ is the resonant frequency of the individual MW unit cells and the RF coils. Self-impedance terms (3.3a) and (3.3b) are written in terms of quality factor in (3.6a) and (3.6b) where $L_{coil_m}$ and $L_{mw_{m,n}}$ are the inductances of the individual RF coils and MW unit cells, respectively. Resistance terms in (6a) and (6b) are similarly denoted.

The off-diagonal coupling terms in (3.5c) can be written in terms of a coupling coefficient which includes both electric and magnetic coupling [25]

$$M_{i,j} = \left(k_{m_{i,j}}\sqrt{L_{i,j}L_{i,j}} - k_{e_{i,j}}\sqrt{C_{i,j}C_{i,j}}\right) \tag{3.8}.$$

Following from Fig. 27, *S*-parameters can be extracted from the terminated RF coil outputs and expressed in terms of (4)

$$S_{m,m} = Z_o - \frac{2}{q_{coil_m}}[\boldsymbol{Z}]^{-1}_{\boldsymbol{m,m}} \tag{3.9a}$$

$$S_{1,m} = Z_o - \frac{2}{\sqrt{q_{coil_1}q_{coil_m}}}[\boldsymbol{Z}]^{-1}_{\boldsymbol{1,m}} \tag{3.9b}.$$

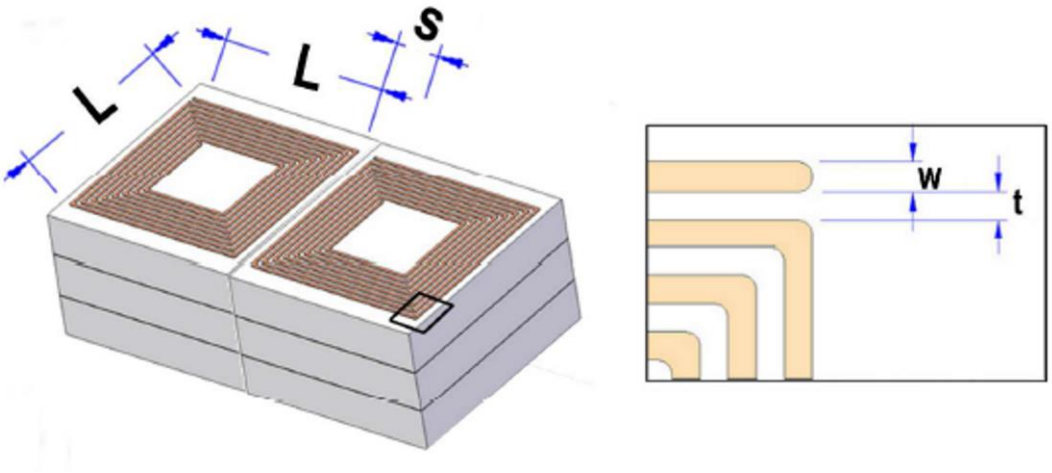


**Figure 28: Magnetic wall dimensions.**

## Methods

All S-parameters, MW frequency responses, and RF-coil frequencies were measured with a network analyzer (Agilent Technologies, model E5071C). Full-wave EM simulations were performed using commercially available software: CST Microwave Studio (Darmstadt, Germany).

## Magnetic Wall Design

A MW filter was designed for theoretical, full-wave and experimental analysis. The design of the MW was completed in a two-fold process. In order to achieve an individual unit cell with a self-resonance near the Larmor frequency of the RF coils, while still capable of being constructed with conventional PCB technology, a stack of identical conductors was required (Fig. 28). This unit cell has an equivalent circuit (Fig. 29a) that accounts for magnetic interactions between the stacks of identical conductors. The inductance matrix for this circuit is

$$L_{mw} = \begin{bmatrix} L_1 & M_{12} & M_{13} \\ M_{21} & L_2 & M_{23} \\ M_{31} & M_{32} & L_3 \end{bmatrix} \tag{3.10}$$

where the following assumptions: (a) uniform magnetic coupling is the dominate source of coupling throughout a single unit cell ($k_{12} = 0.99$, $k_{13} = 0.97$, $k_{23} = 0.98$); and (b) equivalent inductance of individual spiral inductors ($L_1 = L_2 = L_3$) yield a total inductance of

$$L_{mw} = 1.97L_1 \tag{3.11}.$$

Therefore, the total inductance of the MW can be determined by calculating the inductance of a single spiral and then solving (3.11). Similarly, the total capacitance was calculated based upon the self-capacitance of each resonator ($C_1 = C_2 = C_3$). This yields the following expression for resonance

$$\omega_{mw} = \frac{1}{\sqrt{5.91L_1C_1}} \tag{3.12}$$

Given specific the geometry of the spiral resonators, the inductance and capacitance values are directly calculated via equations (3.11) and (3.12) presented in [40] for $L_1$ and $C_1$, respectively. The initial estimates for geometric parameters to achieve resonance at 298.2 MHz with (12) were taken from Fig. 4 of [28] for the case of 8 conductor turns.

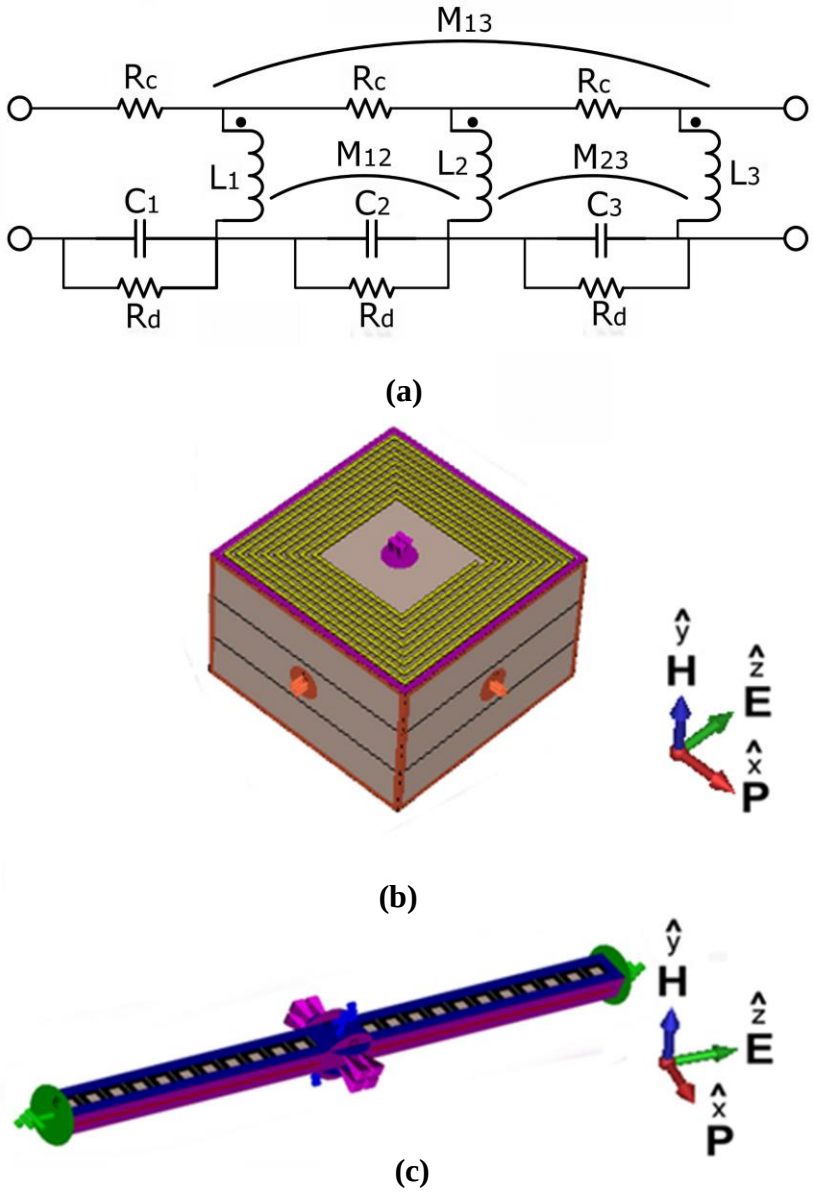


**Figure 29: (a) Magnetic wall equivalent circuit, (b) unit cell as constructed in CST Microwave Studio and (c) electromagnetic boundary conditions applied to the full magnetic wall construction.**

To confirm the equivalent circuit results, the geometric values for the stacked spirals (number of windings, conductor outside and inside diameters, dielectric constant and thickness) were used to construct an initial model inside CST where the final optimization of the structure for decoupling was performed. This method ensured that the MW

parameters were sufficiently close a conductor geometry that resonates at the Larmor frequency. Therefore, the optimization time was reduced and fed the simulation space a well-conditioned initial estimate.

The number of conductor windings, dielectric thickness, and dielectric constant were kept constant in the parametric simulation of the MW. The other geometric parameters (in reference to Fig. 28 - conductor outside diameter 'L', spacing 't' and width 'w') assigned as variables. Initial values for the optimization were assigned from solving (3.12) and given a minimum and maximum bound of 15% of the original value within a parameter search was performed for min{$S_{11}$(298.2 MHz)}. Unit-cell electromagnetic boundary conditions were placed in the positive and negative x- and z-directions (see Fig. 30b). Additional air ($\varepsilon_r$=1 and $\mu_r$=1) was added above and below the MW in the y-direction with open boundary conditions placed at the y-axis extents. The dominant TE Floquet port-mode excitation was used in the positive and negative y-direction with the incident magnetic field (**H**) rotated perpendicular to the xz-plane of the MW (see Fig. 29b for the incident field orientation). *S*-parameters were extracted from waveguide ports located at the positive and negative y-directions, with phase de-embedding applied. The MW was physically constructed with common PCB manufacturing processes (Advanced Circuits, Aurora, AZ).

## Equivalent Circuit Network

The inductance term $L_{coil_m}$ from (3.5) were calculated based on formulas presented in [27] for a flat PCB track. The values for conductor rectangular geometry (20 x 6.35 cm), track width (0.32 cm) and thickness (1 oz. copper) were based on the physical design of the RF coils (Fig. 30) and were used to compute $L_{coil_m}$. Term $L_{mw_{m,n}}$ was computed from (3.12) with $L_1$ calculated from the 'modified wheeler' expression in [41] for the dimensions of the conductor in the MW filter (Fig. 28). Capacitance terms were calculated based on both the MW and the RF coils resonating at 298.2 MHz. Resistance terms in (3.5) were approximated via sheet resistance for flat copper PCB tracks based on the physical design of the MW (Fig. 28) and RF coils (Fig. 30).

Coupling terms in (3.8) for interaction between individual MW unit cells were calculated from equations (17) and (18) in [25] for respective electric and magnetic

couplings of loop resonators. The coupling coefficient between a single MW unit cell ($mw_{m,n}$) and a single RF coil ($coil_m$), as well as between the RF coils ($coil_m, coil_{m+1}$), were calculated from (3.8) with the following definitions

$$k_{e_{i,j}} = \frac{\int_V \mathbf{E}_{\boldsymbol{coil_m}} \cdot \mathbf{E}_{\boldsymbol{mw_{m,n}}}\, dv}{\sqrt{\int_V \left|\mathbf{E}_{\boldsymbol{coil_m}}\right|^2 dv \times \int_V \left|\mathbf{E}_{\boldsymbol{mw_{m,n}}}\right|^2 dv}} \tag{3.13a}$$

$$k_{m_{i,j}} = \frac{\int_V \mu_r \mu_o\, \mathbf{H}_{\boldsymbol{coil_m}} \cdot \mathbf{H}_{\boldsymbol{mw_{m,n}}}\, dv}{\sqrt{\int_V \mu_r \mu_o \left|\mathbf{H}_{\boldsymbol{coil_m}}\right|^2 dv \times \int_V \mu_r \mu_o \left|\mathbf{H}_{\boldsymbol{mw_{m,n}}}\right|^2 dv}} \tag{3.13b}.$$

As seen in (3.13), the circuit terms $C_{m_{i,j}}$ and $L_{m_{i,j}}$ from Fig. 27 are represented with volume integrals over their respective fields responsible for coupling. Computation of the electric and magnetic fields was performed inside CST with an identical 0.5-$W_{rms}$ Gaussian windowed-pulse. Input power was normalized to the accepted power at each respective port for the MW and RF coil ensuring each field was scaled to the same unit excitation. The dimensions of the simulation environment were sized to encompass the full physical realization of the MW filter and RF coils. Therefore, volume and gridding was kept constant for computing each field prior to performing the integration required in (3.13). For MW unit cell to RF coil coupling, one simulation was performed and coupling between all individual MW unit cells and RF coils were assumed to be equivalent. Coupling coefficients were confirmed with measurements using the following definition for the coupling coefficient

$$\mathrm{k_{i,j}} = \frac{f_2^2 - f_1^2}{f_2^2 + f_1^2} \tag{3.14}$$

where $f_2^2$ and $f_1^2$ correspond to the upper and lower resonant peaks resultant from coupling between RF coils as well as between RF coils and a MW unit cell.

## Full-Wave filter Simulation

Two full-wave computations were performed. The first simulation was a waveguide excitation performed on the full MW filter to analyze the reflection and transmission coefficients for a perpendicular magnetic field (**H**). This excitation is an approximate model based on the orientation of the magnetic field (**H**) and electric field (**E**) present between two adjacent transmit coils (see Fig. 26) that result in the mutual coupling terms, $M_{i,j}$, in (3.8). The MW was constructed according to dimensions provided in the truncated magnetic wall figure presented in Fig. 29 and was composed of 1-oz copper (lossy) metallization and adhered to a 1.52-mm-thick Rogers 4350B high-frequency dielectric. The full 27-unit cell array was realized in the simulation space. Waveguide ports were located on the positive and negative extents of the x-axis. Magnetic ($M_t$=0) and electric ($E_t$=0) boundary conditions were located on the positive and negative y- and z-axes, respectively. These boundary conditions produced a linearly polarized TEM waveguide mode inside the cavity along the x-direction. The magnetic field (**H**) was oscillating along the y-axis, with the electric field (**E**) oscillating along the z-axis. The orientation of the MW, waveguide ports and boundary conditions in CST are provided in Fig. 29c. Computation was performed in the frequency domain. Both waveguide ports were driven with a 0.5-$W_{rms}$ Gaussian-windowed pulse. Phase de-embedding was applied to each waveguide port, accommodating for the phase shift occurring between the structure and each port. Waveguide ports were normalized to free-space impedance in accordance with the field lines presented in Fig. 26.

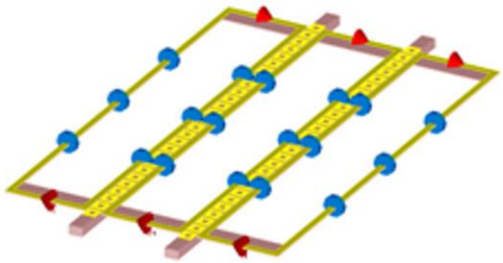

**(a)**

**(b)**

**Figure 30: (a) Magnetic wall EM simulation setup and (b) experimental setup.**

The second simulation was performed to analyze the *in situ* decoupling capability of the MW. This was completed with a 0.5-$W_{rms}$ driven three-port transient simulation performed with three RF coils (20 × 6.35 cm) placed in plane with two MW filters. The MW filter was composed of 1-oz copper (lossy) metallization, and adhered to a 1.52-mm-thick Rogers 4350B high-frequency dielectric. Similarly, the transmit coils were composed of a pure-copper conductor and a G-10 dielectric substrate [42]. The simulation setup corresponding to the full-wave filter analysis is presented in Fig. 30a. Each transmit coil was tuned and matched to 298.2 MHz.

Dissipative power losses occurring inside the MW filter were calculated across the frequency range of the simulation. The power losses incurred in the MW were then

compared to several identical three-coil systems that included conventional decoupling techniques: decoupling capacitor, decoupling inductor, and coil overlap. Both the capacitively decoupled and inductively decoupled three-coil systems included an equivalent series resistance (ESR) for the decoupling coil of 0.1 Ω. Although a direct power dissipation comparison between the MW method and simple coil overlap was not generally applicable, a comparison between power losses due to coupling was performed ($|\boldsymbol{\tau}|^2$). The highest value for the transmission coefficient between all three RF coils was used as the value for $|\boldsymbol{\tau}|^2$. The optimal overlap of the three RF coils was obtained inside CST using the built-in parametric optimizer. The power dissipation simulations were used to compare the relative efficiency of a RF array decoupled with a MW filter to that conventionally decoupled. All simulations were performed unloaded.

### Experimental Validation

A physical realization of the simulation study carried out in CST was performed to verify simulation results. The measurements were performed using the identical experimental setup as described in the Full-Wave Filter Analysis section (see Fig. 30b), with three RF coils (20 × 6.35 cm) placed adjacent to each MW filter. Each transmit coil was tuned and matched to 298.2 MHz. MW's (see Fig. 28 for dimensions) were placed between the three RF coils. The *s*-parameter measurements were then correlated to those extracted from the simulation and calculated with the equivalent network.

## Results

### Magnetic Wall Filter

The final dimensions and geometry of the MW are presented in Fig. 28. Following the parametric optimization for dimensions 'L', 's', 'w', and 't' as outlined in the Methods section, the unit cell of the MW achieved best decoupling when tuned to the Larmor frequency corresponding to dimensions given in Fig. 28.

The simulation setup corresponding to the transmission and reflection analysis of the full-wave filter analysis is presented in Fig. 29c. The simulated filtering response of the MW is presented with reflection ($|S_{11}|$) and transmission ($|S_{12}|$) coefficients in Fig. 31. As demonstrated in Fig. 31, $|S_{11}|$ at 298.2 MHz is -0.4 dB, with $|S_{12}|$ achieving -26 dB, corresponding to an effective stopband response when excited with a field similar to that present between RF coils. At the -20 dB stopband roll-off points, the MW achieves a 15-MHz bandwidth about the Larmor frequency. Although this simulation illustrates a clear bandstop response to an incident perpendicular magnetic field and parallel electric field, the variation in vector field between an actual RF coil and the MW is typically not so rigidly defined. This will alter the eventual decoupling response and was studied further in the full RF array implementation of the MW.

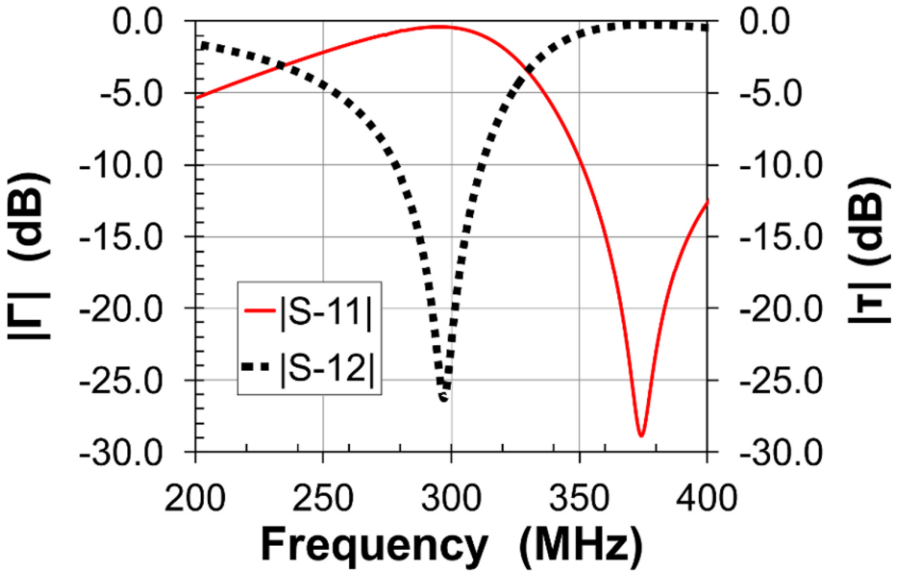


**Figure 31: Simulated s-parameters of magnetic wall**

Due to manufacturing tolerances, the physical MW unit cell with dimensions corresponding to Fig. 28, resonated at a frequency of 304 MHz with a FWHM of 15 MHz. The resonant bandwidth ($\Delta\omega$) was 35 MHz centered about 298.2 MHz. When unit cells were arranged in a linear, periodic array to form a MW, the individual resonance was centered about 297 MHz due to coupling in the full structure. This corresponded to a measured coupling coefficient between individual MW unit cells of $m_{mw_{m,n},mw_{m,n+1}} =$

$-0.047$. Although the individual structures were not identically tuned to the Larmor frequency, the bandwidth was still suitable for decoupling in the experimental verification.

## Equivalent Network Circuit

The calculated *s*-parameters corresponding to Fig. 30 for the 3-coil array are presented in Fig. 32. The coupling matrix from (3.8) was realized with terms for adjacent unit cell coupling, coil-to-coil coupling and coil-to-MW unit cell coupling. The coupling coefficients used to populate (3.8) are summarized in Table III.

**Table III: Coupling coefficients for magnetic proof-of-principle**

| | **Coupling Coefficients** | | |
|---|---|---|---|
| | $k_{e_{i,j}}$ | $k_{m_{i,j}}$ | $k_{i,j}$ |
| $m_{Coil_1,Coil_2}, m_{Coil_2,Coi}$ | 0.0183 | 0.0916 | 0.0733 |
| $m_{Coil_1,Coil_3}$ | 0.006 | 0.0519 | 0.0459 |
| $m_{Coil_1,mw_{1,n}}, m_{Coil_2,mv}$ $m_{Coil_3,mw_{2,n}}, m_{Coil_2,mv}$ | 0.0232 | 0.0013 | -0.0219 |
| $m_{Coil_1,mw_{2,n}}, m_{Coil_3,mv}$ | 0.0021 | 0.0000732 | -0.00203 |
| $m_{mw_{m,n},mw_{m,n+1}}$ | 0.0489 | 0.00348 | -0.0454 |

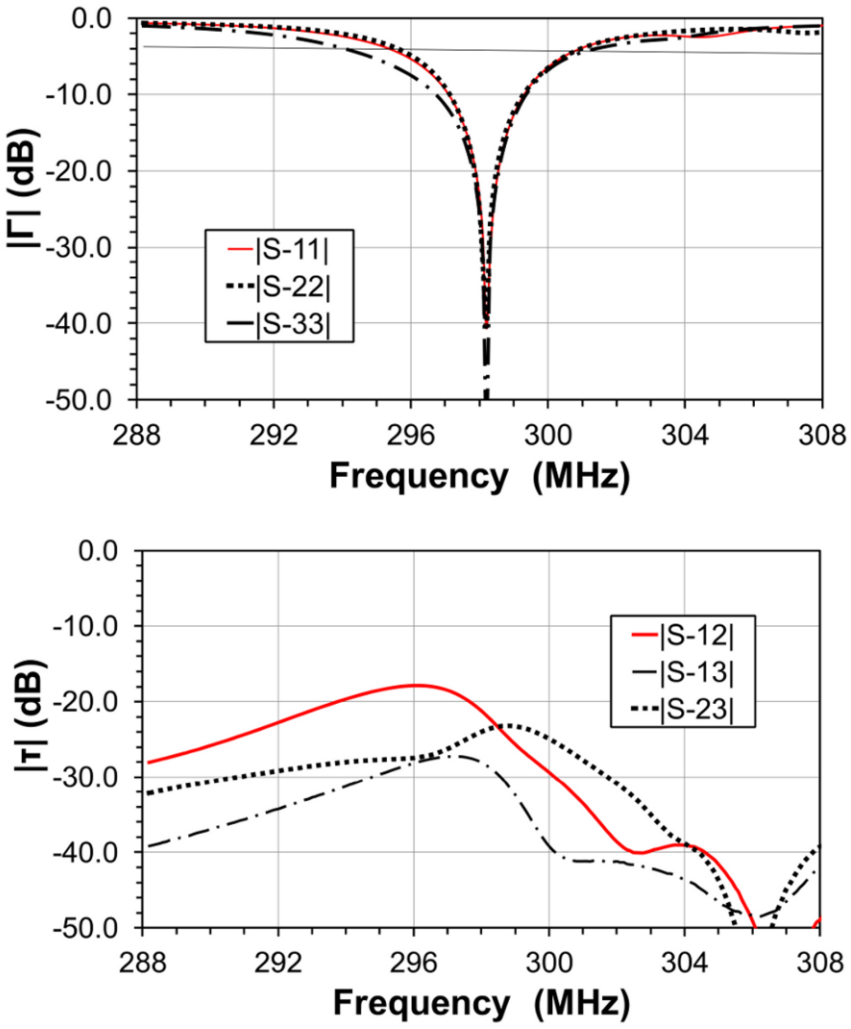


**Figure 32: Computed s-parameters for magnetic wall proof-of-principle from equivalent circuit model**

## Full-Wave Filter Simulation

The simulation setup corresponding to the *in situ* decoupling analysis of the full-wave filter analysis is presented in Fig. 30a. Fig. 35a demonstrates the relative magnetic field profile of two coupled-coils individually tuned and matched for proton imaging at 7 T (corresponding to 298.2 MHz). In comparison to the same RF coils in Fig. 35b, the electromagnetic coupling between the coils is demonstratively suppressed with the placement of MWs between the three coils. The RF magnetic field around both coils is shown in the xy-plane along the centre line, when a voltage drives the middle coil (Coil 2) and the other coils (Coil 1 and Coil 3) are terminated with 50 Ω. Due to the presence of the

MW, minimal current is induced in Coil 1 and Coil 3. Consequently, the flux linkage between coils is reduced. Reflection ($|S_{11}|$) and transmission ($|S_{12}|$) coefficients provided in Fig. 33 for the same setup quantifies the degree of isolation achieved between the terminals of the RF coils. For the simulation, the MW achieved -24 dB of decoupling at the Larmor frequency (298.2 MHz) between both Coil 1 - Coil 2 and Coil 2 - Coil 3, as well as -28 dB of decoupling between Coil 1 - Coil 3. Defining -20 dB as the stopband roll-off, the MW achieved a bandwidth of 40 MHz about Larmor frequency.

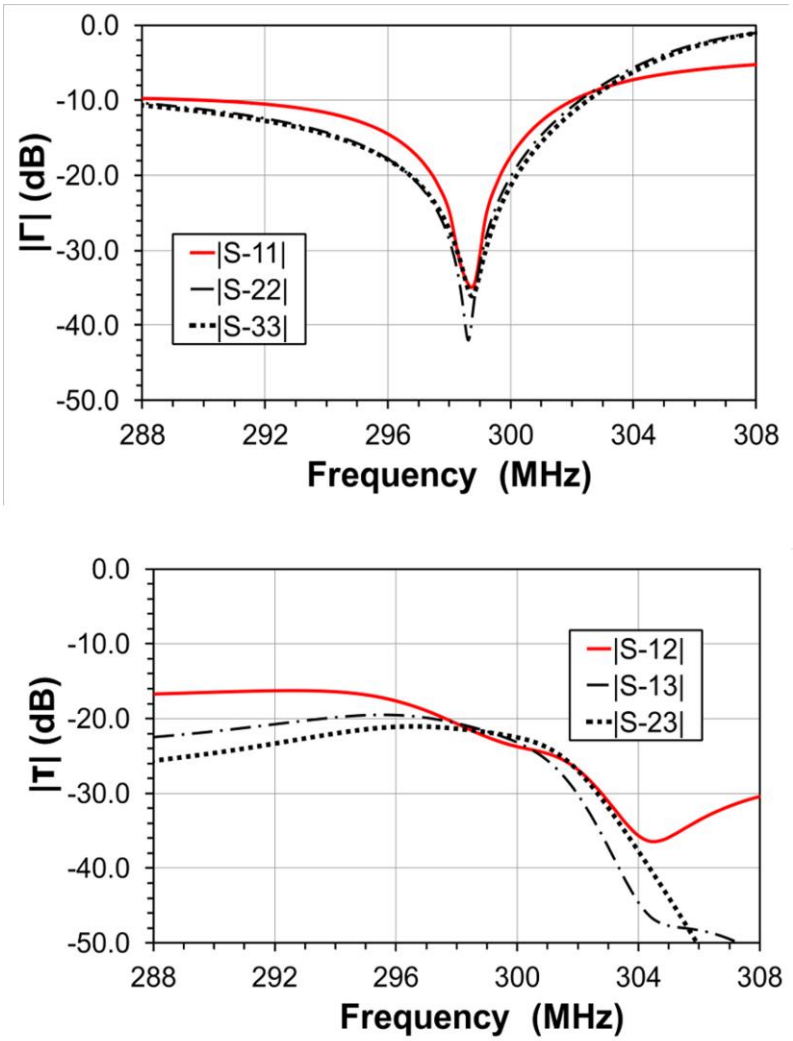


**Figure 33: Simulated s-parameters for the magnetic wall proof-of-principle**

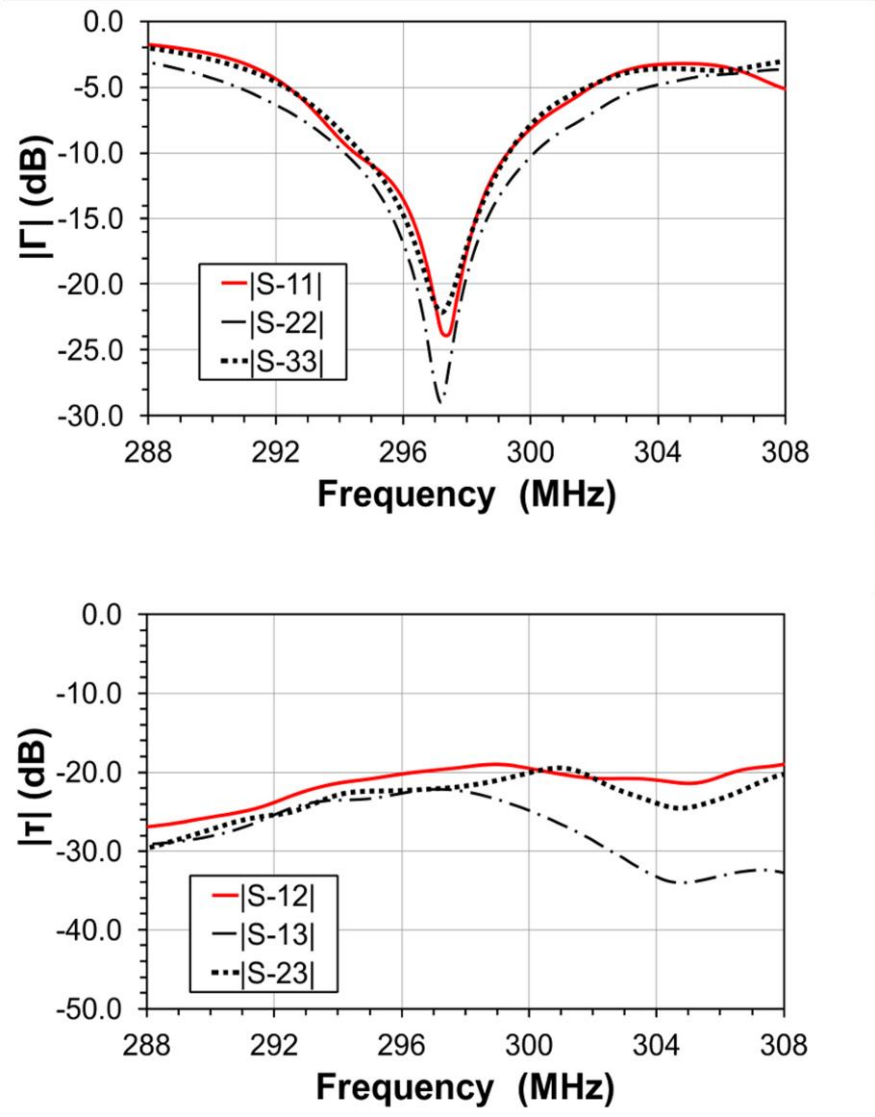


**Figure 34: Measured s-parameters for the magnetic wall proof-of-principle**

As seen in Fig. 36, the computed magnetic field (|**H**|) contours located in the centre of the stopband excitation demonstrate a sharp geometric roll off in intensity along both the x- and z-axes. This may in part be accounted for due to the quasi-toroidal MW geometry present in the y-direction. This results in a relatively continuous field that is produced along the y-direction where the individual coils retain a high coupling coefficient ($k \approx 1$). Additionally, this geometry enables the MW to be highly sensitive to a perpendicular **H**-field incidence without significant magnetic interaction between the individual spiral

inductors themselves on a unit cell to unit cell basis. This is demonstrated in Fig. 36, with minimal flux linkage visible between adjacent conductor windings. Due to this, the coupling between MW unit cells is predominately electric as illustrated by Table III.

The dissipative power losses occurring inside both the MW filter and a decoupling capacitor are provided in Table II. The losses were calculated at 277 MHz, 298.2 MHz, and 338 MHz to provide details on losses incurred in both the passband and stopband of the MW filter. The most pertinent losses are those occurring at 298.2 MHz, as these contribute to the maximum attainable efficiency of a transmitting RF coil.

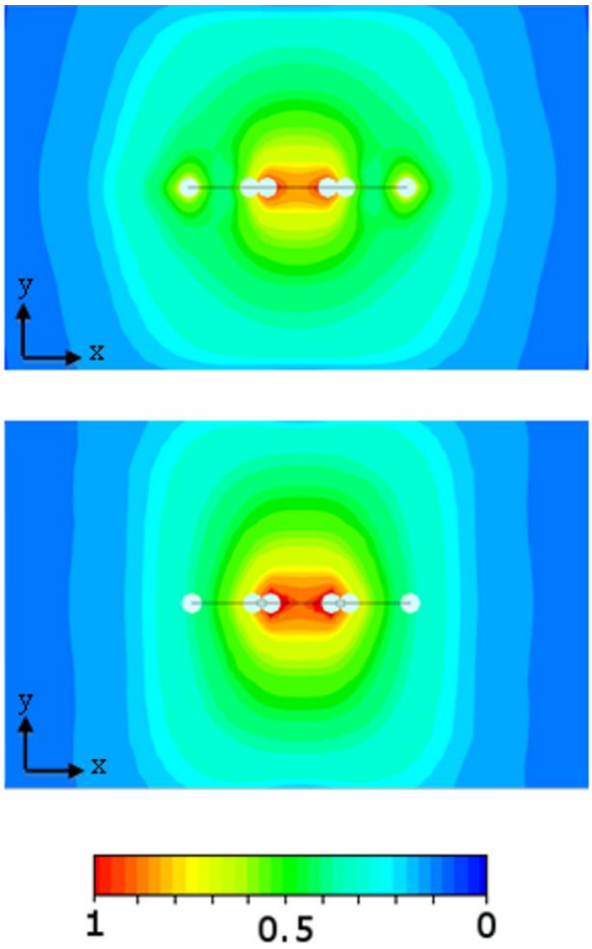


**Figure 35: Relative magnetic field |H| contours for (a) coupled and (b) decoupled RF elements**

## Experimental Results

The experimentally measured S-parameters of decoupling three RF coils with a MW filter are provided in Fig. 34. Placement of the MW filter between the coils effectively decoupled all coils in the array. At 298.2 MHz, $|S_{12}|$ was -19 dB, and both $|S_{13}|$ and $|S_{23}|$ were -22 dB with no mode splitting present in either $|S_{11}|$, $|S_{22}|$ or $|S_{33}|$ spectra.

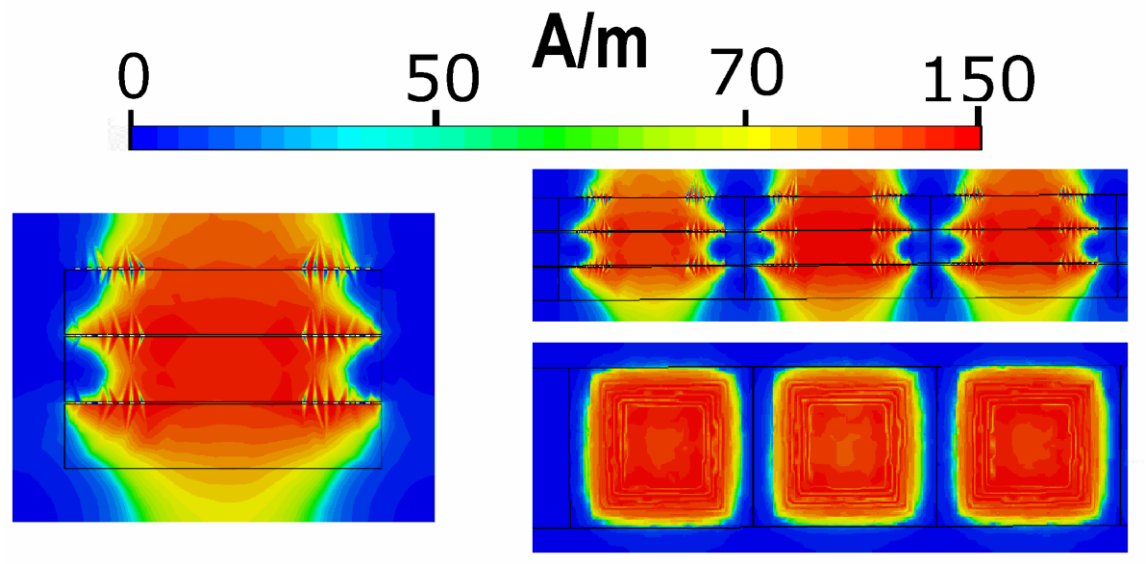


**Figure 36: Relative magnetic field (|H|) contours for a plane-wave excitation of the magnetic wall**

## Discussion

The analysis presented here yields similar filtering behavior to that previously studied [43]. Both in the case of reference [39] and the MW filter, the stopband was centered about the resonant frequency of the periodic filter. Based upon the equivalent network presented in Fig. 27, the calculated *s*-parameters (Fig. 32) were similar to those derived from both the full-wave simulation (Fig. 33) and experiment (Fig. 34). Therefore, through the use of a filter that is edge-coupled to adjacent RF elements, the MW achieves an adequate bandwidth for eliminating transmission between coils.

The 'spiral inductor' or 'spiral resonator' design basis for the filter has been previously demonstrated to operate effectively in the MHz regime [44]. One possible

reason for this is the large inductance achievable with such a design. The relatively large inductance is required to resonate the MW at 298.2 MHz, as highly capacitive structures at these dimensions are difficult to realize. However, the possibility still exists for further miniaturization and optimization for better decoupling with different distributed coil designs. As demonstrated in Fig. 36, when MW unit cells are located in a periodic array it is possible to orient the spiral inductor such that it produces relatively minimal stray magnetic field lines and the coupling can be modulated thusly for either component of the electromagnetic field in an RF array. These field patterns in Fig. 36 also demonstrate the modular decoupling capability of the MW. The MW's ability to minimize fringe field effects and reduce the RF penetration length has the potential for modular application as a bandstop filter placed between many closely interacting transmit coils.

## Design Principles

Several key principles have been demonstrated in this study for the purposes of decoupling closely interacting RF array elements. Several strategies can be used for obtaining the optimal distributed filter design: equivalent circuit calculation, full-wave optimization or a combination of both.

For the equivalent circuit calculation, as seen in (3.4), the transmission between any two RF coils located in an array can be modulated by the coupling coefficients between individual MW unit cells, as well as between the unit cells and the RF coils. Although, in this study the MW unit cell was synthesized based upon the most compact design achievable with the PCB manufacturing tolerances, other geometries can be exploited with finer manufacturing processes. Due to this, (3.4) can be solved such that in (3.10b) $S_{12} \approx 0$ with the following steps: (1) Determine a suitable unit cell geometry with a self-resonance at the Larmor frequency which the RF array is tuned to; (2) Calculate the self impedance of the RF coils and MW unit cells; (3) Calculate coupling coefficients from (3.13) or (3.14) for coupling between RF array coils as well as between each RF array coil and a single MW unit cell; (4) Optimize for required unit cell-to-unit cell coupling. The optimization process for obtaining coupling values in coupled resonant filters can be obtained from a gradient-based optimization [45-47].

In terms of full-wave decoupling optimization, as was performed in this study, the coupling coefficients, although possible to extract after-the-fact, need not be directly calculated. Due to this, the simulation space can be setup to generate a parameter search for the best geometric parameters given some initial steps: (1) Determine a suitable unit cell geometry (single spiral, stacked spiral, concentric open loop rings, etc.) with a self-resonance near the Larmor frequency which the RF array is tuned to; (2) Construct the unit cell inside simulation space and assign geometric variables (for example, from Fig. 28: 'L', 's', 'w', and 't') to the conductor/dielectric dimensions as outlined in the Methods section for determining the resonance of a single unit cell; (3) Array unit cells into full MW and place inside RF array inside the simulation environment; (4) Perform parameter sweep for the same, or a subset of the geometric variables, as outlined in step (3) with the conditions of $\min\{S_{i,j}(\omega_O)\}$ and $\min\{S_{i,i}(\omega_O)\}$. It may be required to include parametric variables for the tune and match lumped elements located on the RF coils to ensure a proper decoupling solution is reached.

**Table IV: Simulated power dissipation in magnetic wall proof-of-principle**

| | **Dissipated Power [dB]** | | | $\|S_{12}\|^2$ |
|---|---|---|---|---|
| | 277 MHz | 298.2 MHz | 338 MHz | 298.2 MHz |
| MW | -42.3 | -35.3 | -40.9 | 0.004 |
| Capacitor | -41.1 | -34.3 | -39.7 | 0.050 |
| Inductor | -40.8 | -34.0 | -39.4 | 0.045 |
| Overlap | | | | 0.071 |

With either approach to the design of a specific MW, the number of unit cells, and their relative placement in the RF array modulate the coupling matrix and electromagnetic fields that ultimately cause coupling and cross-coupling between RF coils in an array. This allows

other potential conductor unit cell geometries to be used that better conform to the RF array requirements and also invites different placement strategies of MW unit cells to further optimize the decoupling effect. With both the equivalent circuit and full-wave analysis including the effects of electric and magnetic coupling, the MW presents an interesting response to the presence of mixed coupling in a full RF array. The high level of decoupling obtained with this method exemplifies that coupling contributions from both components of the electromagnetic field are filtered. Applying this decoupling mechanism is unlike most conventional on-coil MRI RF decoupling techniques (lumped elements, overlap, etc.), which typically only evaluate first-order coupling from the magnetic or electric field components. Furthermore, the distributed design has the ability to minimize transmission within a bandwidth that is modulated by the coupling coefficients between the individual MW unit cells as well as between the unit cells and the RF elements themselves. Therefore, unlike individual lumped elements between adjacent RF coils or geometric overlap, the MW coupling matrix can be synthesized to suppress all cross-coupling terms.

S-parameters from the full-wave analysis are presented in Fig. 33. For an unloaded transmit system, -30 dB of decoupling achieved between transmit coils is considered very high. This simulation data had comparable $|S_{12}|$ values to those measured from experiment (Fig. 34). Furthermore, when comparing the relative magnetic field intensities of the coupled (Fig. 35a) and uncoupled (Fig. 35b) magnetic field intensities, the MW provides a distinct suppression in the magnetic flux linkage between RF coils. Thus, the MW filter is effective in reducing the potentially damaging power scattered through the coupled coils in the array and back towards the amplifiers.

The computed dissipative power losses demonstrate that the MW filter retains a high Q-factor ($\approx 30$) and a low magnetic loss component due to the geometry and materials used for constructing the filter. Because of this, the filter dissipated only 0.1 dB more power at the Larmor frequency than the conventional decoupling capacitor and 0.4 dB more power than a decoupling inductor. Therefore, decoupling with a MW filter does not introduce any significant losses into the transmit system at the transmission frequency of 298.2 MHz and the losses that are introduced are likely compensated for by the improved inter-coil decoupling.

## Production and Application

The PCB manufacturing of fine conductor features is not ideal for translating simulation and analytic design to the physical realization. The etching or milling process may lead to irregularities in the conductor edges and surface roughness — two properties well known to change the electromagnetic response at high frequency [48, 49]. However, within a certain bandwidth of frequencies centered about the Larmor frequency, the slight perturbations in resonance between periodic structures resulted in a MW that is still sufficient for decoupling (inter-coil $|S_{12}|$) beyond the -20 dB limit (Fig. 34). The manufacturing tolerances also might account for the variation in the simulated results to those achieved in experiment. The use of a tabulated surface impedance model for the conductor inside the EM computation may be useful for simulating this reality.

This study has primarily focused on the lumped inductance and capacitance present in the conductor windings of a MW to derive resonance and subsequent filtering response. The permittivity of the substrate the conductor is printed atop has not been explored, but it is expected that altering the substrate will alter the Q-value of the MW filter as well as the bandwidth response. Furthermore, the presence of an additional dielectric layer atop the conductor has the potential to mitigate the selective MW response to certain magnetic field (**H**) angles of incidence [50]. This is a potential method for altering the coupling of the MW into the array without manipulating the specific placement or geometry of the MW unit cell. Due to the fact that eliminating transmission between transmit coils occurs due to the filtering capabilities of a MW, trade-offs between loss-tangent (magnetic losses) of the dielectric substrate and total amount of conductor present (resistive losses) in a MW still could be optimized. Minimizing the amount of lossy material placed adjacent to a transmit coil would be beneficial for designing highly efficient transmit coils.

In comparison to established techniques for decoupling transmit arrays, the design and fabrication process for implementing magnetic walls requires some further effort. However, the use of parametric models in EM simulation or an equivalent network can drastically reduce the optimization time required to realize the desired bandstop features required for magnetic wall decoupling. Furthermore, once a MW unit cell is designed for a given frequency and coil geometry, the same design can be potentially applied to a

plurality of similar coils by varying the coupling coefficients between MW unit cells or MW unit cells and RF coils which can be achieved by altering the number and spacing of the unit cells located inside the MW. This applicability provides a potential method for manufacturing transmit arrays of larger channel-counts and varying geometries best optimized to increase the overall homogeneity of the transmission profile at ultra-high field.

## Comparisons

Typically, a conventional on-coil method for passively decoupling RF coils is a function of the tuning and load present in the RF coils themselves; however, the filtering behaviour of the MW is derived solely from the geometry of the design. As demonstrated in this study, by tuning a MW to the resonance of an array of RF coils the production of a stopband between the terminals of each coil port in the array is possible. Therefore, the MW need not be retuned for any specific change in the loading condition the RF array is subject to. This is in part due to the relatively small penetration of the RF field produced by currents induced in the MW, as illustrated in Fig. 36. Furthermore, as seen in Fig. 31, a 15-MHz FWHM for the filter allowed for modest flexibility in small perturbations in the loading and tuning conditions subject to the RF coils.

The conductor placement of the MW is compact and below a length that has the potential for direct interaction with the RF array load (object to be imaged). This is demonstrated in Table IV where next-nearest adjacent RF coil coupling to the MW unit cell is 10-fold lower than nearest RF coil coupling to an adjacent MW unit cell. More specifically, dual row geometries or highly conformal designs could potentially see the benefits of using such a modular design that utilizes the coupling coefficients to account for extraneous interaction between additional components and the decoupling elements themselves.

The MW method is equally applicable to MRI receive arrays, although in this case, excellent methods for decoupling already exist using preamplifier impedance mismatching. These methods do not translate to transmit coils because all commercial RF amplifiers used in MRI have 50-Ω impedances and transmit chains. As such, it may be more applicable to transceive arrays, wherein the same coils are used for transmit and receive.

# Conclusions

This study confirms the applicability of the ‘magnetic wall’ decoupling concept for multi-channel RF arrays used in MRI. This study provides equivalent circuit analysis, full-wave simulation and physical measurements that demonstrate high decoupling values between adjacent coils, as well as the design principles for achieving this decoupling. Further work can be performed to evaluate whether the MW method can be exploited for different RF coil geometries and higher-channel count arrays.

The novel method uses an FSS-inspired design tuned to a Larmor frequency that is well below the GHz region where FSSs are typically used. It is also the first study to use planar RF filtering techniques for MRI RF decoupling. The MW approach provides exciting opportunities to acquire images with highly decoupled RF channels at potentially high efficiency.

# Chapter 4

# Design and Decoupling of a Parallel-Transmit Head-Coil at 7T with Magnetic Wall Distributed Filters

In this chapter, the decoupling method developed in Chapter 3, based on our decoupling framework from Chapter 2 is applied to the construction of an 8-channel parallel transmit head coil design for neuroimaging at 7 T. This section is derived from the manuscript, "Design and Decoupling of a Parallel Transmit Head Coil at 7 T with Magnetic Wall Distributed Filters" published in IEEE Transactions on Medical Imaging on April 2015.

## Introduction

In this manuscript, a new approach is applied to the construction of a MRI transmit coil based upon our earlier demonstration of magnetic walls (MW) in Chapter 3 and reference [9]]. The MW is a distributed element filter with a periodic structure. In the previous chapter, it was demonstrated that when a MW was edge-coupled to adjacent resonating RF elements, suitable for imaging at 7T, the bandstop filtering characteristics of the MW achieved significant decoupling between elements. Herein, this manuscript adopts the same design as previously presented and describes the use of the MW in a full transmit array suitable for routine imaging.

For MRI, Wiltshire et al. [51] were the first to demonstrate the use of a similar technique by exploiting the properties of a "Swiss Roll" to design a magnetic flux guide for RF transmission. While flux transmission over a 200-mm distance was shown in their paper, it was estimated that optimum SNR would only be possible if the flux guide could be fabricated such that the on-resonance losses (both resistive and dielectric) occurring along the length of the Swiss roll could be reduced by an order of magnitude [52]. To date few studies have examined the use of similar methods for MRI [52-55].

In this work, we apply a distributed RF filter and generate a specific MW design to decouple MRI RF coil elements in a full array. The MWs were created with thin, lightweight MR-compatible substrates that are narrow in relation to the width of the neighbouring elements and the wavelength of operation. Magnetic walls were implemented

using conventional printed circuit board (PCB) technology, making them simple and economical to design and produce.

This manuscript presents the construction and characterization of a practical multi-element transmit coil that employs MWs as the decoupling mechanism. The performance of the transmit coil is evaluated in terms of inter-element coupling, transmit uniformity, transmit efficiency, power deposition, and SAR. The parallel transmit coil is paired with a 31-channel receive coil and demonstrated to be suitable for imaging the human brain at 7 T.

# Methods

## Magnetic Wall Design

The MW design was based on the distributed filter presented in [9]]. To achieve a compact, self-resonant structure, the MW design utilizes conductive, tightly wound spiral traces embedded in a host dielectric strip. The single spiral trace, embedded in the dielectric, is referred to as a spiral resonator (Fig. 37). A 'unit-cell' was defined as a stack of three spiral resonators.

Design of the MW is based upon resonating the individual MW unit cells at the Larmor frequency of the transmit elements that are to be decoupled. The modified impedance of a network, stated in equations (3.1) to (3.6), is used to derive the magnetic wall design for the 8-channel transmit array.

As elucidated in Chapter 3, by tuning the individual MW unit cells to the identical frequency to that of the transmit elements, transmission between individually driven transmit elements is modulated by the coupling terms in (3.5c). This was demonstrated in [9]], where the synthesis of the appropriate coupling coefficients between the MW unit cells and transmit elements, as well as between individual MW unit cells resulted in satisfying (3.9b) for a -20 dB attenuation between individual transmit elements. By tuning all MW unit cells to the same resonant frequency, not only is the manufacturing process simplified, but the optimization of decoupling with MW is formulated in terms of (3.5b) which can be calculated from either full-wave simulation or analytic expressions ([25]).

The MW was a linear array of 27 unit cells with identical dimensions, two stacks of which are shown in Fig. 37. The pertinent dimensions for decoupling the 7-T head coil with this MW design are provided in the caption of Fig. 37.

From full-wave simulation, it was found that when three identical 1D array strips were stacked on top of each other, the stopband of the MW was centered about 298.2 MHz. Simulated $|S_{11}|$ and $|S_{12}|$ parameters, based on the optimized design, are presented in Fig. 38 for an incident TEM mode.

For use in the 10-channel transmit array, the MWs were manufactured using conventional PCB technology (Advanced Circuits, Aurora, Colorado). Twenty-seven copper spiral traces (Fig. 37) were inlaid on a Rogers 4350B substrate (relative permittivity: 3.48, loss tangent: 0.0031) in a 1D array (259 × 7.6 × 1.6 mm). Due to manufacturing tolerances, the individual unit cells located in the delivered MW were resonant at 304 MHz. This shifted the overall stopband of the MW. However, due to the fact that the individuals coupling between the RF coils and the MW unit cells, as well as between the unit cells themselves remained constant, the constructed MW was still able to decouple adjacent coils effectively. This characteristic decoupling of two adjacent coils via the MW is presented in the measured data in Fig. 38.

## Transmit Coil

A 10-channel transmit coil and 31-channel receive coil were combined in a transmit-only/receive-only (TORO) architecture. The mechanical former of the transmit coil was designed to fit as tightly as possible around the conformal receive coil (Fig. 39) (minor and major axes: 24 cm and 26.5 cm, respectively), with a 1-cm radial gap between the transmit and receive coils. The transmit coil consisted of a circumferential array of 10 rectangular loops (‘elements’), of which nine elements were 22.2 cm long. To determine an appropriate width for the nine elements mounted on the transmit former, the Q-ratios (the ratio of unloaded to loaded Q) of isolated elements of varying width were measured. A 5.6-cm-wide element in isolation resulted in a Q-ratio of 4.0 and allowed for the positioning of nine transmit elements (5.6 × 22.2 cm with 6.35-mm-wide struts) about the circumference of the former, spanning a 71.3-cm arc length. The MWs were symmetrically

placed between each element in the 7.9-mm inter-element gaps (Fig. 39) and rigidly mounted at both ends. Elements were milled out of 36-μm-thick copper adhered to 0.79-mm-thick garolite. The corners of each element were filleted to a 3.2-mm radius to reduce radiation losses and dielectric coupling to the sample. Periodic breaks in the elements' conductors were introduced for the distribution of capacitors to reduce dielectric coupling to the sample. Six surface-mount capacitors (100 series: American Technical Ceramics, NY) were incorporated into each element with values ranging from 2.2 – 4 pF. Variable capacitors (1 – 30 pF, Johanson Manufacturing, NJ) were placed at the drive point and opposite thereof to allow for *in situ* tuning and matching. Each of the nine elements were elevated 2.4 mm above the former using milled nylon shims of identical dimensions to those of the transmit elements. These shims aligned the copper trace of each loop element with the middle layer of the adjacent MWs. This placement was chosen to align the loop elements to the surface of the MW as demonstrated in [9]] as well as to keep consistency between full-wave simulation results, bench top measurements and in-vivo experiments.

An opening was incorporated into the anterior portion of the former, with an adjustable mirror, to allow for the presentation of visual stimuli using both front and rear projection. To avoid a reduction in transmit field in the frontal lobe, a tenth transmit element (14 × 13 cm) was incorporated onto the former of the receive coil and connected to the transmit coil using SMA connectors after transmit and receive coils were locked together. This anterior-most element was composed of 1.3-mm-diameter conductive wire with four 1 – 4 pF surface-mount capacitors and two variable 1 – 30 pF capacitors distributed along the wire length.

Active detuning was incorporated into each element using two detuning boards located symmetrically in the central axial plane of the element (see Fig. 39). The detuning boards consisted of a parallel LC circuit and PIN diode (Microsemi, HUM2020) that was DC biased via twisted pairs of 30-AWG insulated wire. At the DC input of the detuning board, two RF chokes (1-μH inductors with self-resonance frequency near 300 MHz) and a single surface mount bypass capacitor (100 series: American Technical Ceramics, NY) isolated the incoming bypass signal from noise. The 30-AWG insulated wires were routed along the virtual ground of the coil. Multiple RF chokes were incorporated into each DC

line. The PIN diode of the detuning board was forward-biased during signal reception, resulting in a high-impedance circuit and 20 – 28 dB difference in sensitivity between tuned and detuned states. Coaxial cables were affixed to shielded 298.2-MHz choke baluns located at the input port of each element. Choke baluns eliminated common-mode currents on coaxial shields during RF transmission and created a balanced input to each element. Coaxial cables were routed as far away from the elements as possible, and additional RF and DC chokes were inserted as needed. All elements were matched to 50 Ω utilizing the parallel-to-series capacitance-ratio method [35].

Each transmit element was tuned and matched with the MWs in place between the elements, with all other transmit elements open-circuited, and with the whole coil in an appropriately loaded and shielded condition. This method was chosen as the inclusion of MWs into the array increases the total system inductance and thusly would shift resonance if placed into the array after the fact. Therefore, in order to not have this occur, the individual elements were tuned and matched with all MW present. Once individually tuned and matched, all the elements were then made resonant. Sufficient isolation was achieved without any further modification. Final adjustment of the tune and match of each element was completed inside the scanner when loaded with a head. The MWs were designed with a slot at each end to allow each array strip to slide linearly with respect to the others, allowing for minute perturbations of the resonant behaviour by varying the inductive coupling between layers. This was required by the two elements located on either side of the former's anterior opening, due to the asymmetry caused by the anterior-most transmit element (embedded in the receive former).

## Receive Coil

A 31-channel receive coil was built on a conformal former that was mechanically fastened to the inside of the transmit coil (Fig. 39). The layout of the receive coil was designed after the 'soccer ball' geometry introduced by Wiggins et al. [56]. Coil elements were constructed with 16-AWG copper wires with five or six capacitor breaks. The elements were noise-matched to 75 Ω, with λ/2 coaxial cables (approximately 33 cm) running from the coil input to low-input-impedance preamplifiers (Siemens Healthcare,

Erlangen, Germany) located directly behind the receive coil and outside of the transmit field. The source impedance of 75 Ω (real) was pre-determined by manufacturer's specifications for optimal source matching. Two lattice baluns were placed along the λ/2 cable to reduce common-mode currents. Active detuning and preamplifier decoupling circuits were located on the preamplifier matching boards.

## MRI System

All MR data collection was performed using a human neuro-dedicated 7-T MRI system (Agilent, Yarnton, UK). The system was equipped with an AC84 head gradient coil and Quantum gradient amplifiers (Siemens, Erlangen, Germany) with a 36-cm-diameter clear bore. The scanner was controlled by a Tx/Rx Direct Drive console (Agilent, Walnut Creek, CA) with independent RF waveform, amplitude and phase control for each of the 16 small-signal transmit-waveform cards. Each transmit-card signal was amplified using one of 16 power modules available with the two 8-channel broadband amplifiers on the system (7T1000M-8C, Communication Power Corporation, Hauppauge, NY). One kilowatt of peak power was available per channel at the amplifier, reduced to ~500W at the distant coil ports. The front-end consisted of 32 independent receive chains, of which 31 were used as dictated by the geometry of the receive coil. Preamplifiers were located directly behind the receive coil (Fig. 39).

Forward and reflected power was monitored during all scans using a calibrated (at the coil port) RF power monitor built in-house. To ensure the most conservative estimate of global SAR, all forward power was assumed absorbed by the subject (i.e., reflected power was not subtracted). Furthermore, the local-to-global SAR ratio was computed inside a voxel tissue model with full-wave electromagnetic simulation software (CST Microwave Studio, Darmstadt, Germany).

All human subjects signed a written form of consent in accordance with the procedures of the Human Subjects Research Ethics Board at The University of Western Ontario.

## Bench-top Measurements

All s-parameters, MW frequency response, and coupling frequencies were measured with a network analyzer (Agilent Technologies, model E5071C). S-parameters of the transmit coil elements were measured with the receive coil nested inside and detuned. The coil system was loaded with two concentric, axially aligned gel phantoms (14.6 cm in diameter and 8.6 cm in height, each), located approximately 2 cm radially away from the transmit elements. The gel phantoms were composed of gadolinium chloride, agarose, and sodium chloride, in concentrations intended to mimic the human head [57].

S-parameter measurements were recorded inside a copper RF shield that replicated the RF shield lining the interior surface of the gradient coil. The 50-Ω match was robust with respect to small subject movements. Similarly, the $S_{12}$ between any two adjacent elements of the receive coil was measured at the preamplifier ports. A circular transceive loop (1.5-cm diameter) with a broadband balun (CX2074, Pulse Electronics) input was used for MW characterization.

Loaded and unloaded Q ($Q_L$ and $Q_U$, respectively) measurements of the transmit coil were acquired with a standard double-probe technique at the isocentre of each element. Q-values were measured with all transmit elements resonating and the receive coil biased to a detuned state. To quantify the effect of the MW decoupling on coil efficiency, Q-ratios were measured as a function of frequency for incremental tunings of the single element in isolation, with and without MWs present. Q-ratios of this isolated element were discretely measured without a coaxial cable or balun attached to the element. All loaded Q measurements were acquired with the head-mimicking phantom described above. The preamplifier decoupling, active detuning, and Q-ratio of a single isolated receive coil (without the preamplifier or coaxial cable attached) was measured using a conventional double-probe technique.

## Transmit Efficiency

The protocol for measuring power efficiency was performed on a human subject. Prior to performing power calibrations, the static field ($B_0$) was shimmed using RASTAMAP [58]. A STEAM power calibration was then performed in the centre of the

brain (voxel size: 3.0 x 3.0 x 3.0 $cm^3$; BW: 34 kHz) to find the power requirement to achieve a 90º pulse in the subject's brain with a 6000-µs square pulse. A factory calibrated power meter (Anritsu ML2437A) was then used to verify the required power at the input of each coil. The accuracy of the power meter (±5%) was also verified using a modulated signal with known power from an external signal generator. The total RF power was calculated by summing the individual powers measured at the input of each transmit element.

In addition to the use of Q-measurements to characterize transmit efficiency, the effect of the MWs on transmit efficiency was also quantified by measuring the efficiency of a single element from the MW coil in isolation (using a STEAM power calibration over the entire sensitive volume of the coil) with and without the presence of a MW on each side of the transmit element.

## Transmit Uniformity

Prior to $B_1^+$ shimming, the static field ($B_0$) was shimmed using RASTAMAP [58]. A low flip-angle 3D gradient-recalled-echo volume was acquired for each transmit channel, according to the methods presented by Van de Moortele et al. [59], to produce relative $B_1^+$ maps (matrix size: 96 x 96 x 64; FOV: 25.6 x 25.6 x 25.6 $cm^3$; TE/TR: 3.3/8.3 ms; BW: 34 kHz; flip angle: 3º). The actual flip angle imaging (AFI) approach was then performed to calibrate the $B_1^+$ maps using the procedures presented by Yarnykh [60] and augmented with the RF and gradient spoiling schemes developed by Nehrke [61] (matrix size: 96 x 96 x 64; FOV: 25.6 x 25.6 x 25.6 $cm^3$; TE/TR1/TR2: 3.3/20/100 ms; BW: 34 kHz; flip angle: 70º).

The required transmit amplitudes and phases for $B_1^+$ shimming were calculated for a shim solution over a single axial slice and over the whole brain using a Gaussian least-means-squared algorithm [62]. This method determines a shim solution that balances transmit uniformity with efficiency. Transmit field uniformity was calculated by dividing the standard deviation of the flip angle by the mean flip angle over the volume of interest (a deviation of 0% being perfectly uniform). To demonstrate the effectiveness of the MW decoupling scheme on isolating individual $B_1^+$ profiles, AFI maps were also acquired using

just two adjacent MW-decoupled elements. One element at a time was open-circuited and AFI maps were acquired. The effect of the MWs on the spatial distribution of a single element's $B_1^+$ profile was also evaluated by acquiring an AFI map of a phantom with and without MWs present.

## Specific Absorption Rate

A full-wave EM simulation of the 10-channel transmit coil was performed using CST. The CST model was designed with the same geometry and material parameters as the actual coil. As shown in Fig. 40, a tissue voxel model ('Gustav' of the 'voxel family') was positioned inside the transmit coil in accordance with the geometry inside the Agilent 7-T scanner. Each element was constructed with six 5.2-pF capacitors and two variable capacitors located inside the circuit schematic. All capacitors were modeled with an equivalent series resistance (ESR) of 0.1 Ω. The variable tune and match capacitors were parameterized outside the simulation space to allow for co-simulation tuning and matching. With magnetic walls placed between each coil element, all elements were tuned to 298.2 MHz and matched to 50 Ω. The full-wave simulation included electric boundary conditions on all six planes of the simulation box. All boundaries were located at a distance of 30 cm away from the nearest in-plane coil feature. The vacant space between coil and boundaries had a relative permittivity and permeability values equal to '1'.

Each coil element port in the simulation was driven in turn, resulting in individual transmit profiles for each element. Once tuned and matched, the worst-case power deposition field was calculated via incrementing the input voltage phases on all 10 transmit channels. The |E| field inside the voxel model was then computed, until a maximum value was found. From the resulting excitation pattern and power deposition, SAR was calculated across the voxel model based on the specific tissue parameters. This allowed for 10-g peak and global SAR to be calculated across the voxel model. The local-to-global SAR fraction was calculated by dividing the peak 10-g local SAR by global SAR. The 10-g averaging SAR calculation was performed in accordance to the IEEE C95.3 standards.

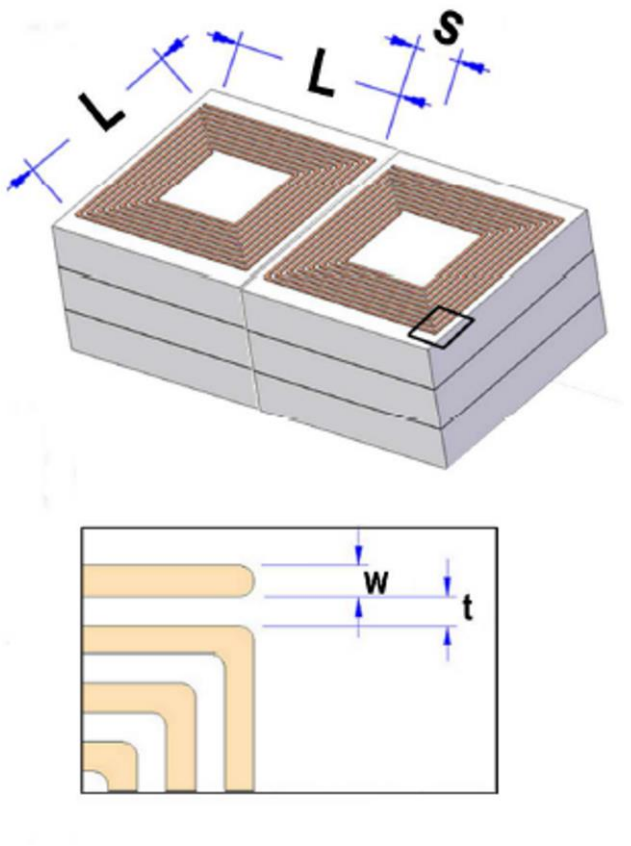


**Figure 37: Magnetic wall dimensions for 8-channel transmit array**

## Results

For all measurements, the uncertainty is quoted as one standard deviation based upon the individual measurements contributing to the mean.

### Magnetic Wall Characteristics

A single spiral-resonator unit cell had a calculated inductance of 24.3 nH and a calculated lumped capacitance of 0.25 nF. For this spiral trace, the conductive and dielectric resistances were 0.08 Ω and 36 MΩ, respectively. Due to the PCB manufacturing tolerances (from Fig. 37, the spiral trace thickness ‘w’ and spacing ‘t’ were particularly susceptible to variation), the constructed 27 adjoining unit-cell stacks comprising the MW individually resonated at 304 MHz (≈ 6 MHz above the Larmor frequency). However, due to the fact that the coupling between MW unit cells and the RF coils is determined by larger and less sensitive conductor geometry (from Fig. 37, MW spacing between RF coils ‘L’

and unit cell-to-unit cell spacing ‘s’), the constructed MW still formed a bandstop filter capable of decoupling coupled transmit elements – see Fig. 39 for MW placement between two actual transmit-coil elements.

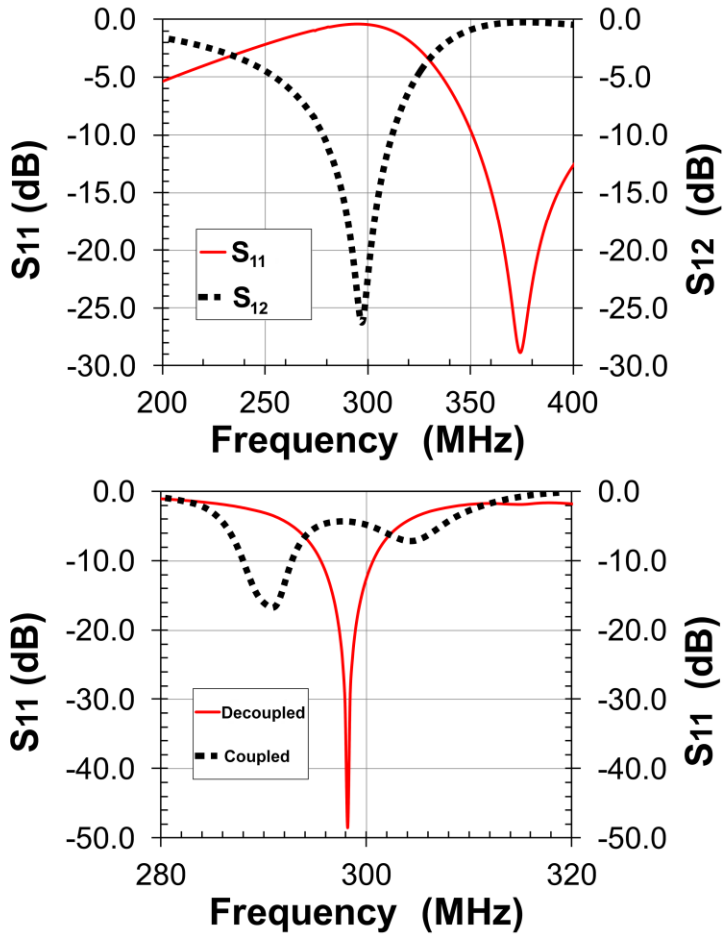


**Figure 38: Simulated s-parameters of the magnetic wall under plane-wave excitation (top) and adjacent RF elements coupled and decoupled (bottom).**

Each coil element was tuned with the MWs in place, while the others were open-circuited. Without a MW present, a pair of resonant elements demonstrated clear coupling, resulting in $S_{11}$ peak splitting about the Larmor frequency (Fig. 38 – dotted line, bottom). With a MW placed between the coupled pair, the $S_{11}$ spectrum displayed a single resonance at 298.2 MHz (Fig. 38 – solid line, bottom). As mentioned in the Methods section, the inclusion of a MW between coil elements increases the overall system inductance. Due to this, the $S_{11}$ spectrum for each transmit element was restored to a single frequency mode

with the placement of a MW between each element; however, this frequency peak was shifted below the Larmor frequency by approximately 7 MHz. To avoid the complications of retuning this shift after the fact, tuning and matching of each coil element in turn was performed with all the MWs in place and all other elements open-circuited. This process was also used for the measurements reported in Fig. 38.

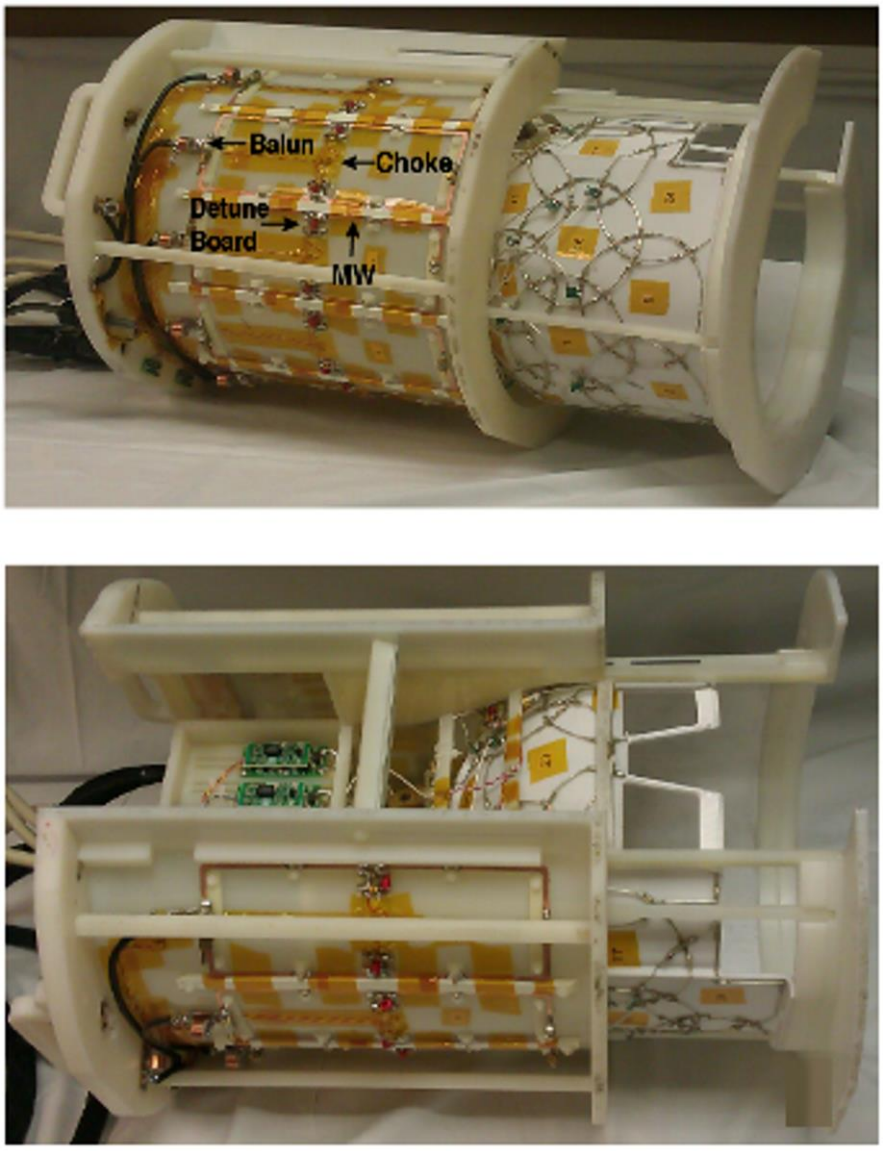


**Figure 39: Physical construction of 8-channel transmit/32-channel receive RF coil.**

## Receive Coil

The mean $|S_{12}|$ between adjacent elements was -19 dB. Typical values for preamplifier decoupling and active detuning were -20 dB and -33 dB, respectively. A typical Q-ratio of a receive element in isolation was 7.8 ($Q_u/Q_L$: 250/32).

## Transmit Coil Decoupling

Adjacent elements had a maximum (worst case) and mean $|S_{12}|$ value of -18 dB and -22 ± 5 dB, respectively. Next-nearest neighbors had a minimum and mean isolation of -24 dB and -33 ± 9 dB, respectively. The mean $|S_{12}|$ value across the full S-parameter matrix was -28 ± 8 dB. A full S-parameter matrix is available in Fig. 41. Peak splitting about the Larmor frequency was eliminated in all $S_{11}$ spectra and coil elements achieved a mean $|S_{11}|$ value of -38 ± 11 dB.

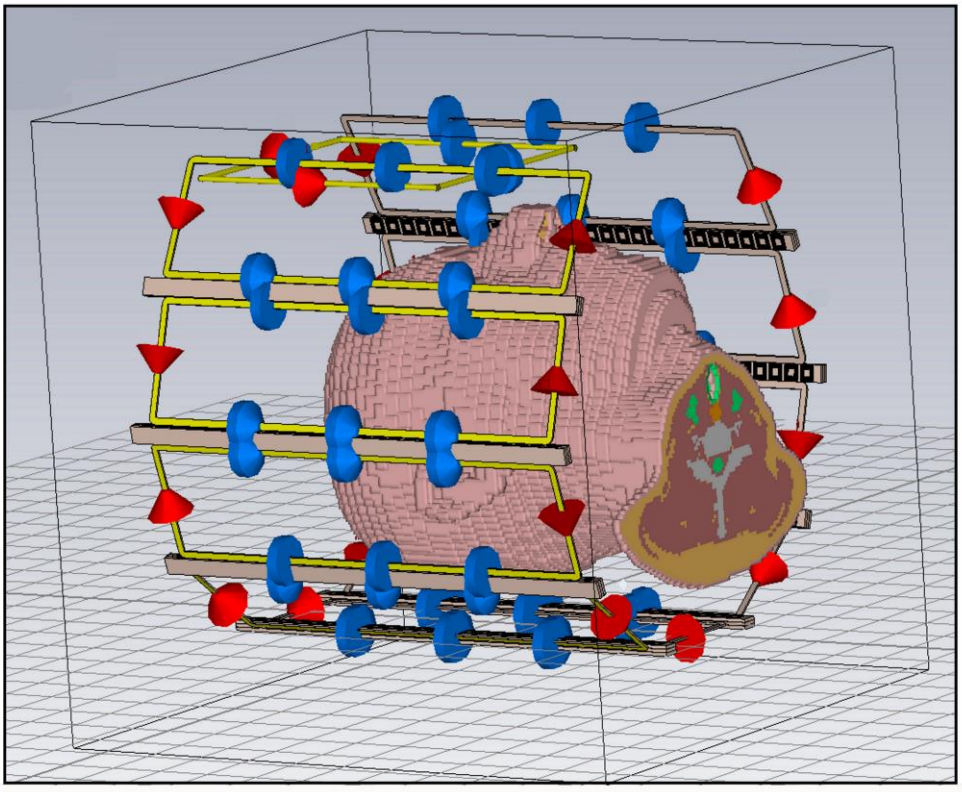

**Figure 40: Electromagnetic simulation setup for SAR calculation in CST Microwave Studio.**

## Transmit Coil Efficiency and Uniformity

A single transmit element in isolation had a Q-ratio of 4.0 ($Q_U/Q_L$: 135/34) without magnetic walls present. When magnetic walls were placed on either side of the element, the Q-ratio decreased to 3.4 ($Q_U/Q_L$: 129/38) at the Larmor frequency. Thus, the presence of the MWs yielded a 15% decrease in the Q-ratio. Consistent with this, the measured transmit efficiency of a single element in isolation decreased by 16% (0.63 dB) after MWs were placed on either side of the element. Additionally, the 15 MHz resonant bandwidth of the MW was consistent with the measured Q-ratio drop when placed adjacent to a transmitting element. With identical experimental setups, the only source of additional resistance in the transmit coil were the MW. Therefore, the decrease in power efficiency is a ratio of the total system resistance with and without the MW – which is measured via the Q-ratio. Unlike the larger coil diameters utilized in this study, the coils presented in Chapter 3 were significantly more coil-noise dominated. Hence, the increase in resistive loss due to the inclusion of the MWs was a smaller proportion of the measured Q-ratios. The normalized Q-ratio as a function of frequency is provided in Fig. 42. In the completed coil, the unloaded Q values ranged from 92 – 104, and the loaded Q values ranged from 48 – 56. This corresponded to Q-ratios for the nine elements located on the transmit former ranging between 2.0 and 2.2. The tenth transmit element located on the receive former had a Q-ratio of 1.6.

The 10-channel MW coil measured 32.2 W of peak forward RF power to achieve a 90º pulse in the brain with a 6000-µs square pulse. Fig. 43 demonstrates the $B_1^+$ profile of a single element, with and without MWs present on both sides and tuned and matched in both cases. The MWs showed minimal effect on the spatial distribution of the $B_1^+$ profile. Figure 44 shows the $B_1^+$ profiles of individual elements in a two-channel transmit array when decoupled with a MW and when operated with one or the other element open-circuited. The array when decoupled with a MW is presented in the top-half of Fig. 44. The array with no MW and either element open-circuited is displayed in bottom-half of Fig. 44.

The excitation pattern of each coil in the decoupled array showed only minor variation from the same element operating in isolation.

The transmit field uniformity across the entire head is demonstrated with flip-angle maps in Fig. 45. The transmit field uniformity over the axial, sagittal, and coronal planes of the whole-brain shim solution was 17%, 10%, and 11%, respectively. The transmit field uniformity over the whole-brain volume (to the posterior-most extent of the cerebellum) was 24%.

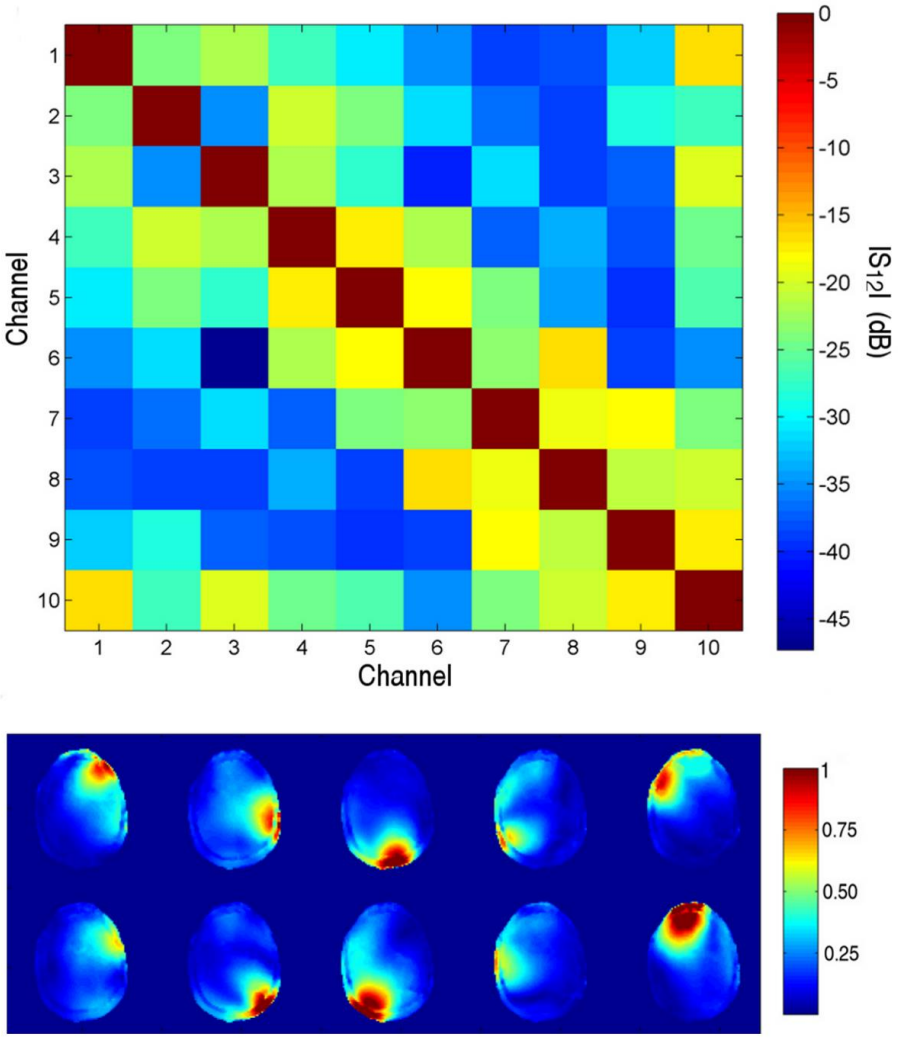


**Figure 41: (top) Measured s-parameters for the 8-channel transmit array and (bottom) relative transmit maps on a per channel basis**

## Specific Absorption Rate

The local-to-global SAR ratio was calculated to be 7 with no significant SAR hot spots located within or directly beneath the MWs. The 10g local SAR value was calculated to be 3.74 W/kg. Representative sagittal and axial slices of power deposition across the simulated head are presented in Fig. 46a. The intensity in each color map presented in Fig. 46 was scaled according to the 3D maximum occurring inside the entire voxel model. Observation of the magnified MWs (4:1 scale) in Fig. 46 (top) display no more significant power deposition occurring inside the MWs in comparison to the axial slice of the simulated head. In Fig. 46 (top), the magnified MWs in the axial slice correspond to the translucent MWs as viewed in the sagittal slice. SAR contours corresponding to the power deposition profiles in Fig. 46 (top) are presented in Fig. 46 (bottom-left) and Fig. 46 (bottom-right) for the sagittal and axial slices, respectively.

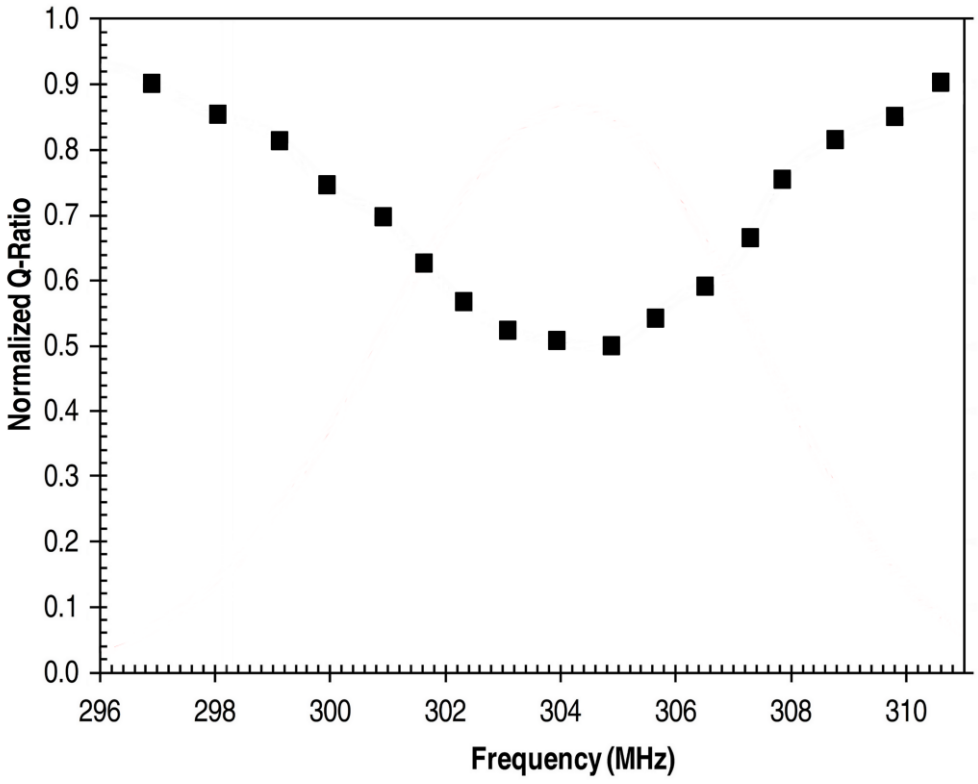


**Figure 42: Measured relative Q-ratios for a signal transmit element placed adjacent to a magnetic wall**

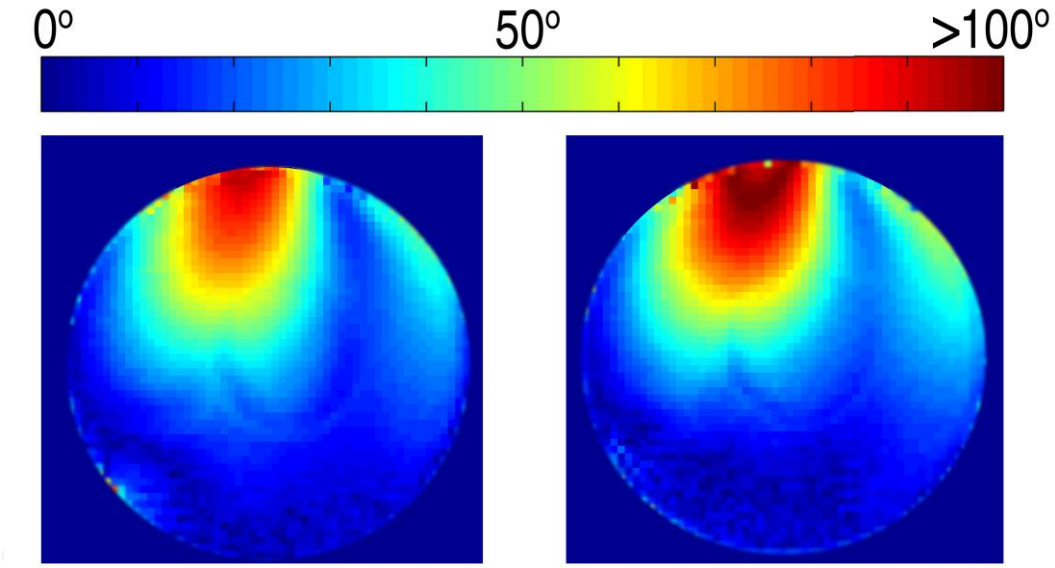


**Figure 43: Actual Flip-angle Imaging (AFI) performed with one transmit element. (Left) with one element in isolation and (Right) with a magnetic wall placed adjacent to the element**

## Discussion

The vertical placement of the coil element will change the symmetric geometry of the transmit array and thus alter the coupling coefficient between the MW and the transmit element. This corresponds to a '$m_{i,j}$' coupling coefficient between the MW and transmit element in (3.5c). The modulation of this coupling affects the ability of the MW to minimize transmission about the system's resonant frequency [9]]. Since the anterior-most element required a vertical offset from the former, the optimal isolation was not achieved with this element. However, for the remaining nine channels, adjacent elements had a mean $|S_{12}|$ value of -23 ± 5 dB. The high decoupling between next-nearest neighbors (-33 ± 9 dB) is a major benefit to this decoupling scheme. As a consequence, the coupled RF power between elements was reduced. The achieved mean $S_{12}$ value between next-nearest neighbors in the MW coil is on the order of what low-input-impedance preamplifier decoupling can provide in receive coils (the current gold-standard for decoupling). Furthermore, the efficacy of MW decoupling of next-nearest neighbors and beyond invites the application of the MW to unconventional transmit array geometries, as the method is not limited by prescribed geometry or parasitic elements; however, the performance of

MW's in denser transmit arrays of higher channel count still remains to be verified.

## Transmit Uniformity and Efficiency

There was a 15% reduction in the normalized Q-ratio (Fig. 42) with MWs present, consistent with the observed 16% decrease in transmit efficiency. It can be deduced that the loss mechanism in the MW is due in part to resistive and dielectric losses, as well as resonant absorption. However, by reducing coupling between coil elements the power losses between elements is reduced. Furthermore, the potential for destructive interference between $B_1^+$ fields of coupled elements is lessened. These two benefits appear to outweigh the loss mechanism in the MW.

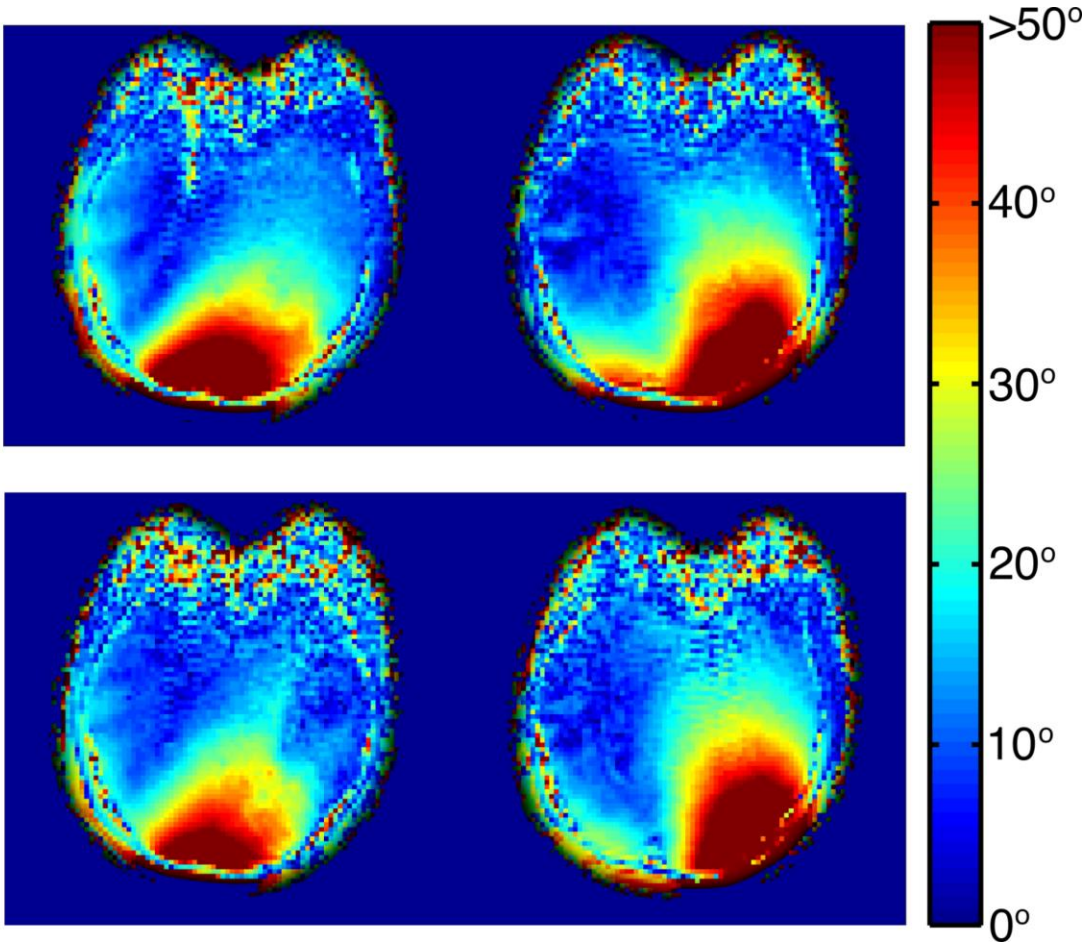


**Figure 44: Actual Flip-angle Imaging (AFI) performed with two transmit elements. (Top) With one element open-circuited and (Bottom) with a magnetic wall decoupling the elements**

Due to the small MW dimensions, only 7.9 mm of separation was required between elements. This construction prevents voids in RF intensity between adjacent elements that cannot be compensated by RF shimming. With RF shimming, the deviation in flip angle was 24% across the whole brain, with a moderate reduction in flip angle in the inferior aspect of the brain (i.e., the cerebellum), as noted in Fig. 45. Uniformity can be further improved with tailored 3D RF excitation and multi-row geometries. A demonstration of image quality and coverage produced by this coil is presented in Fig. 47 for an accelerated anatomic imaging sequence.

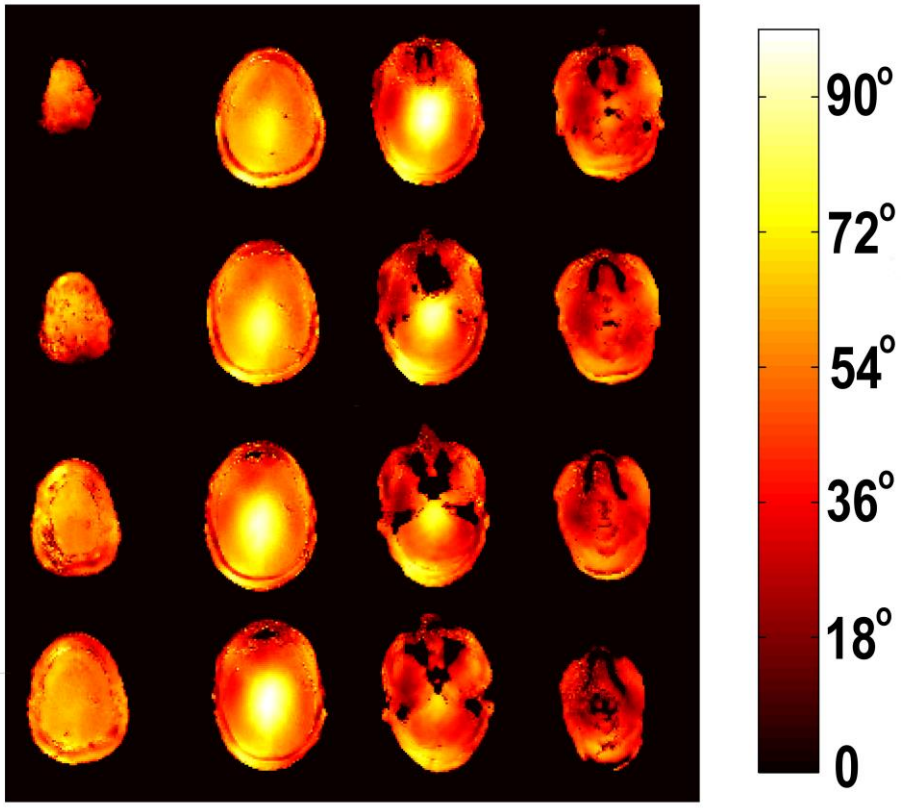


**Figure 45: Transmission uniformity maps constructed with a Magnitude-Least-Squares (MLS) shimming solution applied**

## Specific Absorption Rate

In Fig. 44, the minimal effect a MW has on the $B_1^+$ distribution of an individual transmit element is presented. Only a small deviation in flip angle can be discerned between the two $B_1^+$ profiles. Therefore, the gross interaction a MW has with the electric field

distribution is expected to be similarly minimal. To this end, the maximum power deposition inside the MWs during a full-wave simulation was 10 dB lower than the maximum power deposition inside the simulated head (Fig. 46-top); therefore, MW conductor heating possibly leading to mechanical failure during an MRI scan is not of particular concern. Furthermore, the intensity of SAR hot spots do not show any direct correlation to MW placement in the array and appear to be dominated by tissue parameters (i.e., by comparing the power in Fig. 46-top with SAR in Fig. 46-bottom). The maximum local 10-g SAR was located near the isocentre of the cerebral cortex, with other hot spots located near the frontal sinuses and at the posterior of the head near the occipital bone.

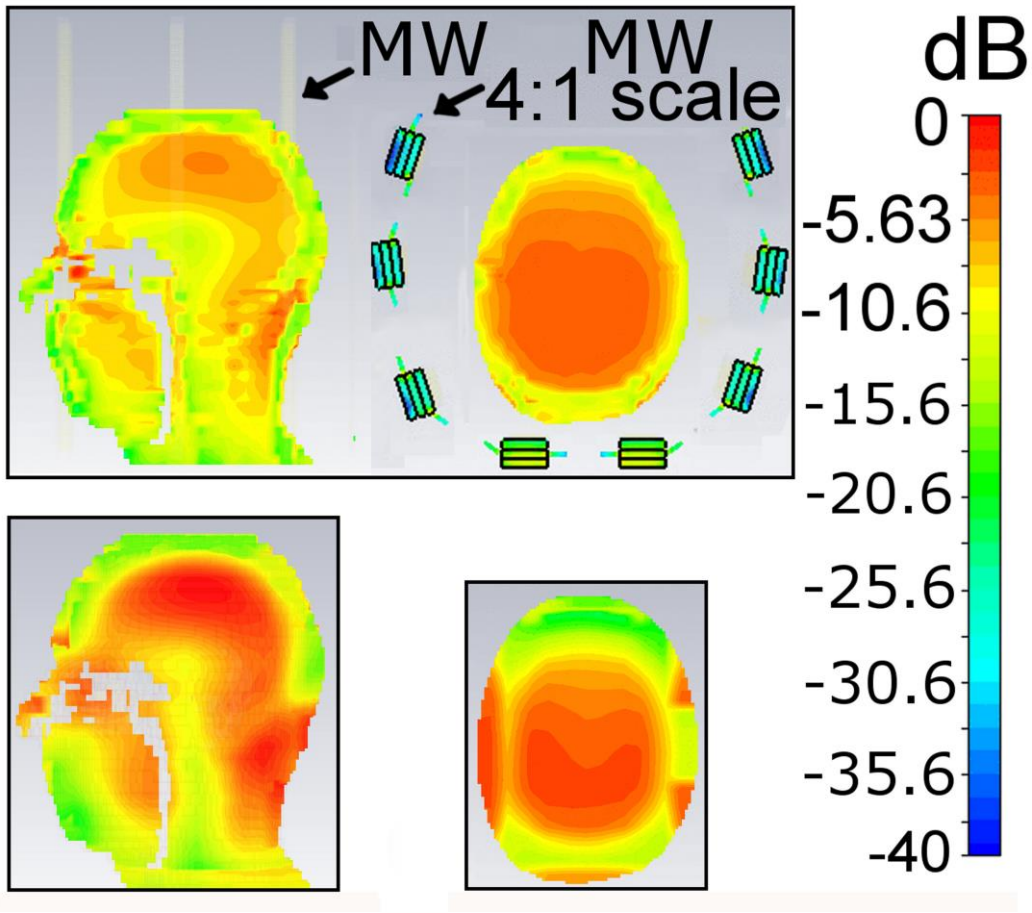


**Figure 46: Simulated SAR distribution**

Previous studies based on full-wave simulations with multi-channel transmit coils operating at 7 T have demonstrated similar SAR distributions to those shown in Fig. 46-bottom. An 8-channel head coil operating at 7 T, studied in [63], reported comparable SAR

distributions across the human head. The simulations performed in the aforesaid study were experimentally verified on a tissue-mimicking phantom. Reference [64] examined the maximum SAR potential of surface coils operating at 7 T. A 28.7-W/kg local maximum was recorded for a 3.2-W/kg SAR average across the head. This is a similar local-to-global SAR ratio of 7 derived from the MW coil.

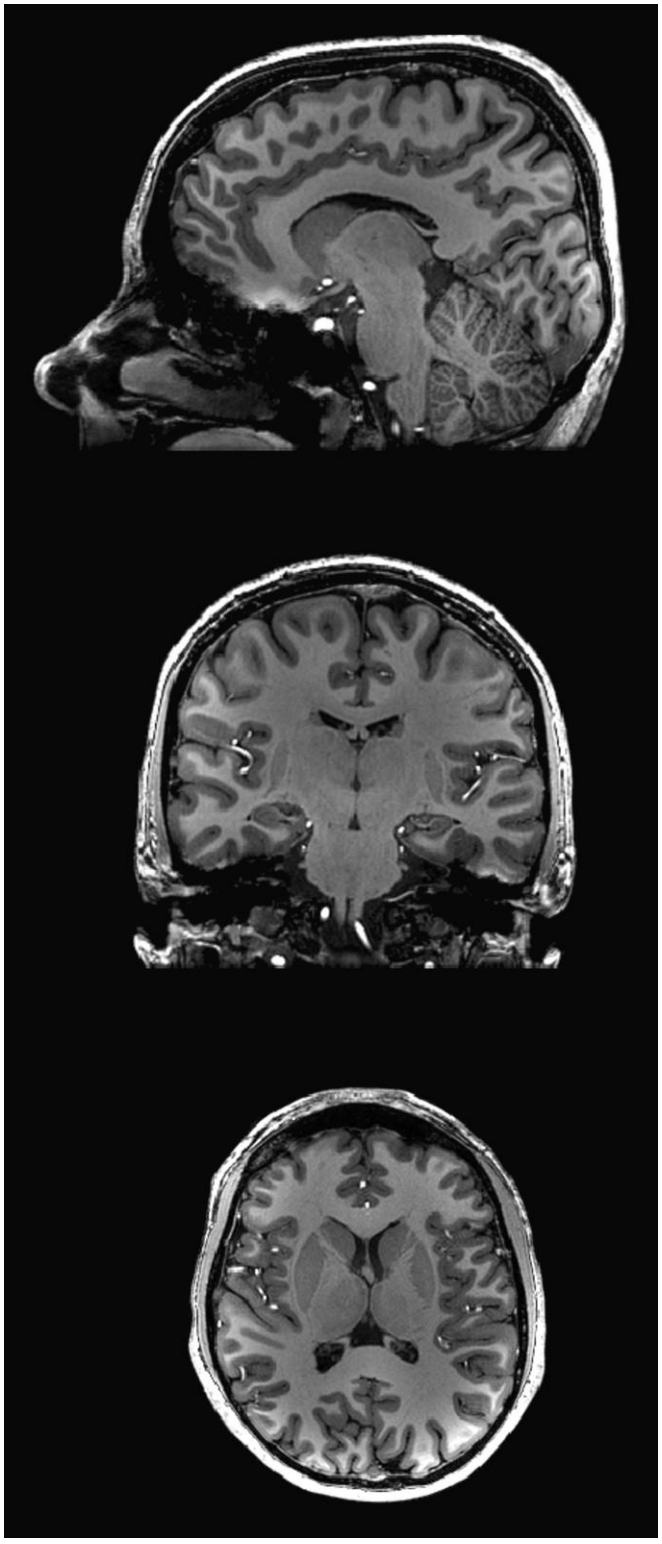

**Figure 47: Sagittal, coronal, and axial slices of a 3D MPRAGE image. Matrix size: 250 x 366 x 286; FOV: 150 mm x 220 mm x 172 mm; TE/TR 2.8/8.1 ms; TR 5500 ms; BW 63 kHz; flip angle: 11-deg; total acceleration: 3.57; scan time: 6 min 12 s.**

## Magnetic Walls

Conventional PCB dielectric layers provide modest flexibility of the wall during the design and manufacturing process. In a linear array of transmit elements, as discussed in this manuscript, the rigidity allows for reproducible and predictable construction; however, in terms of producing two-dimensional coils, decoupling along a curved surface is required. By printing the MW on a flexible dielectric this easily extends the decoupling mechanism to larger arrays with decoupling on a curved surface. Since the local flux lines will curve with the transmit elements, the MW approach is expected to provide good decoupling over non-cylindrical geometries permitting the coupling coefficients in equation (3.5c) can be achieved between the MW and the RF elements. The ability to print the MW in-plane with transmit elements provides the ability to fully-design and manufacture an innately decoupled array prior to populating the PCB with lumped elements. Fully printed arrays provide the benefits of a controlled PCB manufacturing process including the incorporation of low-loss dielectrics and controlled-layer impedance.

It has been previously demonstrated that patch antennas can be routinely decoupled with MW-like structures [65]. This area of application would be of particular interest to travelling wave excitation studies for performing excitation from a combination of synthesized waveguide modes.

# Conclusion

This study establishes the practicality of using a magnetic wall for decoupling multi-channel transmit array coils. The MW decoupling technique is capable of efficiently decoupling nearest neighbor and next-nearest (and further) neighbors to a level comparable to that achieved by receive-only coils using low-input-impedance preamplifiers.

The decoupling scheme uses a distributed RF filter tuned to the Larmor frequency, with a bandstop that encompasses the coupled modes of a multi-element coil. This allows for high decoupling between elements, leading to efficient transmission. The decoupling capabilities of MWs have significant benefits in the design and construction of multi-element transmit coils. Current PCB manufacturing techniques can inlay conductive traces on flexible dielectric substrates, may extend the decoupling mechanism to larger arrays

with decoupling on a curved surface. Thus the MW approach is expected to find practical applications for transmit or transmit/receive arrays at high fields.

## Acknowledgements

RM and MAK would like to acknowledge early discussions with Prof. Omar Ramahi at the University of Waterloo that drew our attention to the use of split-ring resonators for decoupling patch antennas [37].

# Chapter 5

# Conformal Electric Dipole Array

The general coupling/decoupling theory developed in Chapter 2 was verified with a proof-of-principle design for both a lumped-element and distributed filter designs. Following this, the distributed design was further analyzed in Chapter 3 then experimentally verified on a 10-channel transmit array in Chapter 4. This section now analyzes the application of lumped-element decoupling method in more detail than originally provided in Chapter 2. This section provides a treatment for the lumped-element decoupling of a transceiver dipole array in much the sample way Chapter 3 and Chapter 4 analyzed the distributed design. As described in the introduction, the decoupling of complex array topologies is a difficult task. Here, we demonstrate the applicability of our approach for tackling one such array design. Furthermore, this section demonstrates the ability of our decoupling approach to alleviate design constraints that allow an array optimization to selectively minimize SAR while maintaining $B_1^+$ efficiency and homogeneity. The content of this chapter is derived from the manuscript, "Electric Dipole Array Shape Optimization for 7 Tesla Neuroimaging" under revision for Magnetic Resonance in Medicine.

## Introduction

Multi-channel radio-frequency (RF) arrays, composed of multiple resonating elements, are a critical component in magnetic resonance imaging (MRI) acquisition. Parallel transmit (pTx) arrays provide individual sensitivity profiles that when used in concert with optimized gradient and RF waveforms can accelerate the traversal of excitation k-space [89,90]. This principle can be used to accelerate multidimensional selective excitation [91,92], perform $B_1^+$ or RF shimming to overcome inhomogeneity at ultra-high field (UHF) [93-96], or reduce specific absorption rate (SAR) [97,98]. Similarly, parallel receive (pRx) arrays exploit the locally high signal-to-noise ratio (SNR) of surface coils to the MRI signal ($B_1^-$) and extend it across a full field-of-view [12] while simultaneously performing spatial encoding, utilized in accelerated imaging [99-101].

The magnetic fields responsible for exciting spins during RF transmission, as well as receiving signal from the transverse magnetization post-excitation, transition from purely reactive near-field interaction towards a mixture of both near- and far-fields as the main magnetic field strength increases [102]. Due to this, electric dipole antennas are finding increasing utility at UHF when compared to more conventional RF loop elements [103,104] and combinations of dissimilar array elements into a single RF coil construction are expected to show similar performance gains: $B_1^+$ efficiency per unit SAR [105] and SNR [106].

Realizing the potential benefits of densely populated dipole arrays for head imaging requires several technical challenges to be addressed:

(i) Mutual coupling;

(ii) Reduction of dipole footprint for clinical RF-coil dimensions; and

(iii) Impedance matching in the presence of increased electric field interactions.

Following from (i), the magnitude of coupling between dipole elements in a densely populated receive array can significantly enhance noise correlations and degrade measured SNR, regardless of an increased sensitivity to the sample [107]. In terms of (ii), to achieve a resonant length in the proximity of tissue the dipole must be electrically shortened. The final technical challenge (iii) arises due to the electromagnetic field patterns produced by dipole elements. Once placed in proximity to a lossy dielectric, the dipole demonstrates strong sensitivity to the relative permittivity of the conducting medium.

In this study, (i) is addressed with a method for eliminating mutual coupling based on several unique properties of the dipole element in an RF array. Technical challenge (ii) is resolved with a shape-optimization procedure. The design method utilizes an iterative optimization to solve for dipole conductor paths, when projected onto a forming structure, achieve self-resonance, target field homogeneity and passive SAR reduction. Finally, it is demonstrated that the final technical challenge in (iii) is alleviated by the shape-optimization performed in (ii) that produces a more uniform, broadband input impedance, that can be transformed to 50-Ohm across a larger bandwidth via low-pass ‘L’ matching networks.

The decoupling and impedance matching methods presented in this study are applied to a transciever array designed with a new shape-optimization method. The RF array is composed of conformal, meandered dipole antennas, array elements that are not easily decoupled by current approaches. Circuit diagrams and a simplified overview of the methods are provided to aid in future constructions of other UHF arrays adapted for various applications. The conformal dipole geometry was constructed to minimize an aggregation of transmission and receive performance metrics into a single cost function. These metrics included: 10-g SAR minimization, $B_1^+$ uniformity and efficiency, for transmission and $B_1^-$ coverage and mean intensity maximization, for reception.

# Theory

## Input Impedance

The input impedance and mutual coupling of tissue-loaded dipoles have a direct impact on the imaging performance of dipole arrays. Therefore, an equivalent circuit for a dipole in a lossy-conducting medium from [108] is adopted for illustrating the effect of mutual coupling and impedance matching an electric dipole for 7 T head imaging. In this particular case, the dipoles are oriented along the z-axis and the electromagnetic properties of the human brain were considered.

As demonstrated in Fig. 48a, a dipole adjacent to a lossy dielectric will experience a reduction in the input resistance. Approximating the input reactance as straight lines near-resonance (see highlighted portion in Fig. 48a), the slope of the input reactance near-resonance is measurably increased for the tissue-loaded case (increase from $\sim 0.66\,\Omega/\mathrm{MHz}$ to $\sim 2.3\,\Omega/\mathrm{MHz}$). This load-sensitivity is due to the electrical interaction between the dipole and the sample, rather than the conventional inductive loading experienced by loop-based RF elements (109). If impedance matched with a ‘L-section’ network, the tissue-loaded dipole will exhibit a very narrow ‘Q’ due to the decreased input resistance and thus have a narrow matching bandwidth. However, due to the increased electrical sensitivity to the load, as demonstrated by the increased slope of the input reactance (Fig. 48a), deviations in the dipole loading will result in impedance match fluctuations when compared to the free-space equivalent. This poses a potential problem for routine imaging with dipole

elements, as different head sizes and/or placement of the human head in the RF coil will affect the final loading an RF array experiences.

This technical challenge is not unique to dipole elements. However, unlike the common RF 'loop' that is predominately inductively loaded [110] with the relative permeability remaining constant across non-magnetic human tissue, the dipole's strong electrical coupling to the sample scales by the much larger deviations in relative permittivity of the medium. Matching dipole elements for the MRI electromagnetic environment implies that a more sophisticated network may be required, or more accurate determination of the loaded impedances across a variety of subjects.

## Mutual Coupling

In the presence of tissue, both mutual resistance and mutual reactance increase (see Fig. 48b). When the dipole is moved from free-space to the tissue-loaded case, the on-resonance mutual reactance presented in Fig. 48b deviates from a predominately inductive coupling to capacitive coupling. For the tissue-loaded dipole, this increase in the capacitive coupling occurs before- and on-resonance (297.2 MHz). Approximately 5 MHz above resonance, the coupling becomes inductive. In comparison, the dipole located in free-space demonstrates purely inductive coupling for the same frequency band.

The concept of mutual coupling presented in Fig. 48 can be extended for multiple elements in an array. As seen in Fig. 49a, coupling between three adjacent elements, '$Z_m$', is present between all elements in the RF array, with the respective magnitude of interaction mediated by the array geometry. As computed in Fig. 48b, the reactive component of '$Z_m$' arises due to magnetic flux linkage and parasitic capacitance between elements. Similarly, resistive interactions between the sample and adjacent elements can be modelled with an equivalent resistor that links elements with an electrical connection (see Fig. 49a).

Methods for eliminating interactions between elements typically require either: (a) a method to modify the radiation patterns either utilized during transmission and/or reception such that individual elements maintain orthogonal sensitivity profiles in space (i.e. loop overlap), or (b) the addition of one or more reactive elements to compensate for

mutual impedance (-*j*X, as seen in Fig. 49a). As complexity of the RF array increases with channel count and asymmetric radiation patterns, a general decoupling method for eliminating all resistive and reactive coupling terms between elements, such as the method proposed in Fig. 49b with '-$Z_m$', is ideal.

Applying the decoupling method presented in Fig. 49b for the case of two tissue-loaded dipoles (Fig. 48b), results in the following matrix equation:

$$Z_{system} = \begin{bmatrix} Z_D & 0 & Z_m \\ 0 & Z_{decoupling} & 0 \\ Z_m & 0 & Z_D \end{bmatrix} \tag{5.1}$$

The solution for the self-impedance of the decoupling section designed to provide the compensating -$Z_m$ term from (5.1):

$$Z_{decoupling} = \frac{Z_D + Z_m}{Z_D^2 + Z_D Z_m} \tag{5.2}$$

where $Z_D$ is the self-impedance of the tissue-loaded dipoles, $Z_m$ is the mutual impedance between dipoles prior to decoupling, and $Z_{decoupling}$ is the self-impedance of the decoupling section inserted in Fig. 49b that eliminates $Z_m$ with a $-Z_m$. The magnitude of $Z_{decoupling}$ is plotted in Fig. 49c.

The self-impedance $Z_{decoupling}$ is characteristic of a series-resonator circuit, or a ladder filter with prescribed poles. This is a direct consequence of the mutual coupling presented in Fig. 48b, whereby both inductive and capacitive coupling are present near-resonance for tissue-loaded dipoles. Therefore, to achieve a circuit that presents $-Z_m$ between the terminals of the dipoles, a resonant circuit or ladder filter is required. In the case of Fig. 48b, for two loaded dipoles it would appear one resonator tuned on- or near-resonance is required (1$^{st}$-order filter), but the extension to Fig. 49b of multiply coupled dipoles requires more sophisticated matrix decomposition methods for an undetermined filter order.

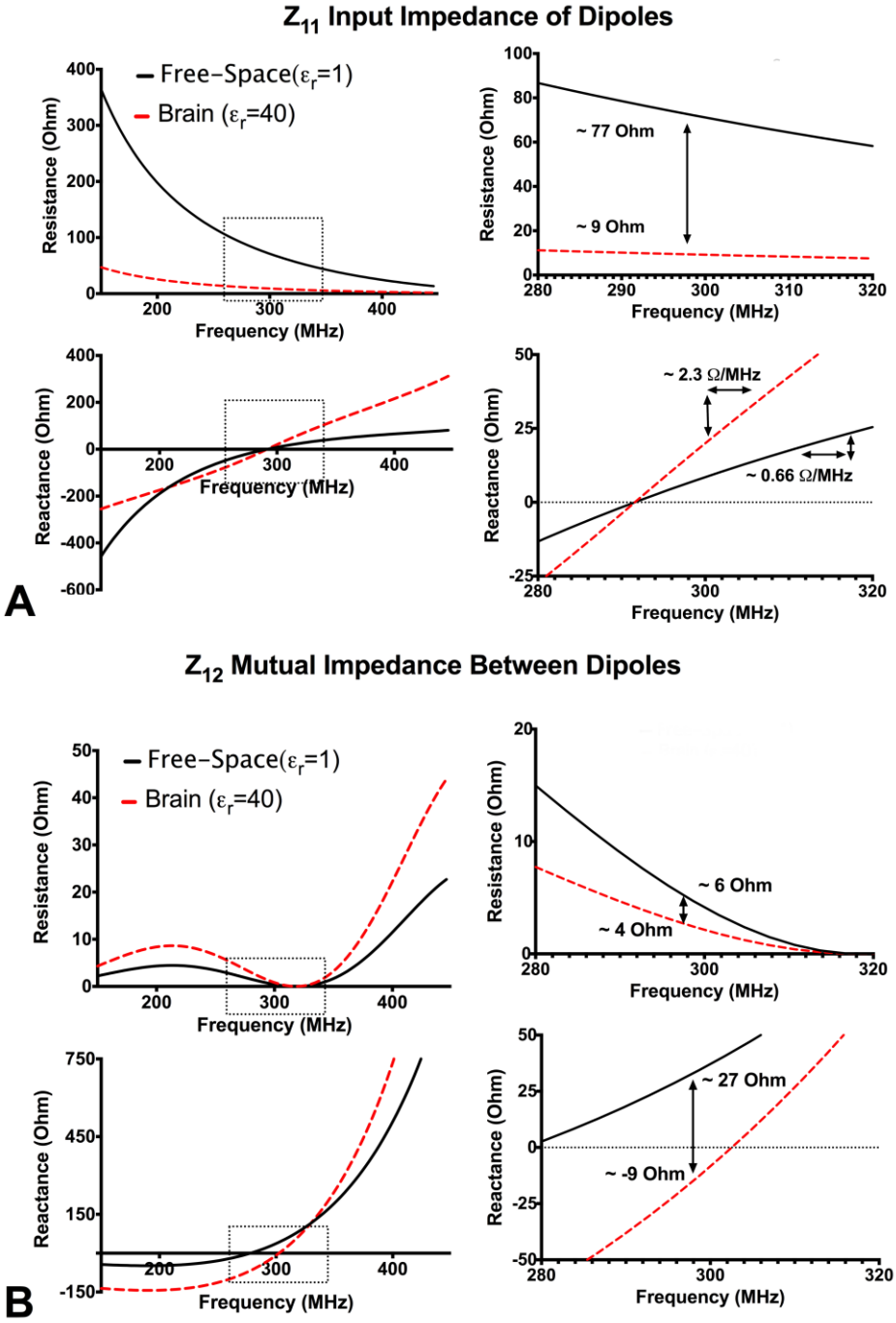


**Figure 48: (a) A comparison of the input impedance of two z-oriented resonating dipoles: in free-space and loaded with the electromagnetic properties of human brain tissue. (b) Effect of loading the two z-oriented dipoles with respect to their mutual impedance and the permittivity of the lossy medium.**

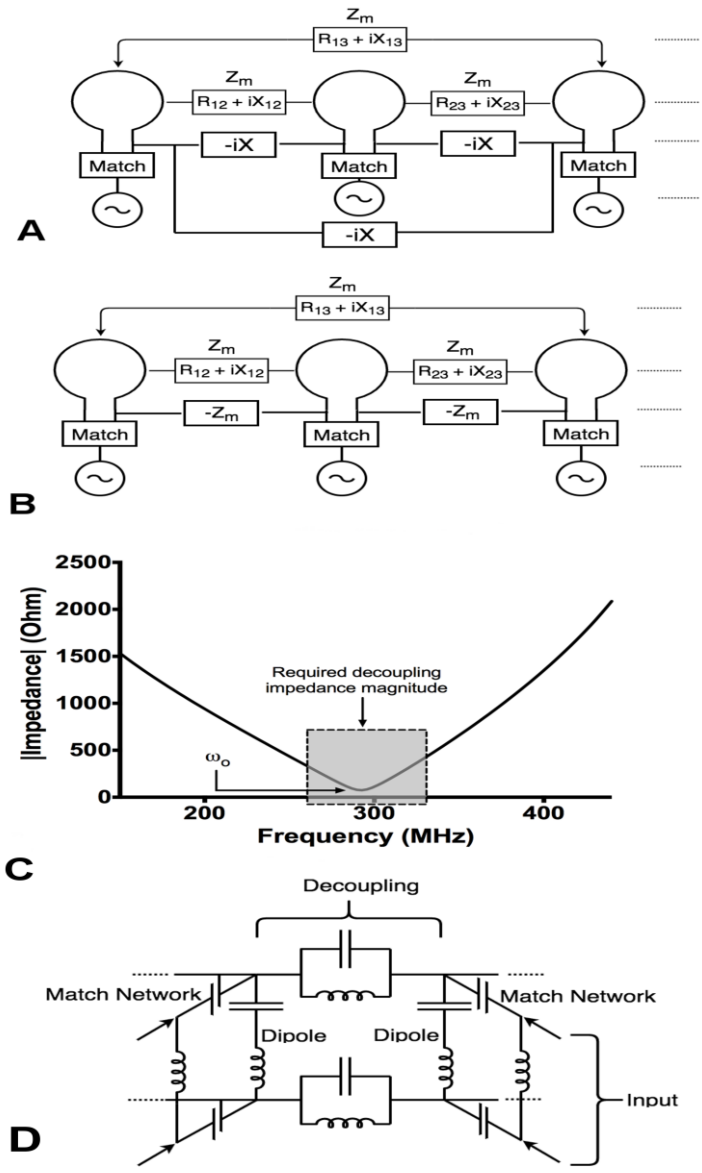


**Figure 49: (a) A sample illustration of a reactive decoupling scheme generalized for a number of elements located in an RF array. Mutual impedance '$Z_m$' is present between coupled elements. Reactive decoupling networks '-iX' compensate for mutual impedance and are placed between individual elements of the array to eliminate induced currents. (b) CMS method which takes the generalized approach in (a) and eliminates the need for second-order and higher networks to be placed between elements. (c) Solution for the decoupling element '-$Z_m$' self-impedance demonstrating the need for a resonant circuit due to the reactance-zero located on-resonance. (d) Circuit design for the conformal dipole array.**

### Footprint Reduction and Shape-Optimization

An efficiently radiating half-wave dipole, requires a total length of 48-cm in free-space. Due to additional loading mechanisms incurred via the sample and RF shield, the resonant dipole length is shortened, however in order to conform to the dimensions required for human head imaging, some form of additional electrical shortening is required. Typically, this takes the form of including additional lumped elements distributed along the length of the dipole, located at the end of the dipole, or feed points of the dipole with the goal of increasing total series inductance to achieve resonance [111]. Similarly, meandering portions of the dipole or specific sections thereof can achieve a suitable resonant length [112].

The contours of the dipole element conductors will determine the distribution of transverse magnetic field and absolute electric field in the sample. Manipulating the conductor dimensions in space provides degrees of freedom to optimize excitation or signal reception. The shape optimization exploits the fact that specific conductor paths can be designed to simultaneously produce field cancellation effects for the electric field, increase the absolute value of magnetic field that is projected onto the transverse plane, or a combination of both.

## Methods

### Mutual Coupling and Coupling Matrix Synthesis

The general decoupling solution presented in [113], ‘coupling matrix synthesis’ (CMS), is a suitable candidate for synthesizing the circuits requiring higher-order matrix decomposition methods for decoupling. CMS allows complex RF arrays of mixed element types and variable coupling coefficients to be efficiently decoupled with a ladder filter approach.

Coupling matrix synthesis (CMS) is an algorithm originally developed for coupled-cavity waveguide design [114]. We recently adapted this approach to construct ladder networks that perform decoupling and matching for general circuit topologies encountered in RF array design [115]. This flexible framework computes a series of ideal transfer

functions for a given array topology and inter-element coupling, and then performs a least-squares minimization across ladder element values to produce decoupling networks that minimize mutual impedance between matched array elements, while minimizing the complexity of the circuit design. It was demonstrated that for up to 32-channel conformal loop coils, a simple two-stage series resonator, placed only between adjacent elements, provided a mean isolation less than -20 dB across all nearest-neighbour RF array elements, without the use of loop overlap or preamplifier decoupling. Following from the circuit designs presented in [113], a CMS solution has been adapted for implementing the conformal, meandered dipole array.

Several reactive decoupling methods similar to CMS have been previously proposed [116-119] and the design of a typical array with reactive decoupling will follow a generic setup as demonstrated Fig. 49a. For these methods, the array geometry, feasibility of construction and magnitude of inter-element coupling dictate the number of reactive decoupling elements. CMS begins with the same building block. However, as demonstrated in [113], it is possible to implement a reactive decoupling mechanism that eliminates main-line and cross-coupling, without the insertion of additional reactive components between all coupled array elements. Therefore, a solution computed with the CMS algorithm follows the form of Fig 49b.

In order to compute a decoupling solution based on the form of Fig. 48b, the bandstop-filter circuit, presented in Fig. 49d, was utilized for physically realizing the array. This circuit can be readily transformed from the filter designs presented in Fig. 4, of [113]. As seen in Fig. 49d, the dipole elements compose the ladder legs of the RF array, with matching networks inserted, transforming the input impedance of the dipole input to power match the complex dielectric load. Additional resonant decoupling circuits complete the band-stop PI network, and the cascaded filter is tiled across to span the entire RF array.

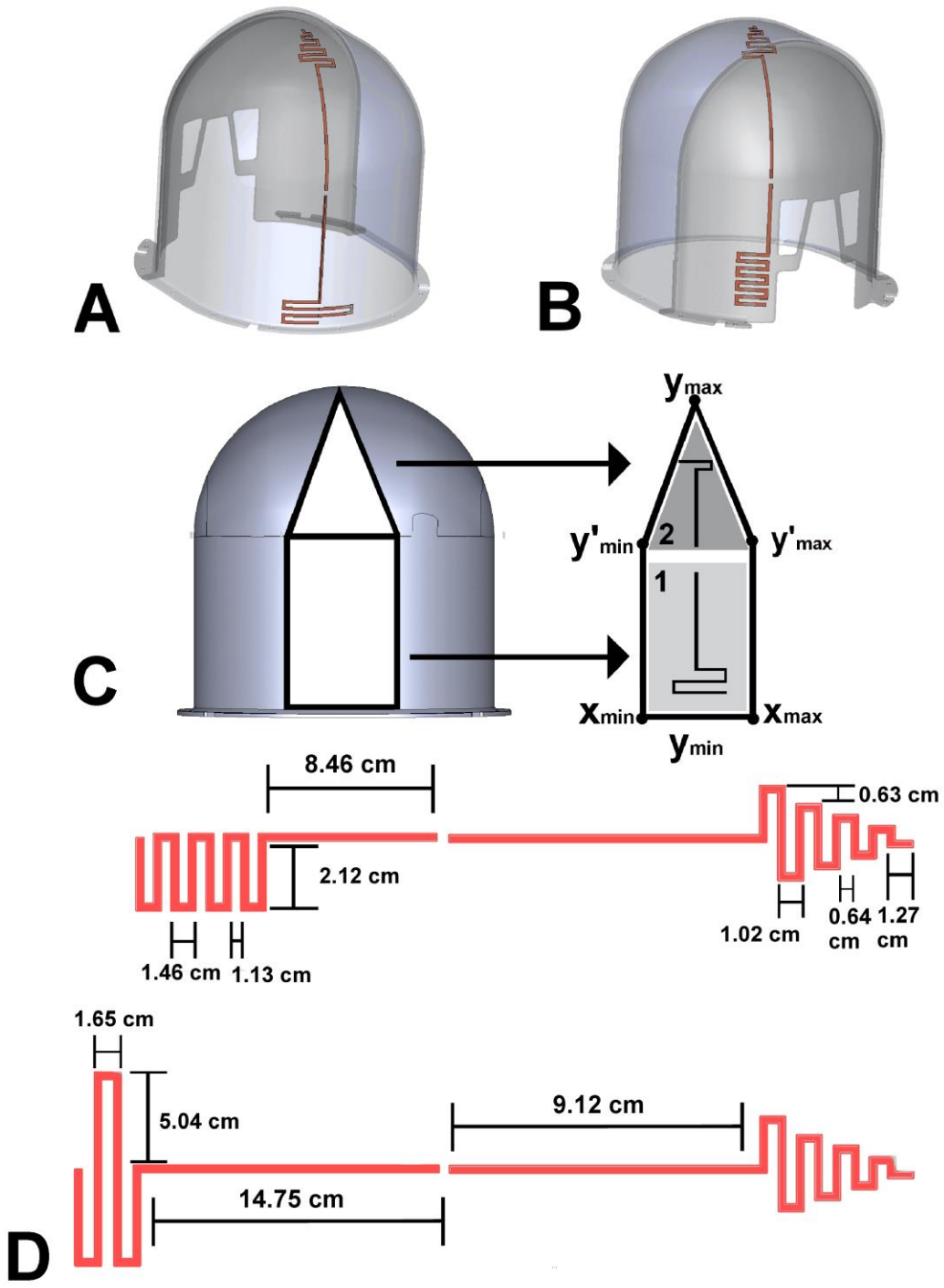


**Figure 50: Six of the eight dipoles follow the meander structure visible in (a) with optimized dimensions visible in (d). The final two dipoles, located at the anterior of the helmet former, follow the meandering structure presented in (b) with final dimensions in (d). Physical bounds for the shape optimization as well as the initial guess are provided in (c).**

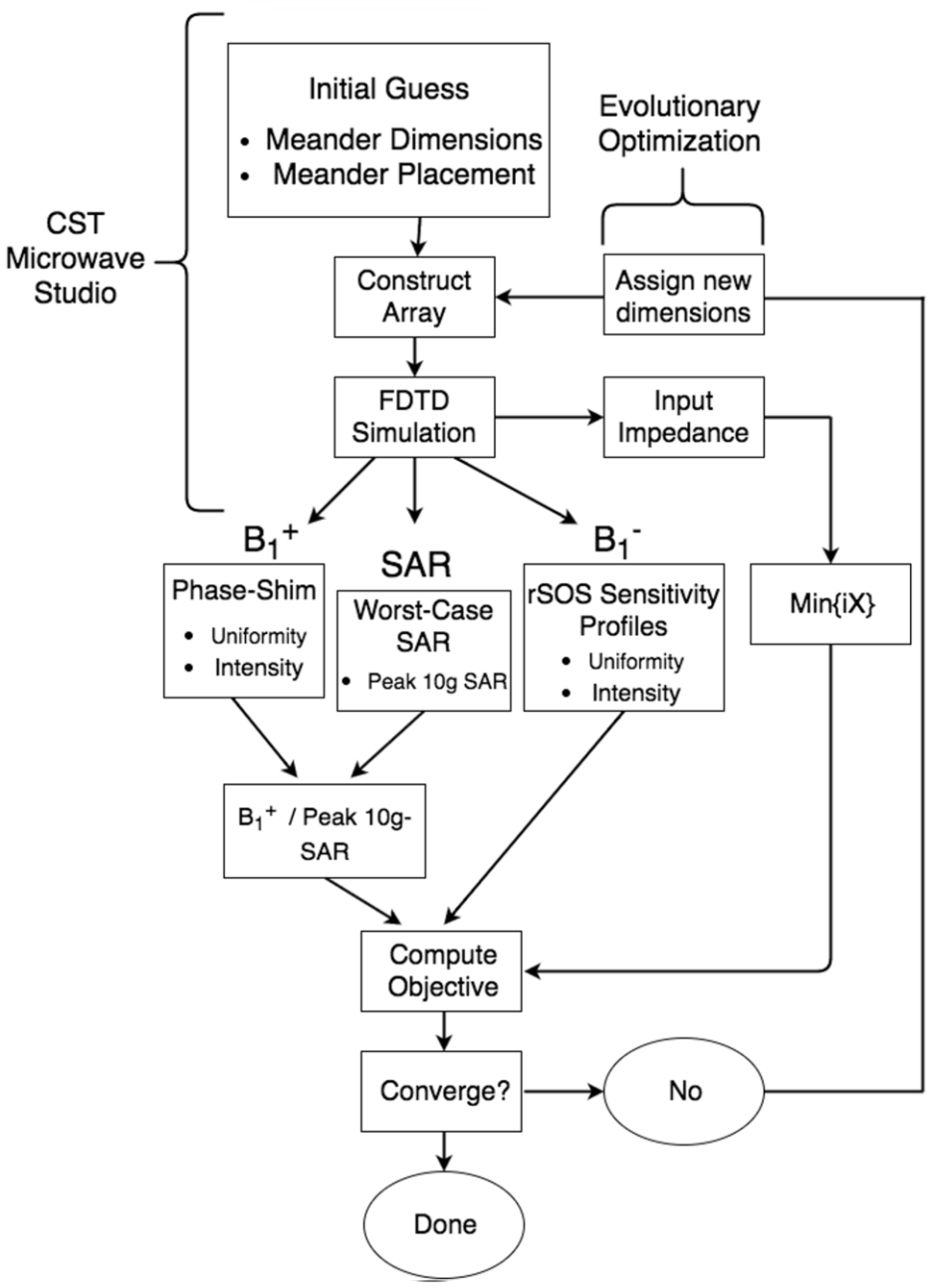


**Figure 50: Block diagram of the design algorithm utilized for synthesizing the conformal dipole geometry. The FDTD engine, supported by CST Microwave Studio, was iteratively called via the CMA-ES optimization routine for successive runs of altered dipole geometries. Post-processing of field results - including the calculation of $B_1^+/B_1^-$ fields, SAR, and input impedances - were performed inside CST studio at the conclusion of a FDTD simulation. A composite objective function was evaluated**

**at each step of the CMA-ES. Convergence was reached once successive generations of the solver failed to further minimize the objective function.**

## Shape Optimization and Array Design

The array was conformed to the 'helmet' former visible in Fig. 50a and Fig. 50b, with two building blocks designated to comprise the full array – six meandered dipoles visible in Fig. 50a and two differently meandered dipoles visible in Fig. 50b.

The building-block elements were defined as two-dimensional point clouds. Twenty-four points deposed along the XZ-plane defined the conductor geometry for both the top- and bottom-halves of the dipole (twelve points for top-half and twelve points for the bottom-half, respectively). These twenty-four points define the total number of input parameters in the dipole array optimization. With the point cloud defined, the dipole conductor paths were defined via a linearly interpolated line constructed through the XZ-plane point cloud. The interpolated line was then projected from the XZ-plane onto the helment former visible in Fig. 50, defining the conformal contours visible in Fig. 50a and Fig. 50b.

The meandering design of the dipole array elements was confined using two sets of boundary conditions as outlined in Fig. 50c. From Fig. 50c, the top-half of the dipoles was confined to a triangular portion of the upper portion of the helmet former. These upper and lower bounds for the optimization were defined in terms of barycentric coordinates for any possible point 'p':

$$a = \frac{\det\left(\vec{\boldsymbol{p}}, \left[\frac{x_{max} - x_{min}}{2}, y_{max}\right]\right) - \det\left([x_{min}, y'_{min}], \left[\frac{x_{max} - x_{min}}{2}, y_{max}\right]\right)}{\det\left([x_{max}, y'_{min}], \left[\frac{x_{max} - x_{min}}{2}, y_{max}\right]\right)} \quad (5.2a)$$

$$b = \frac{\det\left(\vec{\boldsymbol{p}}, [x_{max}, y'_{min}]\right) - \det([x_{min}, y'_{min}], [x_{max}, y'_{min}])}{\det\left([x_{max}, y'_{min}], \left[\frac{x_{max} - x_{min}}{2}, y_{max}\right]\right)} \quad (5.2b)$$

$$S.T. \begin{cases} a, b > 0 \\ a + b = 1 \end{cases}$$

Therefore, with the coordinates known, the lower and upper boundaries were defined in terms of 'a' and 'b':

$$Lower\ Bound \quad [a, b] > 0$$
$$Upper\ Bound \quad a + b = 1$$

For the lower half of the dipole, hard limits for the optimization were placed in terms of a simple rectangle bounded by [xmin, ymin], [xmax, y′min], [xmin, y′min], and [xmax, ymin], as visible in Fig. 50c. A pictorial representation of the initial guess is presented in Fig. 50c, where multiple collinear points defined the geometry. As evident in Fig. 50d, the optimization routine favoured 'pulling apart' the point cloud points such that the closest extends of the bounds in Fig. 50c were sampled.

The design of the conformal dipole array was performed in full-wave electromagnetic software (CST Microwave Studio, Darmstadt, Germany). The meander placement was optimized given initial dipole dimensions (see final dimensions in Fig. 49d) assigned as variables in a Covariance Matrix Adaptation Evolution Strategy (CMA-ES) algorithm supported by the CST Studio optimization toolbox – see Fig. 51 for the algorithm design. The XZ-plane point cloud and meander width was stochastically iterated across, guided by CMA-ES, until convergence based on the following criteria:

1. Modelling the sample as a large complex load, dipoles were conformed and meandered such that reactive input impedance of each individual dipole was minimized. This ensured the applied matching network would provide the greatest power deposition in the sample, and not in a conjugate matching stage.
2. $B_1^+$/10-g SAR was maximized.
3. $B_1^-$ coverage and mean intensity was maximized.

$B_1^+$ coverage and uniformity, given a phase-only RF shim was maximized.

## Array Construction

The dipole array was constructed on an elliptical former (minor and major axes: 17 cm and 21.5 cm, respectively). The close-fitting 'helmet', designed after the 'soccer ball' geometry introduced by Wiggins et al. (31), was affixed to the base of the elliptical former (see Fig. 52). The helmet spanned 25-cm in z direction.

The dipole array was composed of eight resonant dipoles (dimensions provided in Fig. 50d) implemented with 3.2 mm wide 2 oz. copper traces, routed atop 0.79-mm-thick garolite. Dipoles were matched to 50 Ω via low-pass PI matching circuits utilizing two variable capacitors (1 – 30 pF, 5600 series, Johanson Manufacturing, NJ) and one variable inductor (25 – 34 nH, Coilcraft, IL, USA). Sleeve baluns were constructed using triaxial cable (double braid shield, 20 AWG, Belden, IN, USA), and were directly fed to the dipole matching circuit from externally mounted BNC connectors. Decoupling circuits were applied in series with the dipoles – their positioning in the array is visible in Fig 52.

Due to the conformal geometry (see Fig. 52), one half of the balanced form of the decoupling network could be achieved by directly soldering the parallel inductor/capacitor ladder sections between dipoles located at the top of the head (see Fig. 52b). The second half of the decoupling network was connected via coaxial cables between elements (Fig. 52a). The additional capacitive phase shift induced in the decoupling portion of the ladder was compensated for via tuning the parallel inductor/capacitor section while measuring the impedance measured at the input of the two coaxial cables then used to attach the decoupling section to adjacent dipoles.

## Bench-top Measurements

All S-parameters were measured with a network analyzer (Agilent Technologies, model E5071C). S-parameters of both arrays were measured when loaded with an elliptical head-mimicking gel phantom (major diameter: 19 cm, minor diameter: 15.5 cm and 33 cm in height), placed approximately 2 cm from the elements. The gel phantom was composed of an outer annulus (2.1% agarose, 8-μM $GdCl_3$, $T_1/T_2$: 2000/55 msec) and 4.8-cm-diameter inner cylinder (2.2% agarose, 22-μM $GdCl_3$, $T_1/T_2$: 1300/45 msec) that represented gray and white matter, respectively [119].

The placement of a heterogeneous lossy dielectric in close proximity to a radiating dipole does not allow for direct measurement of radiation resistance – or an equivalent procedure performed on loop-based elements. This is due to the fact that, as demonstrated in Fig. 48, an equivalent circuit for a dipole antenna places the lossy sample in parallel with the dipole feed point resistance [120]. Therefore, full-wave simulation results that calculate

the surface impedance of the dipole element with discrete finite-elements, as well as in-scanner measurements, were utilized to measure the efficiency of the conformal dipole array as a tranceiver.

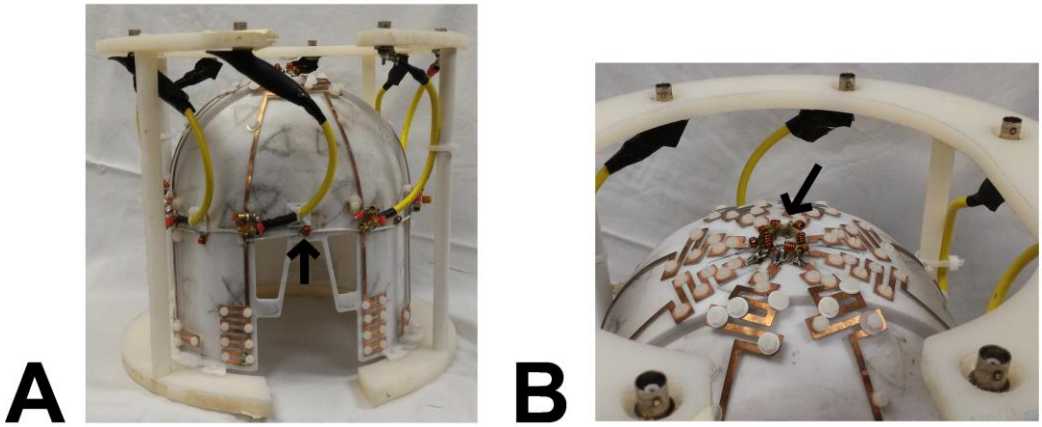


**Figure 51: (a) Isometric view of the constructed dipole array. One-half of the balanced bandstop ladder section utilized for decoupling the dipoles is presented in (b). Due to the conformal geometry, it was possible to directly solder the ladder sections between dipoles directly at the ends, located at the top of the conformal former. The second half of the decoupling ladder is visible in (a) where coaxial cables run from neighbouring dipoles along the virtual ground of the antennas.**

## MRI Measurements

All MR data collection (field mapping, parallel imaging performance and efficiency experiments) was performed on a human, head-only 7-T MRI scanner used in conjunction with a Step-2.3 pTx console (Siemens Healthcare, Erlangen, Germany). The system is equipped with an AC84 head gradient coil (maximum gradient strength: 80 mT/m, maximum slew rate: 400 mT/m/s, [Siemens Healthcare, Erlangen, Germany]) with a 36-cm-diameter clear bore. A slotted, copper RF shield is integrated into the inner-diameter of the AC84 head gradient coil to minimize coupling between the RF coil and gradients.

A custom transmit-receive (TR) switch was integrated into the existing transmit RF chain that allowed for transceive mode across all eight independent transmit/receive channels. Low-input-impedance preamplifiers (Siemens Healthcare, Erlangen, Germany)

were incorporated into the TR switches. Preamplifiers had a maximum noise figure of 0.6 dB and a gain of 26 dB. During transmission, an eight-channel power amplifier powered all channels with 1-kW peak power per channel with independent phase and magnitude control over pulse waveforms.

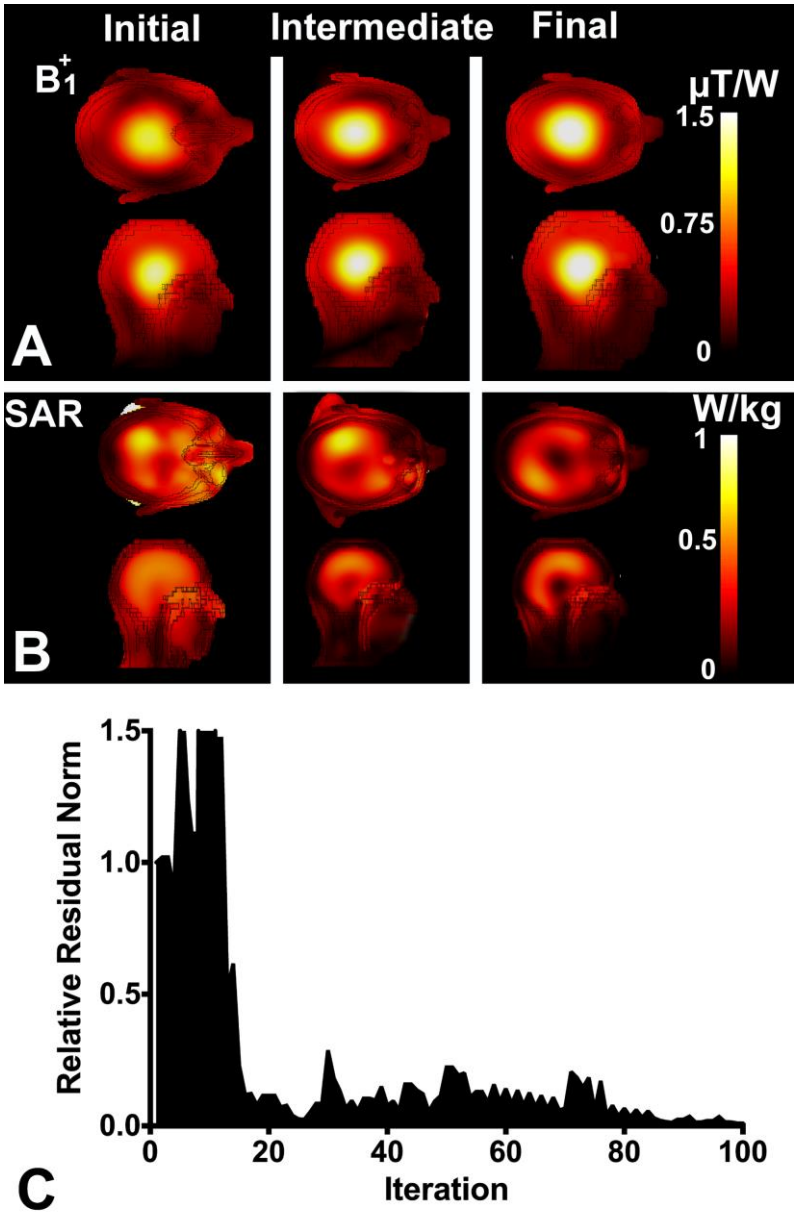


**Figure 52: (a) Phase-only shimmed $B_1^+$ maps computed across several representative time-steps of the optimization routine. (b) 'Worst-case' SAR maps computed for the same optimization time-steps. A clear reduction in both peak and global SAR levels is apparent. (c) Relative residual norm of the optimization procedure.**

A low flip-angle 3D gradient-recalled-echo volume was acquired for each transmit channel, according to the methods presented by Van de Moortele et al. [121], to produce relative $B_1^+$ maps (matrix size: 96 x 96 x 64; FOV: 25.6 x 25.6 x 25.6 $cm^3$; TE/TR: 3.3/8.3 ms; BW: 34 kHz; flip angle: 3º). The actual flip angle imaging (AFI) approach was then performed to calibrate the $B_1^+$ maps using the procedures presented by Yarnykh [122] and augmented with the RF and gradient spoiling schemes developed by Nehrke [123] (matrix size: 96 x 96 x 64; FOV: 25.6 x 25.6 x 25.6 $cm^3$; TE/TR1/TR2: 3.3/20/100 ms; BW: 34 kHz; flip angle: 70º).

Noise-only scans were acquired with the RF transmission turned off, receiving on all coil elements (matrix size: 96 x 96 x 64; FOV: 25.6 x 25.6 x 25.6 $cm^3$, BW: 34 kHz). Noise correlations were then estimated by calculating the pair-wise correlation coefficients between individual voxels across the full FOV. G-factor maps were generated via reconstructing individual acquisitions at set acceleration factors and comparing the reconstructed SNR to the SNR of a fully-sampled acquisition across the identical slice.

# Results

For all measurements, the uncertainty is quoted as one standard deviation, based upon the individual measurements contributing to the mean.

## Shape Optimization

An illustration of the optimization procedure as a function of time step is provided in Fig. 53. The shimmed transmit maps are presented in Fig. 53a with ‘worst-case’ computed SAR presented in Fig. 53b. The shimmed transmit maps in Fig. 53a demonstrate a modest increase in homogeneity across time-steps. However, a dramatic decrease in SAR is visible in Fig. 53b, demonstrating the influence of conductor meandering on electric field generation in the sample. Similarly, the relative residual norm plotted in Fig. 53c demonstrates the convergence of the algorithm outlined in Fig. 51. Runtime for a single iteration was ~15 min and included FDTD simulation, post-processing of results, computing objective functions and CMA-ES overhead. Total runtime accumulated to ~26 h for the entire procedure. Data visualization and communication between main controller and solver servers accounted for the additional time to complete the optimization.

## Impedance Matching and Decoupling

The conformal dipole array achieved a mean – 25 ± 3 dB reflection. The computed input impedance of dipole elements is presented in Fig. 54. It was found that the greatest magnitude of interaction between the bottom-half of the dipoles (see Fig. 52) occured near the feed-point. Thus, to decouple the bottom-half of the dipole, the second decoupling circuit was placed adjacent to the feed point.

Lumped element ladder values computed from CMS are provided in Table V. The mean ladder section impedance of the decoupling circuits was 910 ± 94 Ohm with a mean insertion loss of - 0.2 ± 0.1 dB. Measured S-parameters are provided in Table VI. The array achieved a mean -21.3 ± 3.4 transmission across all the elements in the array. Mean and worst-case transmission between nearest-neighbour dipoles was – 17.2 ± 2.4 dB and – 15.5 dB, respectively. Individual $B_1^+$ sensitivity profiles of the dipole array are provided in Fig. 55.

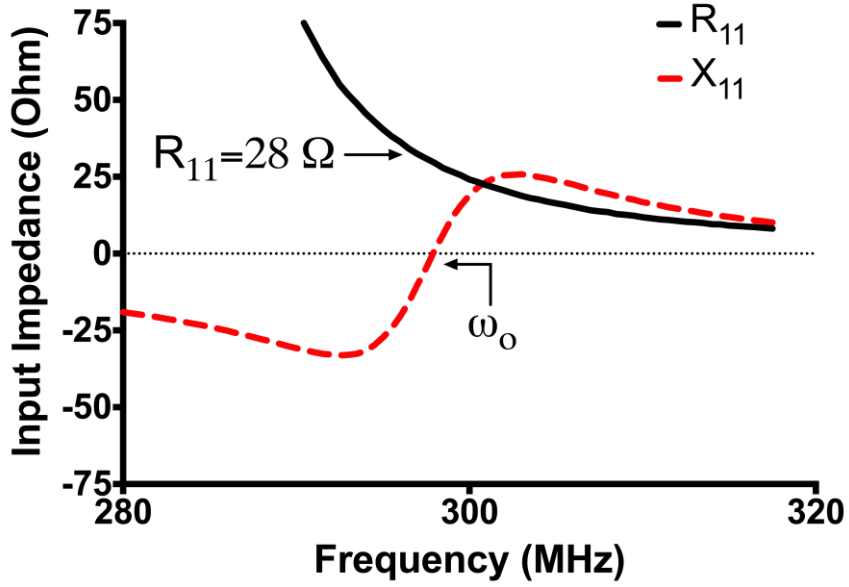


**Figure 53: The input impedance for a sample conformal dipole computed from FDTD software. On-resonance the input resistance has been increased to 28 Ohm from 9 Ohm as computed from the equivalent circuit presented in Fig. 48a.**

## Transmit Performance

The conformal dipole coil required a 101 V reference voltage to achieve a 70º flip-angle across the entire brain with a 1-ms square pulse and a 96 V reference voltage to achieve a 70º flip-angle across a 5-mm thick, central axial slice in the brain with a 1-ms square pulse. These reference voltages were obtained after the application of an RF shim solution and related to $B_1^+$ efficiencies of 22.4 $\mu T/\sqrt{kW}$ for the entire brain and 24.8 $\mu T/\sqrt{kW}$ across the axial slice. The transmit field uniformity achieved the dipole array across the entire head is demonstrated with flip-angle maps in Fig. 56a for a magnitude least-squares (MLS) shim solution and Fig. 56b for a slice-optimized spokes RF pulse design (4).

The standard deviation of the transmit field, after performing MLS shimming, over the axial, sagittal, and coronal planes of the whole-brain shim solution was 18%, 12%, and 14%, respectively. The standard deviation of the transmit field over the whole brain volume (to the posterior-most extent of the cerebellum) was 20%.

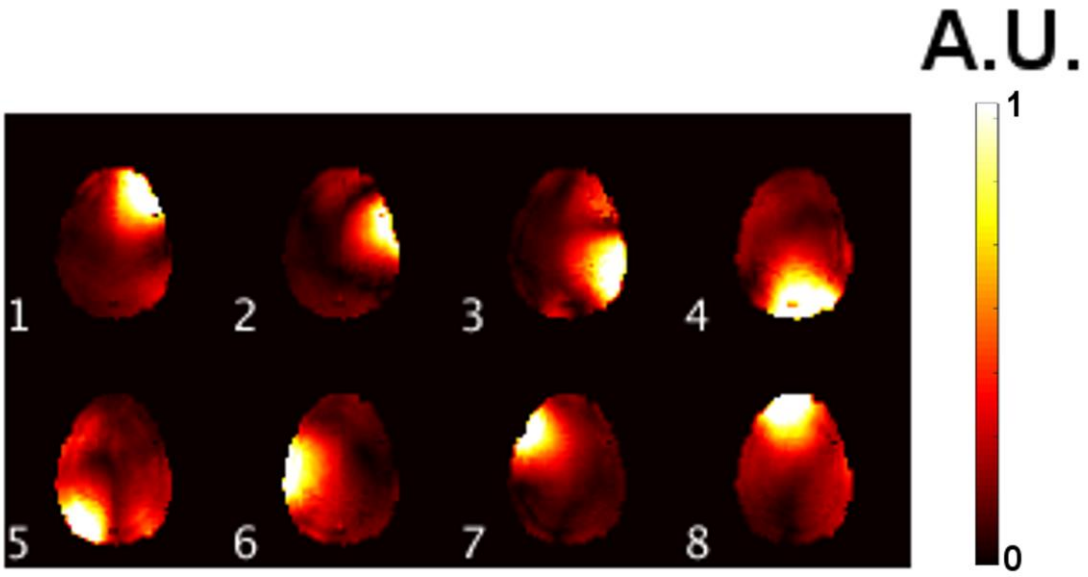


**Figure 54: Relative transmitter isolation maps. The dipole $B_1^+$ profiles demonstrate a high level of isolation between elements.**

The standard deviation of the transmit field, after performing RF-spokes slice optimization, over the central axial slice was 7.5%. The variance of the transmit field magnitude across the entire slice was 2%.

Accounting for peak 10g local SAR, the normalized $B_1^+$/10g-SAR was $12.5\ \mu T \cdot (W/kg)^{-1}$. The normalized $B_1^+$/10g-SAR for the initial conformal dipole dimensions was $6.67\ \mu T \cdot (W/kg)^{-1}$. Therefore, the optimization was successful in increasing the 'SAR efficiency' of the coil 1.9-fold.

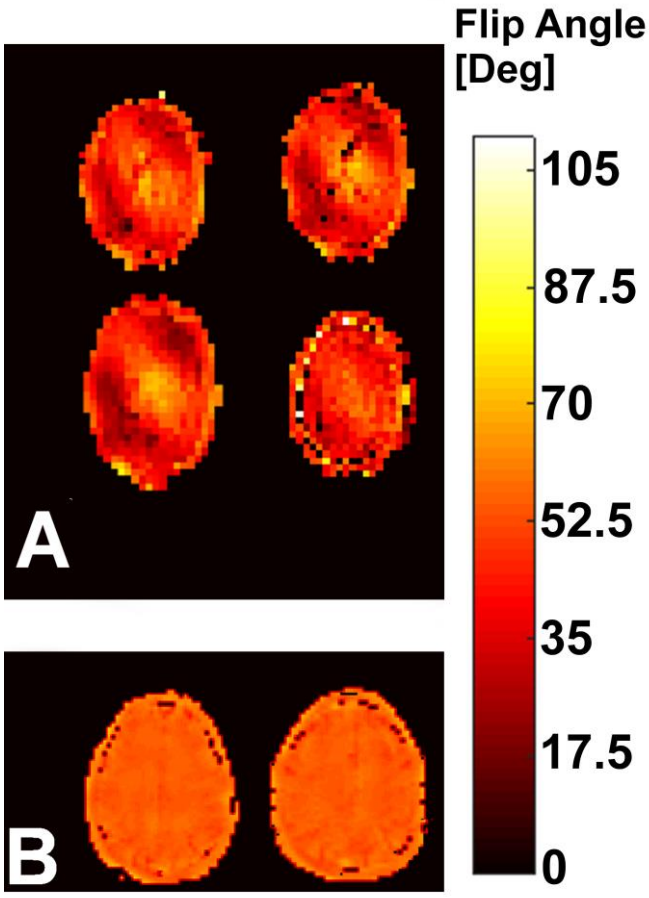


**Figure 55: Actual Flip Angle (AFI) maps obtained for the dipole array after performing: (a) a magnitude-least-squares shim and (b) a Spokes-RF pulse optimization across a centrally located axial slice.**

10-g SAR maps for the MLS shim solution computed from MRI experiments are presented in the final time step of Fig. 53b. The total and peak 10-g SAR, normalized to 1 W accepted input power per channel, was 0.163 W/kg and 0.601 W/kg for the dipole array, respectively. Areas of increased local 10-g SAR distribution include the eyeballs and along an annulus located just outside of the isocentre of the brain. As seen in Fig. 53b, the optimization routine reduces the number of local 10-g SAR 'hot-spots' as well as their relative intensity.

## Receive Performance

SNR for a central axial slice is presented in Fig. 57a. Noise correlations for the constructed array are provided in Table VII. The dipole array demonstrated a maximum noise correlation of 0.15 with a mean noise correlation of 0.023± 0.03. Inverse g-factors maps are provided in Fig. 57b for acceleration factors up to 3x3. Table 1 contains mean and maximum g-factors for the array calculated for each accelerated reconstruction.

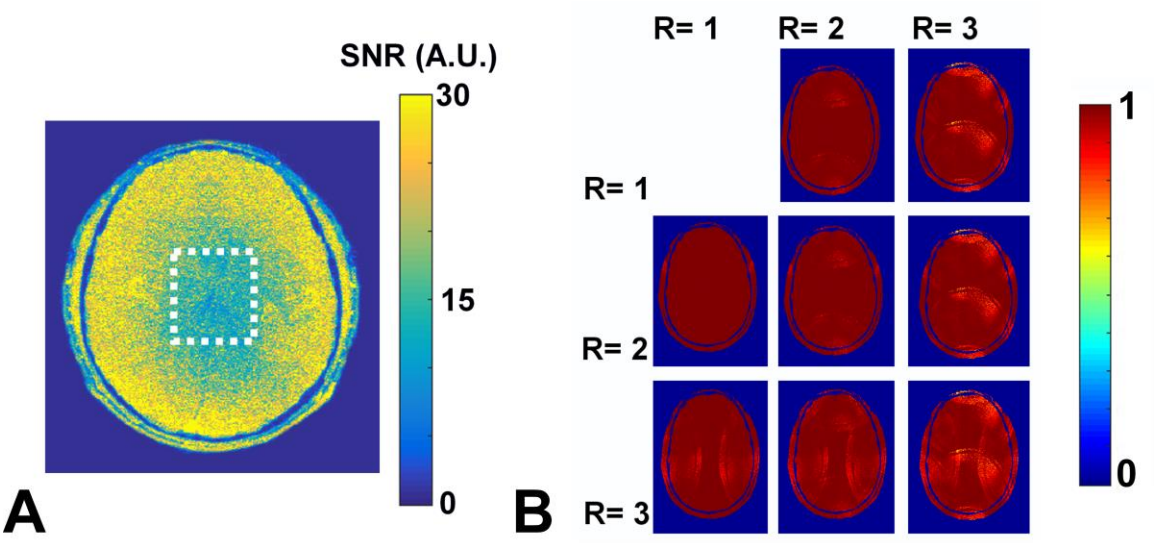


**Figure 56: (a) SNR maps for a centrally located axial slice. The ROI highlighted on image illustrates the drop in SNR for deep imaging targets in the human brain. (b) Inverse g-factor maps.**

# Discussion

## Impedance Matching and Decoupling

The constructed arrays were tightly coupled to the sample. Due to this, it was noted during construction that sample mediated (resistive and capacitive) interactions between array elements were a large contributing factor to both the mutual impedance between elements and the dipole input impedances. This follows from the equivalent circuit analysis provided in Fig. 48b.

In comparison to the theoretical, linearly-oriented dipole, as presented in Fig. 48, the input impedance curve in Fig. 54 demonstrate a much flatter response across a 40 MHz bandwidth about the resonant frequency and a higher absolute resistive component. This has a two-fold effect: a wider matching bandwidth and an increase in body-noise dominance. Therefore, for human head imaging at 7 T, it would appear that conforming dipoles increases sensitivity to the load and similarly reduces the effect of sample permittivity on reflected power due to impedance mismatch.

The bandstop topology derived from the CMS method utilized for the conformal design was effective at reducing the influence of coupling between elements to a suitable level for routine imaging. This is due to the fact that a resonant section can produce tuned inductive and capacitive impedance corrections centred about its resonant frequency. In the case of conformal dipole coupling, a 1$^{st}$-order bandstop filter topology could achieve the appropriate response. This is illustrated in the transmitter isolation maps provided in Fig. 55, S-parameters provided as Table VII, and the noise correlations provided in Table VII.

As seen in Table V, the individual section impedances for the decoupling circuits vary across the array. This is due to the CMS procedure. The decoupling method attempts to find a solution under which all dipole elements are decoupled. Therefore, with a variation in coupling throughout the array, multiple resonant frequencies are required to generate the subsequent poles that compensate for the mutual impedances between nearest- and beyond-neighbouring elements.

The CMS algorithm models the RF array as multiply terminated RF filter and can be implemented digitally for computation. Utilizing this concept, lumped element values were computed at each time step of the shape optimization. CMS ensured all candidate designs were adequately decoupled with the circuit presented in Fig. 49d. Automation of the decoupling procedure minimized the required human input for the optimization routine and allowed for a flexible construction procedure resulting in the unorthodox meandering structure. The dipole array was constructed free of the concern that the array could not be decoupled or effectively implemented after-the-fact. This lifted a significant portion of the burden for designing complex arrays where loop overlap or pre-amplifier decoupling or not readily available. To this end, CMS provided a robust and simple solution to implementing an array with more intricate dipole-shortening methods.

**Table V: Decoupling circuit values computed from CMS**

| Decoupling Circuit | Resonance [MHz] | Section Impedance [Ohm] |
|---|---|---|
| 1 | 297.4 | 1036 |
| 2 | 294.0 | 846 |
| 3 | 298.2 | 748 |
| 4 | 290.0 | 956 |
| 5 | 294.3 | 912 |
| 6 | 299.6 | 894 |
| 7 | 287.1 | 978 |

## Transmit Performance

In comparison to literature [125-127], the conformal dipole coil demonstrated comparable flip-angle distributions across the entire human brain. With a spokes-RF pulse

applied across a slice, the conformal dipole array achieved a high mean $B_1^+$ uniformity. As presented in Fig. 53, for subsequent time steps the conformal dipole array demonstrated increased $B_1^+$/10-g SAR values across the whole head with the MLS shim solution applied.

There are several physical mechanisms [102,127] contributing to an electric dipole's ability to generate $B_1^+$ inside a sample at UHF. These unique UHF electromagnetic interactions occur outside the magnetostatic regime and pose a design challenge for an optimal RF array. Therefore, the use of a machine-based optimization routine in conjunction with a finite-difference-time-domain (FDTD) engine is a powerful tool that allows the designer to approximate ideal temporal-spatial RF currents generated on a dipole array structure. This type of optimization method is an approximation to solving the inverse problem of projecting ideal current patterns occurring in the sample onto a constructible RF coil array.

The increased $B_1^+$/10-g SAR efficiency of the conformal dipole array is due to the method by which the CMA-ES algorithm penalized increases in the peak 10-g SAR for any given conformal meandering structure. In comparison to conventional loop-based RF arrays, conforming and meandering the dipole antenna pattern allows for array patterns that, when used in concert with an RF pulse optimization, can selectively shape the electric field patterns such that power deposition is minimized given the same sample-load distance.

Although originally posed as a design challenge, this form of shape optimization is a unique degree-of-freedom afforded by constructing an array with open-ended dipoles. The effect of electrically shortening a dipole antenna for use in human head imaging provides a unique opportunity to generate more efficient EM fields due to the optimization of conductor placement in the array. The unique conformal dipole geometry demonstrates that it is possible to simultaneously achieve the objectives of self-resonance and minimized electric field intensity across the tissue.

**Table VI: Maximum G-factor comparison for accelerated reconstruction across read and phase-encode directions.**

| **R** | 1 | 2 | 3 |
|---|---|---|---|
| 1 | | 1.2 | 1.6 |
| 2 | 1.1 | 1.2 | 1.6 |
| 3 | 1.3 | 1.5 | 1.7 |

**Table VII: Dipole Array S-Parameters [dB]**

| | 1 | 2 | 3 | 4 | 5 | 6 | 7 | 8 |
|---|---|---|---|---|---|---|---|---|
| 1 | -21.0 | -17.2 | -15.7 | -24.0 | -25.7 | -25.0 | -16.7 | -17.5 |
| 2 | | -22.1 | -15.6 | -19.3 | -24.6 | -22.3 | -23.5 | -15.5 |
| 3 | | | -27.1 | -17.0 | -19.3 | -20.5 | -22.0 | -24.8 |
| 4 | | | | -30.3 | -16.0 | -15.4 | -24.2 | -24.5 |
| 5 | | | | | -23.0 | -20.0 | -23.0 | -26.0 |
| 6 | | | | | | -28.6 | -23.0 | -16.3 |
| 7 | | | | | | | -22.2 | -15.5 |
| 8 | | | | | | | | -25.0 |

Worst-Case Coupling: -15.5

Mean Coupling: -21.3 ± 3.4

## Receive Performance

The benefits of reduced coupling between dipole elements (see Fig. 55) are clearly illustrated in the inverse g-factor maps provided in Fig. 57b. The isolated sensitivity profiles of the conformal dipole array provide full volume coverage and correlate to low maximum g-factors obtained during an accelerated acquisition.

**Table VIII: Dipole Array Noise Correlation**

| | 1 | 2 | 3 | 4 | 5 | 6 | 7 | 8 |
|---|---|---|---|---|---|---|---|---|
| 1 | | 0.0332 | 0.0038 | 0.0094 | 0.009 | 0.0234 | 0.0743 | 0.0082 |
| 2 | | | 0.0092 | 0.008 | 0.008 | 0.0085 | 0.0307 | 0.004 |
| 3 | | | | 0.0658 | 0.017 | 0.0121 | 0.0295 | 0.0112 |
| 4 | | | | | 0.0168 | 0.0099 | 0.0072 | 0.0201 |
| 5 | | | | | | 0.15 | 0.0093 | 0.0061 |
| 6 | | | | | | | 0.0093 | 0.0071 |
| 7 | | | | | | | | 0.0141 |
| 8 | | | | | | | | |

Maximum Noise Correlation: 0.15

Mean Noise Correlation: $0.023 \pm 0.03$

When receiving across the full sample FOV, the conformal dipole has a relative reduction in peripheral sensitivity of the dipole array in comparison to that of the loop RF array [128]. However, as seen in similar dipole RF array studies [103], the increased sensitivity of a dipole array across a centrally-located slice or an ROI located in the

isocentre of the sample provides unique opportunities for dipoles to be used alongside loop-based elements to increase SNR and coverage sensitivity –first presented in [129].

The conformal dipole sensitivity profiles are sufficiently orthonormal for clinically applicable acceleration factors up to 3x3. By example, for R = 1x3 and R = 2x1 acceleration, the mean accelerated SNR is reduced by a modest 6.3% and 13% when compared to the un-accelerated SNR, respectively. The insertion loss of individual decoupling circuits was -0.15 dB. This loss is on the order of that measured for the shielded baluns (-0.18 dB). The high input impedance of the decoupling circuits eliminated the possibility of parasitic current paths. Although the placement of the balanced decoupling network, at first observation, could potentially produce secondary electromagnetic fields that interfere with the generation of the desired $B_1$-field profiles, the high input impedance of decoupling sections demonstrated very-little-to-zero field generation occurring on either the coaxial cables connecting dipoles and decoupling circuits, or on the inductors.

The largest contributor to tuning and matching was proximity of the dipoles to the load. This is evident in both the transmitter isolation maps (Fig. 55) as well as the flip angles maps provided in Fig. 56 whereby any secondary magnetic fields generated by decoupling methods would interfere with the presented field profiles. The measured $B_1^+$ distributions of the dipole array characterized well-known UHF field patterns occurring in the human head [130]. Therefore, it is concluded that the CMS and chosen implementation of the decoupling method is quite suitable for implementing complex array geometries.

## Conclusion

In this study the application of several methods were presented for the first time in the construction of dipole-based RF arrays utilized for UHF MRI. Firstly, the MRI-adapted coupling matrix synthesis (CMS) method for designing RF arrays as a large, multiply terminated RF ladder filter was applied to an unorthodox meandering dipole structure and demonstrated excellent decoupling of an array structure not well-suited to decoupling by conventional methods. Secondly, due to the elimination of implementation barriers typically posed by other decoupling methods, an evolutionary computer algorithm (CMA-ES) was utilized to optimize the conductor paths of the dipole antennae. The sum total of

these techniques allowed the designers to construct a conformal dipole array that increased the body-noise of the dipole array, matching bandwidth and power delivered to the sample. Similarly, the 10-g SAR, transmission profile, and receive sensitivities of the transceiver array were passively optimized for a conformal array design.

## Acknowledgements

The authors would like to thank Peter Zeman for assistances in constructing the custom T/R switch and Dr. Kyle M. Gilbert for assistance during in-vivo MRI scanner experiments.

# Summary & Conclusion

This thesis presents several advancements in the field of MRI RF array design and construction. These advancements in array design were applied to the central research questions, posed at the beginning of the thesis:

(1) Does an increase in element-to-element isolation translate to increased imaging performance?
(2) Does a more flexible solution for isolating elements in an RF array remove implementation barriers for more sophisticated RF array designs that have potential benefits for UHF MRI?
(3) Is it possible to shape-optimize conducting structures to passively shape the electromagnetic fields responsible for SAR and nuclear excitation?

To address central question (1), a general framework, coupling matrix synthesis (CMS), was applied to model the complex electromagnetic coupling occurring in RF arrays. The CMS algorithm was designed specifically to increase isolation between elements in an RF array and incorporated several new features not previously addressed by current technology – the ability to decouple both nearest and next-nearest neighbours with filters placed only between adjacent elements and the ability to decouple non-loop based RF elements. The CMS algorithm also demonstrated that, for the first time, it was physically possible to fully decouple a 32-channel head coil without the use of element overlap or low-input impedance preamplifiers. A proof of principle was provided for the CMS algorithm that demonstrated high element isolation, and for the first time, RF elements decoupled with resonant, distributed-filters.

The CMS model was then utilized to synthesize a series of decoupling methods that included: (a) lumped element circuits and (b) distributed element filters (magnetic walls) for incorporation into full-scale RF arrays, designed for routine imaging. It was demonstrated that including these decoupling methods into the construction of state-of-the-art RF arrays improved element isolation in both full-wave simulation as well as with in-vivo MRI experiments, thus addressing central question (1) in a clinically-relevant setup.

However, for the case of both decoupling methods, modest efficiency losses were measured due to including additional lossy circuitry into the RF array.

Extending on the methods derived to solve question (1), it was demonstrated that for conformal dipole arrays a CMS decoupling method was able to isolate elements at a level previously unattained by conventional technology. The dipole structure that was successfully implemented with the CMS procedure was not readily decoupled by any other conventional means. Therefore, with analysis and simulation confirming that for a subset of challenging RF array constructions, especially those encountered during a shape optimization procedure, CMS is a convenient method for realizing highly conformal RF arrays designed for neuro-imaging. Thus providing evidence that CMS can address central question (2).

Finally, central question (3) was addressed through the use of a shape-optimization procedure to define the conductor paths of a conformal dipole array. The constructed array demonstrated a novel method by which SAR can be passively minimized for any given target excitation and was the first demonstration of an algorithm designed to intelligently design the meandering patterns of a MRI dipole array. The decrease in 10g SAR achieved with the conformal array was accompanied by a modest increase in excitation uniformity with a minimal influence on the overall efficiency of the excitation.

In summary, this thesis presented strong evidence that elimination of mutual coupling in RF arrays of complex geometry and large coil-counts is possible via simple circuits realized with the CMS approach. Additionally, the CMA-ES evolutionary algorithm was applied to the meandering structures of dipole elements that synthesized a conductor geometry that minimized electric field coil-patient interactions, thus reducing the overall SAR burden for any given acquisition. Due to the presence of intense electric fields near dipole elements, shape-optimization is a very promising method for mitigating the notoriously high power deposition produced by these element-types while simultaneously increasing their efficacy as an UHF transmitter.

Future extensions of this work include extending the shape optimization procedure laid out in Chapter 5, in conjunction with the CMS technique in Chapter 2 to construct

complex array geometries that exploit the electromagnetic environment to further minimize patient risk via reducing SAR. As was demonstrated by the conformal array, performance gains for RF arrays are possible when performing a shape-optimization, however the method by which the dipoles were shaped was not fully general. A target-field-approach, as seen in gradient coil design, is a natural candidate for applying a CMS-decoupled array and is possible in a finite-difference-time-domain regime.

The application of the CMS method to other RF arrays is another potentially advantageous method to construct RF arrays combining elements of dissimilar conductor pattern – i.e. loops and dipoles. The elimination of mutual coupling between these elements with a simple circuit approach allows a large increase in the degrees of freedom one can use to approach the problem of transmission uniformity. With current pulse-shaping algorithms still requiring high peak power deposition and an increase in the number of RF pulses required for field homogenization, increasing the number of elements and distinct radiation patterns in a transmit array is advantageous for simpler 'RF-shimming' strategies that rely heavily on the number of mutually independent transmit elements. The CMS method could be realized in several forms for any given array construction. Mixing lumped element circuits with distributed filters – such as the magnetic wall – provides an additional means by which arrays could be constructed.

Although distributed filters were the most lossy method by which decoupling was studied in this thesis, the use of magnetic walls, or structures similar thereto, still presents a simple solution to manufacturing RF arrays. Typically, construction of RF arrays is an iterative process and the use of a distributed filter; if efficiency is not of prime concern, has great potential for quickly manufacturing well-decoupled RF arrays.

The future of UHF MRI depends heavily upon the RF arrays that can be feasibly constructed and relied upon for clinical use. To-date, this has been a very active area of MRI engineering research and the advancements presented in this thesis go to great lengths in translating UHF MRI into the clinical environment.

# References


1. Hoult, D.I. and R.E. Richards, *The signal-to-noise ratio of the nuclear magnetic resonance experiment.* Journal of Magnetic Resonance (1969), 1976. **24**(1): p. 71-85.
2. Lattanzi, R. and D.K. Sodickson, *Ideal current patterns yielding optimal signal-to-noise ratio and specific absorption rate in magnetic resonance imaging: Computational methods and physical insights.* Magnetic Resonance in Medicine, 2012. **68**(1): p. 286-304.
3. Edelstein, W.A., Glover, G.H., Hardy, C.J. and Redington, R.W, *The Intrinsic Signal-to-Noise Ratio in NMR Imaging*. Magnetic Resonance in Medicine, 1986.**3**(1), p. 604-618.
4. Kozlov, Mikhail and Turner, Robert, *Dependence of near field transmit properties at 300 MHz of array element spatial distribution*. 2011 41st European Microwave Conference, Manchester, 2011, p.p. 1007-1010.
5. Avdievich, N.I., J.W. Pan, and H.P. Hetherington, *Resonant inductive decoupling (RID) for transceiver arrays to compensate for both reactive and resistive components of the mutual impedance.* NMR in biomedicine, 2013. **26**(11): p. 1547-1554.
6. Maunder, A.M., et al., *Stray Capacitance Between Magnetic Resonance Imaging Coil Elements: Models and Application to Array Decoupling.* Microwave Theory and Techniques, IEEE Transactions on, 2013. **61**(12): p. 4667-4677.
7. Connell, I.R.O., et al., *MRI RF Array Decoupling Method with Frequency Selective Magnetic Wall Filters.* IEEE Transactions on Medical Imaging, 2015. **44**(4): p. 825-835.
8. Li, B.K., et al., *An orthogonal-based decoupling method for MRI phased array coil design.* NMR Biomed, 2012. **25**(6): p. 835-42.
9. Gilbert, K.M., et al., *A radiofrequency coil to facilitate B-1(+) shimming and parallel imaging acceleration in three dimensions at 7 T.* NMR in biomedicine, 2011. **24**(7): p. 815-823.
10. Von Morze, C., et al., *An eight-channel, nonoverlapping phased array coil with capacitive decoupling for parallel MRI at 3 T.* Concepts in Magnetic Resonance Part B-Magnetic Resonance Engineering, 2007. **31B**(1): p. 37-43.
11. Lee, R.F., R.O. Giaquinto, and C.J. Hardy, *Coupling and decoupling theory and its application to the MRI phased array.* Magnetic Resonance in Medicine, 2002. **48**(1): p. 203-13.
12. Scott, G.C., et al., *General Signal Vector Decoupling for Transmit Arrays*, in *Proceedings of the Sixteenth Annual Meeting of ISMRM*. 2008: Toronto, ON. p. 168.
13. Hoult, D.I., et al., *The NMR multi-transmit phased array: a Cartesian feedback approach.* Journal of Magnetic Resonance, 2004. **171**(1): p. 64-70.
14. Roemer, P.B., et al., *The NMR Phased-Array.* Magnetic Resonance in Medicine, 1990. **16**(2): p. 192-225.
15. Hoult, D.I., G. Kolansky, and D. Kripiakevich, *A 'hi-fi' Cartesian feedback spectrometer for precise quantitation and superior performance.* Journal of Magnetic Resonance, 2004. **171**(1): p. 57-63.

16. Zelinski, A.C., et al., *Sparsity-enforced slice-selective MRI RF excitation pulse design.* IEEE Transactions on Medical Imaging, 2008. **27**(9): p. 1213-1229.
17. Setsompop, K., et al., *Magnitude least squares optimization for parallel radio frequency excitation design demonstrated at 7 Tesla with eight channels.* Magnetic Resonance in Medicine, 2008. **59**(4): p. 908-915.
18. Brunner, D.O. and K.P. Pruessmann, *Optimal Design of Multiple-Channel RF Pulses Under Strict Power and SAR Constraints.* Magnetic Resonance in Medicine, 2010. **63**(5): p. 1280-1291.
19. Liu, Y.N., et al., *Reducing SAR in parallel excitation using variable-density spirals: a simulation-based study.* Magnetic Resonance Imaging, 2008. **26**(8): p. 1122-1132.
20. Zhu, Y., *Parallel excitation with an array of transmit coils.* Magn Reson Med, 2004. **51**(4): p. 775-84.
21. Katscher, U., et al., *Transmit SENSE.* Magn Reson Med, 2003. **49**(1): p. 144-50.
22. Wiggins, G.C., et al., *96-Channel receive-only head coil for 3 Tesla: Design optimization and evaluation.* Magnetic Resonance in Medicine, 2009. **62**(3): p. 754-762.
23. Shajan, G., et al., *A 16-channel dual-row transmit array in combination with a 31-element receive array for human brain imaging at 9.4 T.* Magnetic Resonance in Medicine, 2014. **71**(2): p. 870-879.
24. Atia, A.E. and A.E. Williams, *Narrow-Bandpass Waveguide Filters.* Ieee Transactions on Microwave Theory and Techniques, 1972. **Mt20**(4): p. 258-&.
25. Cameron, R.J., *General coupling matrix synthesis methods for Chebyshev filtering functions.* IEEE Transactions on Microwave Theory and Techniques, 1999. **47**(4): p. 433-442.
26. Pinkerton, R.G., E.A. Barberi, and R.S. Menon, *Noise properties of a NMR transceiver coil array.* Journal of Magnetic Resonance, 2004. **171**(1): p. 151-6.
27. Hong, J.S. and M.J. Lancaster, *Couplings of microstrip square open-loop resonators for cross-coupled planar microwave filters.* IEEE Transactions on Microwave Theory and Techniques, 1996. **44**(11): p. 2099-2109.
28. Cameron, R.J., *Advanced coupling matrix synthesis techniques for microwave filters.* IEEE Transactions on Microwave Theory and Techniques, 2003. **51**(1): p. 1-10.
29. Terman, F.E., *Radio Engineering*. 1947: MacGraw-Hill.
30. Miraftab, V. and M. Yu, *Advanced coupling matrix and admittance function synthesis techniques for dissipative microwave filters.* Microwave Theory and Techniques, IEEE Transactions on, 2009. **57**(10): p. 2429-2438.
31. Amari, S., C. LeDrew, and W. Menzel, *Space-mapping optimization of planar coupled-resonator microwave filters.* Microwave Theory and Techniques, IEEE Transactions on, 2006. **54**(5): p. 2153-2159.
32. Amari, S. and U. Rosenberg, *Direct synthesis of a new class of bandstop filters.* Microwave Theory and Techniques, IEEE Transactions on, 2004. **52**(2): p. 607-616.
33. Raaijmakers, A.J.E., et al., *Design of a radiative surface coil array element at 7 T: The single-side adapted dipole antenna.* Magnetic Resonance in Medicine, 2011. **66**(5): p. 1488-1497.

34. Soutome, Y., Y. Otake, and Y. Bito, *Vertical Loop Decoupling Method for Gapped Phased-Array Coils*, in *Proceedings of the Nineteenth Annual Meeting of ISMRM*. 2011: Montreal, Quebec. p. 1859.
35. Li, Y., et al., *ICE decoupling technique for RF coil array designs.* Med Phys, 2011. **38**(7): p. 4086-4093.
36. Jevtic, J., *Ladder networks for capacitive decoupling in phased-array coils*, in *Proceedings of the 9th Annual Meeting of ISMRM*. 2001: Glasgow, Scotland. p. 17.
37. Barberi, E.A., et al., *A transmit-only/receive-only (TORO) RF system for high-field MRI/MRS applications.* Magnetic Resonance in Medicine, 2000. **43**(2): p. 284-9.
38. Bilotti, F., A. Toscano, and L. Vegni, *Design of spiral and multiple split-ring resonators for the realization of miniaturized metamaterial samples.* IEEE Trans Antennas Propag, 2007. **55**(8): p. 2258-2267.
39. Bilotti, F., et al., *Efficient modeling of the crosstalk between two coupled microstrip lines over nonconventional materials using an hybrid technique.* IEEE Transactions on Magnetics, 2008. **44**(6): p. 1482-1485.
40. Zhang, J., et al., *Sharp-rejection low-pass filter with controllable transmission zero using complementary split ring resonators (csrrs).* Progress in Electromagnetics Research-Pier, 2007. **69**: p. 219-226.
41. Baena, J.D., et al., *Equivalent-circuit models for split-ring resonators and complementary split-ring resonators coupled to planar transmission lines.* Ieee Transactions on Microwave Theory and Techniques, 2005. **53**(4): p. 1451-1461.
42. Bilotti, F., et al., *Equivalent-circuit models for the design of metamaterials based on artificial magnetic inclusions.* IEEE Transactions on Microwave Theory and Techniques, 2007. **55**(12): p. 2865-2873.
43. Mohan, S.S., et al., *Simple accurate expressions for planar spiral inductances.* IEEE Journal of Solid-State Circuits, 1999. **34**(10): p. 1419-1424.
44. Gilbert, K.M., et al., *A radiofrequency coil to facilitate B(1)(+) shimming and parallel imaging acceleration in three dimensions at 7 T.* NMR Biomed, 2011. **24**(7): p. 815-23.
45. Ortiz, J.D., et al., *Spatial Angular Filtering by FSSs Made of Chains of Interconnected SRRs and CSRRs.* IEEE Microwave and Wireless Components Letters, 2013. **23**(9): p. 477-479.
46. Alici, K.B., et al., *Miniaturized negative permeability materials.* Applied Physics Letters, 2007. **91**(7).
47. Shang, X., et al., *Design of multiple-passband filters using coupling matrix optimisation.* IET Microwaves Antennas & Propagation, 2012. **6**(1): p. 24-30.
48. Michalski, J.J., et al., *Coupling Matrix Synthesis by Optimization with Cost Function Based on Daubechies D4 Wavelet Transform.* Piers 2012 Moscow: Progress in Electromagnetics Research Symposium, 2012: p. 1351-1354.
49. Skaik, T.F., M.J. Lancaster, and F. Huang, *Synthesis of multiple output coupled resonator circuits using coupling matrix optimisation.* IET Microwaves Antennas & Propagation, 2011. **5**(9): p. 1081-1088.
50. Vincent, T., B. Powers, and I. Bar-On, *The influence of substrate surface roughness on microstrip transmission line loss using conventional analyses and length-scale fractal analysis.* Surface and Interface Analysis, 2010. **42**(1): p. 21-35.

51. Vincent, T.S., Y. Itovich, and I. Bar-On, *Quantitative Edge Cross-Section Angle Impact on Conductor Loss.* IEEE Transactions on Components and Packaging Technologies, 2010. **33**(2): p. 386-390.
52. Munk, B.A., *Frequency Selective Surfaces: Theory and Design*. 2005: John Wiley & Sons.
53. Wiltshire, M.C., et al., *Microstructured magnetic materials for RF flux guides in magnetic resonance imaging.* Science, 2001. **291**(5505): p. 849-51.
54. Allard, M. and R.M. Henkelman, *Using metamaterial yokes in NMR measurements.* Journal of Magnetic Resonance, 2006. **182**(2): p. 200-7.
55. Algarin, J.M., et al., *Signal-to-noise ratio evaluation in resonant ring metamaterial lenses for MRI applications.* New Journal of Physics, 2011. **13**.
56. Erni, D., et al., *Highly adaptive RF excitation scheme based on conformal resonant CRLH metamaterial ring antennas for 7-Tesla traveling-wave magnetic resonance imaging.* Conf Proc IEEE Eng Med Biol Soc, 2011. **2011**: p. 554-8.
57. Mosig, J., et al., *Design and Characteristics of a metamaterial transmit/receive coil element for 7 Tesla MRI.* World Congress on Medical Physics and Biomedical Engineering, Vol 25, Pt 2 - Diagnostic Imaging, 2009. **25**: p. 173-176.
58. Wiggins, G.C., et al., *32-channel 3 Tesla receive-only phased-array head coil with soccer-ball element geometry.* Magnetic Resonance in Medicine, 2006. **56**(1): p. 216-23.
59. Gilbert, K.M., et al., *Transmit/receive radiofrequency coil with individually shielded elements.* Magnetic Resonance in Medicine, 2010. **64**(6): p. 1640-51.
60. Klassen, L.M. and R.S. Menon, *Robust automated shimming technique using arbitrary mapping acquisition parameters (RASTAMAP).* Magnetic Resonance in Medicine, 2004. **51**(5): p. 881-7.
61. Van de Moortele PF, U.K. *Very Fast Multi Channel B1 Calibration at High Field in the Small Flip Angle Regime*. in *Proceedings of the 17th Annual Meeting ISMRM*. 2009. Honolulu, Hawaii, USA.
62. Yarnykh, V.L., *Actual flip-angle imaging in the pulsed steady state: a method for rapid three-dimensional mapping of the transmitted radiofrequency field.* Magnetic Resonance in Medicine, 2007. **57**(1): p. 192-200.
63. Nehrke, K., *On the steady-state properties of actual flip angle imaging (AFI).* Magnetic Resonance in Medicine, 2009. **61**(1): p. 84-92.
64. Curtis, A.T., et al., *Slice-by-slice B1+ shimming at 7 T.* Magnetic Resonance in Medicine, 2012. **68**(4): p. 1109-16.
65. Bitz, A.K., et al., *Assessment of RF Safety of Transmit Coils at 7 Tesla by Experimental and Numerical Procedures*, in *Proceedings of the International Society for Magnetic Resonance in Medicine*. 2011: Montreal. p. 490.
66. Collins, C.M., et al., *Temperature and SAR calculations for a human head within volume and surface coils at 64 and 300 MHz.* Journal of Magnetic Resonance Imaging, 2004. **19**(5): p. 650-656.
67. Bait-Suwailam, M.M., O.F. Siddiqui, and O.M. Ramahi, *Mutual Coupling Reduction Between Microstrip Patch Antennas Using Slotted-Complementary Split-Ring Resonators.* IEEE Antennas and Wireless Propagation Letters, 2010. **9**: p. 876-878.

68. Setsompop, K., et al., *Slice-selective RF pulses for in vivo B 1+ inhomogeneity mitigation at 7 tesla using parallel RF excitation with a 16-element coil.* Magnetic Resonance in Medicine, 2008. **60**(6): p. 1422-1432.
69. Grissom, W., et al., *Spatial domain method for the design of RF pulses in multicoil parallel excitation.* Magnetic Resonance in Medicine, 2006. **56**(3): p. 620-629.
70. Hoult, D.I. and D. Phil, *Sensitivity and power deposition in a high-field imaging experiment.* Journal Magnetic Resonance Imaging, 2000. **12**(1): p. 46-67.
71. Deniz, C.M., et al., *Maximum efficiency radiofrequency shimming: Theory and initial application for hip imaging at 7 tesla.* Magnetic Resonance in Medicine, 2013. **69**(5): p. 1379-1388.
72. Zhang, Z., et al., *Reduction of transmitter B1 inhomogeneity with transmit SENSE slice-select pulses.* Magnetic Resonance in Medicine, 2007. **57**(5): p. 842-7.
73. Cloos, M.A., et al., *Local SAR reduction in parallel excitation based on channel-dependent Tikhonov parameters.* Journal of Magnetic Resonance Imaging, 2010. **32**(5): p. 1209-1216.
74. Guérin, B., et al., *Design of parallel transmission pulses for simultaneous multislice with explicit control for peak power and local specific absorption rate.* Magnetic Resonance in Medicine, 2015. **73**(5): p. 1946-1953.
75. Sodickson, D.K. and W.J. Manning, *Simultaneous acquisition of spatial harmonics (SMASH): fast imaging with radiofrequency coil arrays.* Magnetic Resonance in Medicine, 1997. **38**(4): p. 591-603.
76. Pruessmann, K.P., et al., *SENSE: Sensitivity encoding for fast MRI.* Magnetic Resonance in Medicine, 1999. **42**(5): p. 952-962.
77. Griswold, M.A., et al., *Generalized autocalibrating partially parallel acquisitions (GRAPPA).* Magnetic Resonance in Medicine, 2002. **47**(6): p. 1202-1210.
78. Wiggins, G.C., et al., *The electric dipole array: an attempt to match the ideal current pattern for central SNR at 7 Tesla.* Proceedings of the 20th Annual Meeting of ISMRM, Melbourne, Australia, 2012: p. 541.
79. Eryaman, Y., et al., *SAR reduction in 7T C- spine imaging using a "dark modes" transmit array strategy.* Magnetic Resonance in Medicine, 2015. **73**(4): p. 1533-1539.
80. Wiggins, G., et al., *Mixing Loops and Electric Dipole Antennas for Increased Sensitivity at 7 Tesla.* Proceedings of the 21st Annual Meeting of ISMRM, Salt Lake City, USA, 2013: p. 2737.
81. Chen, G., et al., *Approaching the Ultimate Intrinsic SNR with Dense Arrays of Electric Dipole Antennas*, in *24th Annual meeting for International Society for Mangetic Resonance in Medicine*. 2016, ISMRM: Singapore.
82. Connell, IRO. and R. Menon, *General Coupling Matrix Synthesis for Decoupling MRI RF Arrays.* IEEE Transactions on Medical Imaging, 2016. **35** (10): p.2229-2242.
83. Cameron, R.J., *General coupling matrix synthesis methods for Chebyshev filtering functions.* Microwave Theory and Techniques, IEEE Transactions on, 1999. **47**(4): p. 433-442.
84. Wiggins, G., K. Lakshmanan, and G. Chen, *The Distributed Inductance Electric Dipole Antenna*, in *23rd Annual Meeting of the International Society for Magnetic Resonance in Medicine*. 2015, ISMRM: Toronto, Canada.

85. Raaijmakers, A.J.E., et al., *The fractionated dipole antenna: A new antenna for body imaging at 7 Tesla.* Magnetic Resonance in Medicine, 2016. **75**(3): p. 1366-1374.
86. Balanis, C.A., *Antenna Theory: Analysis and Design*. 2005: Wiley-Interscience.
87. Raaijmakers, A.J.E., P.R. Luijten, and C.A.T. van den Berg, *Dipole antennas for ultrahigh-field body imaging: a comparison with loop coils.* NMR in Biomedicine, 2015: p. n/a-n/a.
88. Wiggins, G., et al., *The Electric Dipole Array: An Attempt to Match the Ideal Current Pattern for Central SNR at 7 Tesla*, in *20th Annual Meeting of the International Society for Magnetic Resonance in Medicine*. 2012, ISMRM: Melbourne, Australia.
89. Wiggins, G., et al., *Mixing Loops and Electric Dipole Antennas for Increased Sensitivity at 7 Tesla*, in *21st Annual Meeting of the Internation Society for Magnetic Resonance in Medicine*. 2013, ISMRM: Salt Lake City, USA.
90. Collins, C.M., et al., *Central brightening due to constructive interference with, without, and despite dielectric resonance.* Journal of Magnetic Resonance Imaging, 2005. **21**(2): p. 192-196.
91. Katscher U, Bornert P, Leussler C, van den Brink JS. *Transmit SENSE*. Magn Reson Med 2003;49(1):144-150.
92. Zhu Y. *Parallel excitation with an array of transmit coils*. Magn Reson Med 2004;51(4):775-784.
93. Setsompop K, Alagappan V, Gagoski B, Witzel T, Polimeni J, Potthast A, Hebrank F, Fontius U, Schmitt F, Wald LL, Adalsteinsson E. *Slice-selective RF pulses for in vivo B 1+ inhomogeneity mitigation at 7 tesla using parallel RF excitation with a 16-element coil*. Magn Reson Med 2008;60(6):1422-1432.
94. Grissom W, Yip CY, Zhang ZH, Stenger VA, Fessler JA, Noll DC. *Spatial domain method for the design of RF pulses in multicoil parallel excitation*. Magn Reson Med 2006;56(3):620-629.
95. Hoult DI, Phil D. *Sensitivity and power deposition in a high-field imaging experiment. Journal of magnetic resonance imaging* : JMRI 2000;12(1):46-67.
96. Curtis AT, Gilbert KM, Klassen LM, Gati JS, Menon RS. *Slice-by-slice B1+ shimming at 7 T*. Magn Reson Med 2012;68(4):1109-1116.
97. Deniz CM, Brown R, Lattanzi R, Alon L, Sodickson DK, Zhu YD. *Maximum efficiency radiofrequency shimming: Theory and initial application for hip imaging at 7 tesla*. Magn Reson Med 2013;69(5):1379-1388.
98. Zhang Z, Yip CY, Grissom W, Noll DC, Boada FE, Stenger VA. *Reduction of transmitter B1 inhomogeneity with transmit SENSE slice-select pulses*. Magn Reson Med 2007;57(5):842-847.
99. Cloos MA, Luong M, Ferrand G, Amadon A, Le Bihan D, Boulant N. *Local SAR reduction in parallel excitation based on channel-dependent Tikhonov parameters*. Journal of Magnetic Resonance Imaging 2010;32(5):1209-1216.
100. Guérin B, Setsompop K, Ye H, Poser BA, Stenger AV, Wald LL. *Design of parallel transmission pulses for simultaneous multislice with explicit control for peak power and local specific absorption rate*. Magn Reson Med 2015;73(5):1946-1953.

101. Sodickson DK, Manning WJ. *Simultaneous acquisition of spatial harmonics (SMASH): fast imaging with radiofrequency coil arrays*. Magn Reson Med 1997;38(4):591-603.
102. Pruessmann KP, Weiger M, Scheidegger MB, Boesiger P. *SENSE: Sensitivity encoding for fast MRI*. Magn Reson Med 1999;42(5):952-962.
103. Griswold MA, Jakob PM, Heidemann RM, Nittka M, Jellus V, Wang J, Kiefer B, Haase A. *Generalized autocalibrating partially parallel acquisitions (GRAPPA)*. Magn Reson Med 2002;47(6):1202-1210.
104. Lattanzi R, Sodickson DK. *Ideal current patterns yielding optimal signal-to-noise ratio and specific absorption rate in magnetic resonance imaging*: *Computational methods and physical insights*. Magn Reson Med 2012;68(1):286-304.
105. Raaijmakers AJE, Ipek O, Klomp DWJ, Possanzini C, Harvey PR, Lagendijk JJW, van den Berg CAT. *Design of a radiative surface coil array element at 7 T: The single-side adapted dipole antenna*. Magn Reson Med 2011;66(5):1488-1497.
106. Wiggins GC, Zhang B, Lattanzi R, Chen G, Sodickson D. *The electric dipole array: an attempt to match the ideal current pattern for central SNR at 7 Tesla*. Proceedings of the 20th Annual Meeting of ISMRM, Melbourne, Australia 2012:541.
107. Eryaman Y, Guerin B, Keil B, Mareyam A, Herraiz JL, Kosior RK, Martin A, Torrado-Carvajal A, Malpica N, Hernandez-Tamames JA. *SAR reduction in 7T C-spine imaging using a "dark modes" transmit array strategy*. Magn Reson Med 2015;73(4):1533-1539.
108. Wiggins G, Zhang B, Cloos M, Lattanzi R, Chen G, Lakshmanan K, Haemer G, Sodickson D. *Mixing Loops and Electric Dipole Antennas for Increased Sensitivity at 7 Tesla*. Proceedings of the 21st Annual Meeting of ISMRM, Salt Lake City, USA 2013:2737.
109. Chen G, Lattanzi R, Sodickson D, Wiggins G. *Approaching the Ultimate Intrinsic SNR with Dense Arrays of Electric Dipole Antennas*. 24th Annual meeting for International Society for Mangetic Resonance in Medicine. Singapore: ISMRM; 2016.
110. Liao Y, Hubing TH, Su D. *Equivalent Circuit for Dipole Antennas in a Lossy Medium*. IEEE Transactions on Antennas and Propagation 2012;60(8):3950-3953.
111. van Heteren JG, Henkelman RM, Bronskill MJ. *Equivalent circuit for coil-patient interactions in magnetic resonance imaging*. Magnetic Resonance Imaging 1987;5(2):93-99.
112. Wiggins G, Lakshmanan K, Chen G. *The Distributed Inductance Electric Dipole Antenna*. 23rd Annual Meeting of the International Society for Magnetic Resonance in Medicine. Toronto, Canada: ISMRM; 2015.
113. Raaijmakers AJE, Italiaander M, Voogt IJ, Luijten PR, Hoogduin JM, Klomp DWJ, van den Berg CAT. *The fractionated dipole antenna: A new antenna for body imaging at 7 Tesla*. Magnetic Resonance in Medicine 2016;75(3):1366-1374.
114. Connell I, Menon R. *General Coupling Matrix Synthesis for Decoupling MRI RF Arrays*. IEEE transactions on medical imaging 2016.
115. Cameron RJ. *General coupling matrix synthesis methods for Chebyshev filtering functions*. Microwave Theory and Techniques, IEEE Transactions on 1999;47(4):433-442.

116. Jevtic J. *Ladder networks for capacitive decoupling in phased-array coils*. Proceedings of the 9th Annual Meeting of ISMRM. Glasgow, Scotland2001. p 17.
117. Lee RF, Giaquinto RO, Hardy CJ. *Coupling and decoupling theory and its application to the MRI phased array*. Magn Reson Med 2002;48(1):203-213.
118. Avdievich NI, Pan JW, Hetherington HP. *Resonant Inductive Decoupling (RID) for Transceiver Arrays to Compensate for both Reactive and Resistive Components of the Mutual Impedance*. NMR in biomedicine 2013;26(11):1547-1554.
119. Shajan G, Kozlov M, Hoffmann J, Turner R, Scheffler K, Pohmann R. *A 16-channel dual-row transmit array in combination with a 31-element receive array for human brain imaging at 9.4 T*. Magnetic Resonance in Medicine 2014;71(2):870-879.
120. Wiggins GC, Triantafyllou C, Potthast A, Reykowski A, Nittka M, Wald LL. *32-channel 3 Tesla receive-only phased-array head coil with soccer-ball element geometry*. Magn Reson Med 2006;56(1):216-223.
121. Gilbert KM, Curtis AT, Gati JS, Klassen LM, Villemaire LE, Menon RS. *Transmit/receive radiofrequency coil with individually shielded elements*. Magn Reson Med 2010;64(6):1640-1651.
122. Balanis CA. *Antenna Theory: Analysis and Design*: Wiley-Interscience; 2005.
123. Van de Moortele PF UK. *Very Fast Multi Channel B1 Calibration at High Field in the Small Flip Angle Regime*. 2009; Honolulu, Hawaii, USA. p 336.
124. Yarnykh VL. *Actual flip-angle imaging in the pulsed steady state: a method for rapid three-dimensional mapping of the transmitted radiofrequency field*. Magn Reson Med 2007;57(1):192-200.
125. Nehrke K. *On the steady-state properties of actual flip angle imaging (AFI)*. Magn Reson Med 2009;61(1):84-92.
126. Adriany G, Auerbach EJ, Snyder CJ, Gozubuyuk A, Moeller S, Ritter J, Van de Moortele PF, Vaughan T, Ugurbil K. *A 32-channel lattice transmission line array for parallel transmit and receive MRI at 7 tesla*. Magn Reson Med 2010;63(6):1478-1485.
127. Adriany G, Van de Moortele PF, Wiesinger F, Moeller S, Strupp JP, Andersen P, Snyder C, Zhang X, Chen W, Pruessmann KP, Boesiger P, Vaughan T, Ugurbil K. *Transmit and receive transmission line arrays for 7 Tesla parallel imaging*. Magn Reson Med 2005;53(2):434-445.
128. Gilbert KM, Belliveau JG, Curtis AT, Gati JS, Klassen LM, Menon RS. *A conformal transceive array for 7 T neuroimaging*. Magn Reson Med 2012;67(5):1487-1496.
129. Raaijmakers AJE, Luijten PR, van den Berg CAT. *Dipole antennas for ultrahigh-field body imaging: a comparison with loop coils*. NMR Biomed 2015:n/a-n/a.
130. Cohen-Adad J, Mareyam A, Keil B, Polimeni JR, Wald LL. *32-channel RF coil optimized for brain and cervical spinal cord at 3 T*. Magn Reson Med 2011;66(4):1198-1208.
131. Wiggins G, Zhang B, Lattanzi R, Chen G, Sodickson D. *The Electric Dipole Array: An Attempt to Match the Ideal Current Pattern for Central SNR at 7 Tesla*. 20th Annual Meeting of the International Society for Magnetic Resonance in Medicine. Melbourne, Australia: ISMRM; 2012.

132. Collins CM, Liu W, Schreiber W, Yang QX, Smith MB. *Central brightening due to constructive interference with, without, and despite dielectric resonance*. Journal of Magnetic Resonance Imaging 2005;21(2):192-196.

# Appendices

# Appendix A

## Synthesized coupling coefficients for the lumped element 4-coil array

| | $Coil_1$ | $L_{1,1}$ | $L_{1,2}$ | $Coil_2$ | $L_{2,1}$ | $L_{2,2}$ | $Coil_3$ | $L_{3,1}$ | $L_{3,2}$ | $Coil_4$ |
|---|---|---|---|---|---|---|---|---|---|---|
| **$Coil_1$** | 1 | 0.6045 | 0 | ***0.0670*** | 0 | 0 | ***0.0410*** | -0.2872 | 0.2157 | ***0.0410*** |
| **$L_{1,1}$** | | -0.2906 | 0.4879 | 0 | 0 | 0 | 0 | 0 | 0 | 0 |
| **$L_{1,2}$** | | | -0.9939 | -0.0449 | 0 | 0 | 0 | 0 | 0 | 0 |
| **$Coil_2$** | | | | -0.9963 | -0.4966 | 0 | ***0.0670*** | 0 | 0 | ***0.0410*** |
| **$L_{2,1}$** | | | | | -0.0392 | -0.0349 | 0 | 0 | 0 | 0 |
| **$L_{2,2}$** | | | | | | 0.0254 | 0.3568 | 0 | 0 | 0 |
| **$Coil_3$** | | | | | | | 0.3029 | -0.0924 | 0 | ***0.0670*** |
| **$L_{3,1}$** | | | | | | | | 0.0636 | -0.2522 | 0 |
| **$L_{3,2}$** | | | | | | | | | 0.2669 | 0.8285 |
| **$Coil_4$** | | | | | | | | | | 0.2027 |

## Synthesized design matrix for the lumped element 4-coil array

| | $Coil_1$ | $L_{1,1}$ | $L_{1,2}$ | $Coil_2$ | $L_{2,1}$ | $L_{2,2}$ | $Coil_3$ | $L_{3,1}$ | $L_{3,2}$ | $Coil_4$ |
|---|---|---|---|---|---|---|---|---|---|---|
| **$Coil_1$** | 273.6 MHz | 14.4 pF | | ***0.0670*** | | | ***0.0410*** | 28.8 pF | 5.14 pF | ***0.0410*** |
| **$L_{1,1}$** | | 290.3 MHz | 28.7 pF | | | | | | | |
| **$L_{1,2}$** | | | 273.7 MHz | 1.1 pF | | | | | | |
| **$Coil_2$** | | | | 273.6 MHz | 11.7 pF | | ***0.0670*** | | | ***0.0410*** |
| **$L_{2,1}$** | | | | | 296.3 MHz | 3.15 pF | | | | |
| **$L_{2,2}$** | | | | | | 297.8 MHz | 7.42 pF | | | |
| **$Coil_3$** | | | | | | | 304.4 MHz | 1.95 pF | | ***0.0670*** |
| **$L_{3,1}$** | | | | | | | | 298.7 MHz | 22.2 pF | |
| **$L_{3,2}$** | | | | | | | | | 303.5 MHz | 17.1 pF |
| **$Coil_4$** | | | | | | | | | | 302.0 MHz |

## Truncated coupling matrix for the distributed filter 4-coil array

| | $Coil_1$ | $D_1$ | $D_2$ | $D_3$ | $D_4$ | $D_5$ | $D_6$ | $D_7$ | $D_8$ | $D_9$ | $D_{10}$ | $Coil_2$ |
|---|---|---|---|---|---|---|---|---|---|---|---|---|
| **$Coil_1$** | -0.075302 | -0.24434 | -0.19704 | -0.474 | -0.1 | -0.09071 | -0.2906 | -0.23629 | -0.40238 | -0.246 | -0.27065 | ***0.0397*** |
| **$D_1$** | | 0 | -0.36598 | 0 | 0 | 0 | 0 | 0 | 0 | 0 | 0 | -0.24434 |
| **$D_2$** | | | 0 | 0.099998 | 0 | 0 | 0 | 0 | 0 | 0 | 0 | -0.19704 |
| **$D_3$** | | | | 0 | -0.4053 | 0 | 0 | 0 | 0 | 0 | 0 | -0.474 |
| **$D_4$** | | | | | 0 | -0.1 | 0 | 0 | 0 | 0 | 0 | -0.1 |
| **$D_5$** | | | | | | 0 | -0.4254 | 0 | 0 | 0 | 0 | -0.09071 |
| **$D_6$** | | | | | | | 0 | -0.35949 | 0 | 0 | 0 | -0.2906 |
| **$D_7$** | | | | | | | | 0 | -0.09867 | 0 | 0 | -0.23629 |
| **$D_8$** | | | | | | | | | 0 | -0.62323 | 0 | -0.40238 |
| **$D_9$** | | | | | | | | | | 0 | -0.2857 | -0.246 |
| **$D_{10}$** | | | | | | | | | | | 0 | -0.27065 |
| **$Coil_2$** | | | | | | | | | | | | -0.06625 |

## Truncated design matrix for the distributed filter 4-coil array

| | **$Coil_1$** | **$D_1$** | **$D_2$** | **$D_3$** | **$D_4$** | **$D_5$** | **$D_6$** | **$D_7$** | **$D_8$** | **$D_9$** | **$D_{10}$** | **$Coil_2$** |
|---|---|---|---|---|---|---|---|---|---|---|---|---|
| **$Coil_1$** | 293.5 MHz | 9.62 mil | 7.76 mil | 18.7 mil | 3.94 mil | 3.57 mil | 11.4 mil | 9.3 mil | 15.8 mil | 9.68 mil | 10.7 mil | ***0.0397*** |
| **$D_1$** | | 0 | 14.4 mil | | | | | | | | | 9.62 mil |
| **$D_2$** | | | 0 | 3.93 mil | | | | | | | | 7.76 mil |
| **$D_3$** | | | | 0 | 16.0 mil | | | | | | | 18.7 mil |
| **$D_4$** | | | | | 0 | 3.94 mil | | | | | | 3.94 mil |
| **$D_5$** | | | | | | 0 | 16.7 mil | | | | | 3.57 mil |
| **$D_6$** | | | | | | | 0 | 14.2 mil | | | | 11.4 mil |
| **$D_7$** | | | | | | | | 0 | 3.89 mil | | | 9.3 mil |
| **$D_8$** | | | | | | | | | 0 | 24.5 mil | | 15.8 mil |
| **$D_9$** | | | | | | | | | | 0 | 11.2 mil | 9.68 mil |
| **$D_{10}$** | | | | | | | | | | | 0 | 10.7 mil |
| **$Coil_2$** | | | | | | | | | | | | 293.9 MHz |

# Appendix B

This appendix provides pseudo-code for the various design algorithms implemented in software throughout the thesis: (1) RF shimming, (2) coupling matrix synthesis, and (3) dipole shape optimization. All code can be found in the following code-repository: https://github.com/llennoc89/thesis.git. Readers will note that additional software can be found in the repository. This additional software is used for formatting various inputs to the design software – magnetic field maps from CST Studio for use in Matlab for RF shimming, by example. However, the following pseudo-code should allow readers to design their own software based on the algorithms presented below.

## RF Shimming pseudo-code

Import individual{ $B_1^+$ maps} for *i* channels

Vectorize {$B_1^+$ maps} for *i* channels

Concatenate {$B_1^+$ maps} to *n* x *i* matrix

Initialize shim weights ***w*** *to circularly polarized mode*

for k = 1:length(*i)*

***w****(i) = 1*exp(i*2*pi*(i-1)*45/length(i))*

end

Set ***tol***

Set $\boldsymbol{B_1^+}(r)$ (desired transmission profile).

Compute minimization problem

while ***err*** > ***tol***

**Compute** $\|\boldsymbol{wB_1^+}(r,\boldsymbol{w}) - \boldsymbol{B_1^+}(r)\| = \boldsymbol{err}$ for $\boldsymbol{w}$

return

## Coupling Matrix Synthesis

Compute individual{element-to-element coupling} for *i* elements

Estimate element-to-element coupling values $\{\boldsymbol{M_{i,j}}\}$

Populate coupling matrix $\{\boldsymbol{M}\}$

Initialize *j* decoupling sections

Compute $\{\boldsymbol{s}\}$ stencil for deoupling entries in $\{\boldsymbol{M}\}$

Compute impedance matrix $\{\boldsymbol{A}\}$ where length(diagonal($\boldsymbol{A}$)) = $j*i+i$

Initial *i* reflection polynomials $\{\boldsymbol{R_i}\}$ and $i*j$ transmission polynomials $\{\mathbf{t_{i,j}}\}$

Set ***tol***

Compute minimization problem

while ***err*** > ***tol***

for k = 1 to number of points in transfer function

$\boldsymbol{M} = \boldsymbol{M}*\boldsymbol{s}$

$\boldsymbol{\Gamma_{i,i}} = 1 + 2jR_m[\boldsymbol{A}]^{-1}_{i,i}$

$\mathbf{T_{i,j}} = -2j\sqrt{R_m R_k}[\boldsymbol{A}]^{-1}_{i,j}$

**Compute** $\left\|(\boldsymbol{\Gamma}(\mathrm{k},\mathbf{M})_{\boldsymbol{i,i}} - \boldsymbol{R}(k)_{\boldsymbol{i}}) + (\mathbf{T}_{\boldsymbol{i,j}}(k,\boldsymbol{M}) - \mathbf{t}_{\boldsymbol{i,j}}(k))\right\| = \boldsymbol{err}$ for $\boldsymbol{M}$

end

return

## Dipole Shape Optimization

Initialize dimensions with points $\boldsymbol{p}$

A = $\{[lb_x, lb_y] > \boldsymbol{p} < [ub_x, ub_y]\}$

while isfalse(A)

Initialize dimensions with points $\boldsymbol{p}$

A = $\{[lb_x, lb_y] > \boldsymbol{p} < [ub_x, ub_y]\}$

Continue

Construct trace through points $\boldsymbol{p}$

Minimization problem

while ***err*** > [***tol]***

*Compute FDTD solution to EM fields*

for k = 1 to number of voxels in ROI

**Compute**

$$\boldsymbol{obj_1} = \sum \boldsymbol{B_1^+}(r) - \boldsymbol{B_{1\,Desired}^+}(r)$$

$$\boldsymbol{obj_2} = \sum \boldsymbol{SAR}(r) - \boldsymbol{SAR_{Desired}}(r)$$

end

**Compute**

$$\boldsymbol{obj_3} = \boldsymbol{mean}(\boldsymbol{B_1^+}(r)_{\boldsymbol{ROI}})$$

$$\boldsymbol{obj_4} = \boldsymbol{X}|_{\boldsymbol{f=297.2\ MHz}}$$

CMA-Evoluationary Algorithm

$\boldsymbol{err} = [\boldsymbol{obj_1}, \boldsymbol{obj_2}, \boldsymbol{obj_3}, \boldsymbol{obj_4}]$

Pick new $\boldsymbol{p}$

return

# Curriculum Vitae

Ian R. O. Connell

Revised: 01/2017

---

## Education

| | |
|---|---|
| **01/2017 - Present** | **Post-Doctoral Fellow, Physics & Astronomy**<br>University of Western Ontario, London, Ontario<br>Supervisor: Dr. Blaine Chronik, Ph.D. |
| **09/2012 – 01/2017** | **Doctor of Philosophy (Ph.D.) Candidate, Medical Biophysics**<br>University of Western Ontario, London, Ontario<br>Supervisor: Dr. Ravi S. Menon, Ph.D. |
| **09/2007 - 04/2012** | **Bachelors of Engineering (B.Eng), Engineering Physics**<br>McMaster University, Hamilton, Ontario<br>Specialization: **Nuclear Engineering** |

## Research Interests

| | | |
|---|---|---|
| MRI engineering | MRI RF hardware | Ultra-high field MRI |
| Computational electromagnetics | MRI safety | Antenna design |
| Gradient coil design | Advanced filter synthesis | Microwave/RF engineering |

## Professional Experience

| | |
|---|---|
| 09/2016 – Present | **MRI Scientist**<br>Synaptive Medical, Toronto, ON, Canada |
| 09/2012 – 05/2017 | **Graduate Student**<br>Robarts Research Institute, London, ON, Canada |

04/2012 - 08/2012 **Summer Student**

Robarts Research Institute, London, ON, Canada

09/2010 - 01/2011 **Teaching Assistant** (Engineering 3Y03)

McMaster University, Engineering Department, Hamilton, ON, Canada

04/2010 - 05/2011 **Research Assistant, Medical Physics Department**

McMaster University, Hamilton, ON, Canada

Supervisor: Dr. Michael Farquharson, Ph.D.

04/2009 - 08/2009 **Engineering Technician**

Niagara Region, Public Works, Thorold, ON, Canada

09/2006 - 08/2008 **Engineering Technician**

Chris Tossell Architect, Sault Ste. Marie, ON

## Peer-Reviewed Publications

### Published

1. **Connell IRO** and Menon RS. General Coupling Matrix Synthesis for Decoupling MRI RF Arrays. *IEEE Transactions on Medical Imaging* 35 (10), 2229-2242. October 2016.

2. **Connell IRO**, Abou-Khousa MA, Gilbert KM and Menon RS. MRI RF Array Decoupling Method with Magnetic Wall Distributed Filters. *IEEE Transactions on Medical Imaging* 34 (4), 836-845. April 2015.

3. **Connell IRO**, Gilbert KM, Abou-Khousa MA and Menon RS. Design of a Parallel Transmit Head Coil at 7T with Magnetic Wall Distributed Filters. *IEEE Transactions on Medical Imaging* 34 (4), 825-835. April 2015.

### Submitted or Under Review

1. **Connell IRO** and Menon RS. Conformal Electric Dipole Arrays: Implementation and Evaluation. *In Revision*.

# Intellectual Property

## Patents

1. System and Method for Decoupling Magnetic Resonance Imaging Radio Frequency Coils with a Modular Magnetic Wall. United States. PCT/US13/212002. 2012-07-05.

# Peer-Reviewed Presentations

## Invited Poster Presentations

1. **Connell IRO** and Menon RS. Decoupling and Integration of Electric Dipoles into RF Arrays, 25th Joint Annual Meeting of ISMRM, April 2017, Hawaii, USA. **International.**

2. **Connell IRO** and Menon RS. Mixing RF Elements of Dissimilar Radiation Patterns, In Vivo Magnetic Resonance Gordon Research Conference, July 2016, Andover, NH. **International.**

3. **Connell IRO** and Menon RS. Design of RF Coils Mixing Elements of Dissimilar Radiation Pattern. 24th Joint Annual Meeting of ISMRM, May 2016, Singapore. **International.**

4. **Connell IRO**, Abou-Khousa MA, Gilbert KM and Menon RS. Design and Decoupling of a Parallel Transmit Head Coil at 7T Using Magnetic Walls. 22nd Joint Annual Meeting of ISMRM, May 2014, Milan, Italy. **International.**

5. **Connell IRO**, Abou-Khousa MA, Gilbert KM and Menon RS. Magnetic Walls for Ultra-High Field MRI. In Vivo Magnetic Resonance Gordon Research Conference, 2014. Andover, NH, USA. **International.**

6. **Connell IRO**, Abou-Khousa MA, Gilbert KM and Menon RS. MRI Hardware Enhancement via Metamaterials. London Health Research Day. 2014, London, ON, Canada. **Regional.**

7. **Connell IRO**, Abou-Khousa MA, Gilbert KM and Menon RS. New Methods of Decoupling 7T MRI Transmit-Only-Head-Coil Elements via Metamaterials. 11th Annual Imaging Network Ontario Symposium, February 4-5 2013, Toronto, ON, Canada. **Provincial. Awarded 3rd prize in poster competition.**

**Invited Talks**

1. **Connell IRO** and Menon RS. Shape-Optimization of Electric Dipoles for Human Head Imaging at 7 Tesla, 25th Joint Annual Meeting of ISMRM, April 2017, Hawaii, USA. **International.**

2. **Connell IRO** and Menon RS. Mixing RF Elements of Dissimilar Radiation Patterns, In Vivo Magnetic Resonance Gordon Research Conference, July 2016, Andover, NH. **International.**

3. **Connell IRO and Menon RS.** Evolutionary Antenna Design for Magnetic Resonance Imaging. Canadian Institute of Health Research Student Forum, June 2016, Winnipeg, MB, Canada. **National**.

4. Connell IRO and Menon RS. Evolutionary Antenna Design for Magnetic Resonance Imaging. London Health Research Day, April 2016, London, ON, Canada. **Regional**. **Awarded 1st prize in platform speaker competition.**

5. Gilbert KM, **Connell IRO** and Menon RS. Educational Session: RF Engineering – Coils. 23rd Join Annual Meeting of ISMRM, June 2015, Toronto, ON, Canada. **International.**

6. **Connell IRO**, Abou-Khousa MA, Gilbert KM and Menon RS. Design and Decoupling of a Parallel Transmit Head Coil at 7T Using Magnetic Walls. 22nd Joint Annual Meeting of ISMRM, May 2014, Milan, Italy. **International.**

**Invited Speaker**

1. **Connell IRO**. Metamaterials for Magnetic Resonance Imaging. 7th International Conference on Metamaterials, Photonic Crystals and Plasmonics (META). July 2016, Malaga, Spain. I**nternational.**

**Invited Lectures**

1. **Connell IRO**. Specific Absorption Rate (SAR) and MRI Patient Safety. Centre for Functional and Metabolic Mapping (CFMM) Winter School, University of Western Ontario. January 2015, London, Ontario, Canada. **Institutional.**

2. **Connell IRO**. The Engineering of MRI for Neurological Assessment. Retiring with Strong Minds, December 2014, London, Ontario, Canada. **Institutional.**

## Teaching

1. Lecturer - Biophysics 9663B MRI Physics, University of Western Ontario. Winter 2016.

## Manuscript Reviews

*Ad hoc* reviewer

IEEE Transactions on Biomedical Circuits

IEEE Transactions on Biomedical Engineering

IEEE Transactions on Industrial Electronics

IEEE Transactions on Medical Imaging

IEEE Transactions on Microwave Theory and Techniques

Journal of Magnetic Resonance Imaging

Magnetic Resonance in Medicine

Nature Scientific Reports

Nature Materials

PLOS ONE

## Professional Membership & Association

**Professional Engineers of Ontario (PEO)**
Engineer in Training (EIT)

**International Society for Magnetic Resonance in Medicine (ISMRM)**
Graduate Student Member

**Institute of Electrical and Electronics Engineers (IEEE)**
Graduate Student Member

**Rowing Canada (2010-2011, 2013-2014)**
National Team Athlete

## Committees

1/2016 – Present **University of Western Ontario Varsity Rowing Team Executive**
Media & Relations

10/2014 – 6/2015 **Robarts Research Institute, London, ON**

Scientific Director Selection Committee

## Scholarships

01/2017 – Present **Mitacs Accelerate Post-Doctoral Fellowship**
**$ 55,000 yearly**

University of Western Ontario, London, ON, Canada
Synaptive Medical, Toronto, ON, Canada

05/2015 – 09/2016 **Ontario Graduate Scholarship (OGS)**
**$ 15,000 yearly**

University of Western Ontario, London, ON, Canada

09/2012 - Present **Western Graduate Research Scholarship**
**$ 3,500 yearly**

University of Western Ontario, London, ON, Canada

09/2007 - 04/2012 **Entrance Scholarship (renewed)**
**$ 2,500 yearly**

McMaster University, Hamilton, ON, Canada

09/2010 - 04/2012 **Marauder Scholar** (Dean's list and varsity athlete)

McMaster University, Hamilton, ON, Canada

04/2007 - 05/2011 **Group Health Centre Scholarship: John Barker Scholarship (renewed)**
**$ 12,000 yearly**

Group Health Centre, Sault Ste. Marie, ON, Canada

## Awards

07/2016 **Outstanding Poster Award - International ($300)**

Gordon Research Conference, July 2016, Andover, NH.

06/2016 **Honorable Mention - National**

Canadian Institute of Health Research Student Forum

04/2016 **I$^{st}$ Prize Platform Speaker – Regional ($700)**

London Health Research Day, April 2016, London, ON, Canada.

04/2016 **Trainee Stipend - International ($500)**

24$^{th}$ Joint Annual Meeting of ISMRM, May 2016, Singapore.

04/2015 **University of Western Ontario Athletics Bronze Award**

*Excellence in Men's Rowing*

University of Western Ontario, London, ON, Canada

05/2014 **Trainee Stipend - International ($500)**

22$^{nd}$ Joint Annual Meeting of ISMRM, May 2014, Milan, Italy.

02/2013 **3rd Prize - Ontario Consortium on Building a Better Brain Provincial ($300)**

11$^{th}$ Annual Imaging Network of Ontario Symposium, Toronto, ON, Canada

Various **McMaster University Athletic Awards (Rowing)**

*McMaster University, Hamilton, ON, Canada*

- Men's Rowing team captain (2008-2012), "Rowing Rookie of the Year Award" (2007/2008), Most Valuable Oarsman (2008/2009, 2009/2010, 2011/2012)

04/2007 **Lieutenant Governor's Community Volunteer Award**

04/2006 **Royal Conservatory of Music: Grade 9 Piano Practical Exam**

## Community

2015 – Present **Executive Council**

University of Western Ontario Varsity Rowing

2008 - 2012 **McMaster Athletic Council**

McMaster University, Hamilton, ON

2007 - 2012 **Executive Council**

Leander Boat Club, Hamilton, ON

2005 - 2007 **Volunteer**

Habitat for Humanity, Sault Ste. Marie, ON

2002 - 2007 **Coach**

YMCA Basketball League**,** Sault Ste. Marie, ON